

Constitutive Modeling of Active Polymers

by

Scott V. Therkelsen

B. S. Mechanical Engineering
The University of Iowa, 2002

SUBMITTED TO THE DEPARTMENT OF MECHANICAL ENGINEERING IN
PARTIAL FULFILLMENT OF THE REQUIREMENTS FOR THE DEGREE OF

MASTER OF SCIENCE IN MECHANICAL ENGINEERING
AT THE
MASSACHUSETTS INSTITUTE OF TECHNOLOGY

[February 2005]
January 2005

© 2005 Scott V. Therkelsen. All rights reserved

The author hereby grants to MIT permission to reproduce
and to distribute publicly paper and electronic
copies of this thesis document in whole or in part

Signature of Author: _____

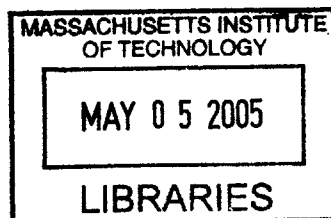
Department of Mechanical Engineering
January 24, 2005

Certified by: _____

Mary C. Boyce
Professor of Mechanical Engineering
Thesis Supervisor

Accepted by: _____

Lallit Anand
Professor of Mechanical Engineering
Graduate Officer



BARKER

Constitutive Modeling of Active Polymers

by
Scott Therkelsen

Submitted to the Department of Mechanical Engineering
on January 24, 2005 in Partial Fulfillment of the
Requirements for the Degree of Master of Science in
Mechanical Engineering

Abstract

This thesis develops a three-dimensional constitutive model of active polymeric materials, including changes in material volume and properties due to actuation.

Active polymers reversibly change shape, volume and/or material properties in response to some external stimulus. Electric fields are a common driving force for this actuation, though changes in pH, temperature, magnetic field, or visible light have been studied in their role as stimuli.

The study and future use of conducting polymer actuators is important because of their potential to meet and exceed the capabilities of currently available materials in a variety of fields, most notably in the field of artificial muscles.

This thesis first reviews the basic principles of continuum mechanics, followed by a review of the classical and current statistical mechanics based constitutive models for rubber-like materials. A theoretical model for reversibly swelling active polymer gels is presented. Material responses to different homogeneous deformation conditions are then studied as a function of swelling. The effect of inert rigid filler particles on the swelling behavior of an active polymer is then studied using a closed-form solution of a boundary value problem developed in the literature. The constitutive model is also used in a study of the behavior of a bimorph strip, noting that the responsive nature of active polymers is often mechanically accentuated by layering with other materials, with implications for future work on transient analysis. Finite element analysis is implemented for verification and analysis of the boundary value problem.

Thesis Supervisor: Mary C. Boyce
Title: Professor of Mechanical Engineering

Acknowledgments

I would like first to thank Mary Boyce, my advisor over the last two years on this project. Her support and guidance for this work is rivaled only by her patience and perseverance. The range of knowledge and interests she provided was invaluable for the successful completion of this work.

I extend thanks to Simona Socrate for her general support and for assistance with some lengthy derivations. David Parks also deserves thanks for his class on elasticity that was the seed for this project, as well as his review of portions of the analysis. Likewise, I would like to acknowledge the important contributions by Mats Danielsson and Ethan Parsons for creating and assisting with the implementation of the computational models of multiparticle arrays. I would like to thank Ian Hunter and his research group – particularly Patrick Anquetil for sharing his knowledge and resources, as well as his assistance fabricating polypyrrole samples.

I would also acknowledge the extremely helpful and seemingly always available Una Sheehan for the uncountable list of small favors and helpful answers she provided. Leslie Regan, Ray Hardin, and Pierce Hayward also deserve thanks for their aid.

Past colleagues have been instrumental in assisting my academic research and helping me keep perspective, most notably including Babak Cohan, Rajdeep Sharma, Hang (Jerry) Qi, Adam Mulliken, Mike Bauerly, Kristi Schmidt, and all the members of the MIT graduate soccer club.

I acknowledge the National Defense Science and Engineering Graduate fellowship program for financial support of this work. Likewise, the Dupont/MIT Alliance and the MIT Institute for Soldier Nanotechnologies helped support this research.

Lastly, I would like to thank my family without whose support none of this would have been possible. To my mom Sandy, my dad Ken, and my brother Ryan. And especially to Dianne, Custer, and Sasha. Thank you.

Contents

| | | |
|--|-------|----|
| Abstract | | 2 |
| Acknowledgments | | 3 |
| Contents | | 4 |
| List of Figures | | 6 |
| Chapter 1: Introduction | | 11 |
| 1.1 Active Polymers | | 11 |
| 1.1.1 Overview | | 11 |
| 1.1.2 History | | 18 |
| 1.2 Objective | | 20 |
| 1.3 Scope of the Work | | 20 |
| 1.4 Reference | | 20 |
| Chapter 2: Review of Continuum Mechanics and A Statistical Mechanics Based Constitutive Model of Rubber Elasticity | | 23 |
| 2.0 List of Symbols | | 23 |
| 2.1 Kinematics | | 24 |
| 2.2 Stress | | 26 |
| 2.3 Constitutive Equations | | 28 |
| 2.3.1 Statistical Mechanics | | 28 |
| 2.3.2 Strain-Energy Functions | | 32 |
| 2.3.2.1 Thermodynamics | | 32 |
| 2.3.2.2 Stress | | 35 |
| 2.4 Reference | | 38 |
| Chapter 3: Swelling | | 39 |
| 3.1 Kinematics | | 40 |
| 3.2 Constitutive Equations of Swelling Behavior | | 42 |

| | | |
|------------|---|----|
| 3.2.1 | Statistical Mechanics of Swelling | 42 |
| 3.2.2 | Strain-Energy Functions of Swelling Behavior | 46 |
| 3.2.2.1 | Thermodynamics | 46 |
| 3.2.2.2 | Stress | 47 |
| 3.3 | Reference | 49 |
| Chapter 4: | Examples and Results | 50 |
| Chapter 5: | Application: Filled Polymers | 61 |
| 5.1 | Filled Polymers: Background | 61 |
| 5.2 | Spherical Shell Model | 62 |
| 5.2.1 | Kinematics and Boundary Conditions | 62 |
| 5.2.2 | Stress Analysis | 66 |
| 5.3 | Finite Element Analysis/Conclusions | 72 |
| 5.4 | The Multiparticle Representative Volume Element | 76 |
| 5.5 | The Cylindrical Representative Volume Element | 80 |
| 5.6 | Reference | 83 |
| Chapter 6: | Future Work and Conclusion | 84 |
| 6.1 | Future Work: Transient Analysis and the Bilayer Strip | 84 |
| 6.1.1 | Model Description | 85 |
| 6.1.2 | Model Results: Steady State | 89 |
| 6.1.3 | Transient Analysis and Future Work | 91 |
| 6.2 | Conclusions | 92 |
| 6.3 | Reference | 93 |
| Appendix | | 94 |

List of Figures

| | |
|----------------------------|---|
| Figure 1.1 p. 11 | Schematic of polyethylene |
| Figure 1.2 p. 11 | Schematic of a polymer gel |
| Figure 1.3 p. 12 | The chemical structure of polypyrrole |
| Figure 1.4 p. 13 | Polypyrrole with local charge carriers |
| Figure 1.5 p. 14 | The chemical structures of PVA and PAA |
| Figure 1.6 p. 15 | The chemical structure of PVA-PAA gel |
| Figure 1.7 p. 15 | Schematic of PVA-PAA immersed in neutral water |
| Figure 1.8 p. 16 | Expansion and contraction of a PVA-PAA gel from [1.15] |
| Figure 2.1 p. 24 | Reference and current configurations of a body |
| Figure 2.2 p. 26 | Traction vectors on infinitesimal surface elements |
| Figure 2.3 p. 27 | Gaussian statistical distribution of polymer chain end-to-end lengths |
| Figure 2.4 p. 33 | 8-chain model representative volume element |
| Figure 2.5 p. 34 | Deformation of the 8-chain polymer network under a tension loading |
| Figure 3.1 p. 40 | Schematic representation of the multiplicative decomposition, $\Lambda_i = \lambda_i^m \lambda_s$ |

| | |
|-----------------------------|--|
| Figure 3.2 p. 42 | Rigid chamber with two types of particles initially separated and then allowed to mix |
| Figure 3.3 p. 43 | Schematic of a polymer separated from fluid particles and then allowed to mix |
| Figure 3.4 p. 46 | Balance of network tension and osmotic pressure in a swelled polymer |
| Figure 4.1 p. 50 | Comparison of Gaussian and 8-chain models for simple tension |
| Figure 4.2 p. 51 | Comparison of Gaussian and 8-chain models for simple tension, including swelling effects |
| Figure 4.3 p. 52 | Total entropy change at different swelling ratios for a Gaussian polymer/solute |
| Figure 4.4 p. 53 | Osmotic pressure and total hydrostatic tension during uniaxial loading |
| Figure 4.5 p. 54 | Stress-strain response to uniaxial tension and swelling, 8-chain model |
| Figure 4.6 p. 54 | Stress-strain response to uniaxial tension and swelling, Gaussian model |
| Figure 4.7 p. 55 | Stress-strain response to uniaxial tension, small stretch regime |
| Figure 4.8 p. 55 | Stress-strain response to uniaxial tension, varying cross-link density |
| Figure 4.9 p. 56 | Stress-strain response to uniaxial compression with swelling |
| Figure 4.10 p. 56 | Stress-strain response to simple shear with swelling |
| Figure 4.11 p. 57 | PVA-PAA gel uniaxial deformation, experimental (from [4.1]) |
| Figure 4.12 p. 57 | PVA-PAA gel uniaxial deformation, theoretical (from [4.1]) |

| | |
|-----------------------------|---|
| Figure 4.13 p. 58 | PVA-PAA gel uniaxial deformation, 8-chain prediction |
| Figure 4.14 p. 59 | PVA-PAA gel equibiaxial deformation, 8-chain prediction |
| Figure 5.1 p. 61 | A hypothetical material randomly filled with particles |
| Figure 5.2 p. 62 | A hypothetical material divided using Voronoi tessellation |
| Figure 5.3 p. 63 | Schematic representation of the initial, reference, and deformed configurations of a spherical shell representative volume element (from [5.2]) |
| Figure 5.4 p. 64 | The reduction in swelling caused by increased filler content (spherical shell results) |
| Figure 5.5 p. 65 | The reduction in swelling at different unconstrained swelling ratios (spherical shell results) |
| Figure 5.6 p. 69 | Radial interfacial stress as a function of the initial swelling ratio |
| Figure 5.7 p. 70 | Hoop and radial stress distributions at various swelling levels |
| Figure 5.8 p. 71 | Hoop and radial stress distributions at various volume fractions of filler |
| Figure 5.9 p. 72 | Spherical shell geometry in finite element model |
| Figure 5.10 p. 72 | Computer generated mesh of the spherical geometry |
| Figure 5.11 p. 73 | An example radial stress distribution |
| Figure 5.12 p.74 | Hoop and radial stress distributions – a comparison between the analytical solution and the computational solution |
| Figure 5.13 p. 76 | A randomly distributed multiparticle mesh |

| | |
|-----------------------------|--|
| Figure 5.14 p. 77 | A translucent display of the multiparticle mesh |
| Figure 5.15 p. 77 | A spherical cell compared to Voronoi tessellation |
| Figure 5.16 p. 78 | A cutaway view of the undeformed multiparticle mesh |
| Figure 5.17 p. 78 | A cutaway view of the swelled multiparticle assembly with Von Mises stress |
| Figure 5.18 p. 79 | Comparison of stress-strain characteristics for the filled and unfilled polymer |
| Figure 5.19 p. 80 | A circular cylinder with embedded cylindrical particle |
| Figure 5.20 p. 82 | The reduction in swelling caused by increased filler content (cylindrical shell results) |
| Figure 5.21 p. 82 | The reduction in swelling at different unconstrained swelling ratios (cylindrical shell results) |
| Figure 6.1 p. 84 | Sketch of a fiber grabbed by a microfingert |
| Figure 6.2 p. 84 | A microrobot arm moves a bead across a system of polyurethane tracks |
| Figure 6.3 p. 85 | A schematic picture of a cell clinic consisting of a microcavity and lid |
| Figure 6.4 p. 85 | Basic schematic of a bilayer strip |
| Figure 6.5 p. 85 | Deflection of a bilayer strip |
| Figure 6.6 p. 86 | A cross section of an encapsulated bilayer actuator |
| Figure 6.7 p. 86 | Finite element instance of two strips of material |

| | |
|-----------------------------|--|
| Figure 6.8 p. 87 | Bilayer strip, modeled after Figure 6.4 |
| Figure 6.9 p. 87 | Sectioning the bilayer strip to exploit symmetry |
| Figure 6.10 p. 88 | The rigid body constraint on the bilayer strip |
| Figure 6.11 p. 88 | Constraints applied along symmetry planes |
| Figure 6.12 p. 88 | An 8-node brick mesh of the bilayer strip |
| Figure 6.13 p. 89 | Bending of the bilayer strip due to swelling action with contours of vertical displacement |
| Figure 6.14 p. 90 | Deflection of a “thick” bilayer strip plotted with Von Mises stress contours |

Chapter 1: Introduction

1.1 Active Polymers

1.1.1 Overview

The word *polymer* is derived from the Greek *polu* meaning many (poly) and *meros* meaning parts. The “parts” are repeating chemical units that are covalently bonded to each other to form long chains. These chains may consist of many thousands to millions of repeating units, and so polymer molecules are usually of very high molecular weight. For example, a molecule of polyethylene consists of a CH₂ unit repeated tens of thousands of times. This may be indicated by writing (CH₂)_{*n*}, where the subscript *n* indicates the degree of polymerization and takes on a large value. Schematically, polyethylene may be represented in several ways, for example:

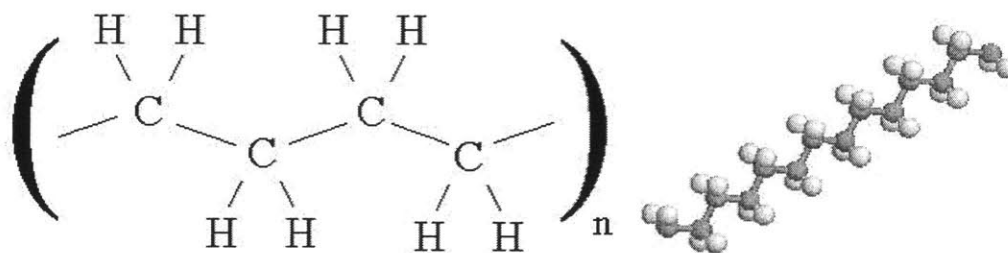


Figure 1.1: Traditional schematic representations of polyethylene.

Representations like those found in Figure 1.1 can be found in most high school chemistry books, however they are unfortunate in that they fail to grasp the most important feature of the polymer chain – its flexibility.

Rather than the rigid structures implied in Figure 1.1, polymer molecules should be thought of almost as microscopic string, able to take on an exceedingly large number of configurations. When many of these long chains are conglomerated into an elastic network, they become tangled and are more likely to form a network either simply due to physical entanglement or due to chemical crosslinking between chains. In a polymer gel, an interstitial fluid occupies the space between the chains, and the chains keep the fluid in place. This system is shown schematically in Figure 1.2:

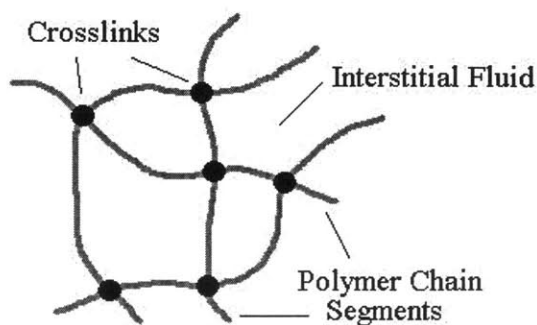


Figure 1.2: Schematic of a polymer gel.

The term *polymer gel* refers to a polymeric network combined with an interstitial fluid. A familiar example is the soft contact lens, a polymer gel consisting of poly(hydroxyethyl methacrylate) as the polymer network, and saline as the interstitial fluid [1.1].

Polymer gels are relatively compliant and can easily be deformed by external stimuli. As early as 1948, Kuhn [1.2], Breitenbach and Karlinger [1.3], and Katchalsky and Oplatka [1.4] independently found that water-swollen polymer gels can convert chemical energy directly into mechanical work under isothermal conditions. This conversion of microscopic chemical free energy to macroscopic mechanical work is the motivation behind the study of active polymer gels. Applications for such a material abound: actuators, sensors chemical valves, delivery controllers, selective separation, and so on [1.5-1.10]

Active polymers reversibly change shape, volume and/or material properties in response to some external stimulus. Electric fields are a common driving force for this actuation [1.11][1.12][1.13][1.14], though changes in pH [1.15], temperature [1.16], magnetic field [1.17] [1.18], or visible light [1.19] have been studied in their role as stimuli. Below, we briefly review these various categories of active polymers.

First, polymer gels that are activated by electric fields are often called *conducting polymer actuators*. The ability of conducting polymers to conduct electricity is an unusual capability for an organic material, made possible by their unique structure. Most organic compounds have strong covalent bonds that prevent electron mobility, but the conjugated backbone found in conducting polymers allows some degree of electron delocalization.

The study and future use of conducting polymer actuators is important because of their potential to meet and exceed the capabilities of currently available materials in a variety of fields. Many conducting polymers (e.g. polypyrrole) respond with forces that exceed that of mammalian skeletal muscle by up to two orders of magnitude [1.11]. This makes this material class a promising candidate for an artificial muscle. The chemical structure of polypyrrole is given in Figure 1.3:

Polypyrrole

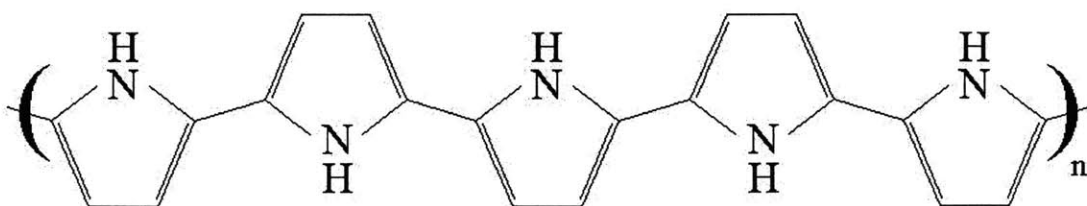


Figure 1.3: The chemical structure of polypyrrole.

The polymerization of the pyrrole monomers does not in general result in a neutral polymer as it is depicted in Figure 1.3. In fact, the charged backbone is what

enables polypyrrole to conduct electrons. A more appropriate representation is shown in Figure 1.4, which includes local positively charged portions of the backbone balanced by anions [1.11]:

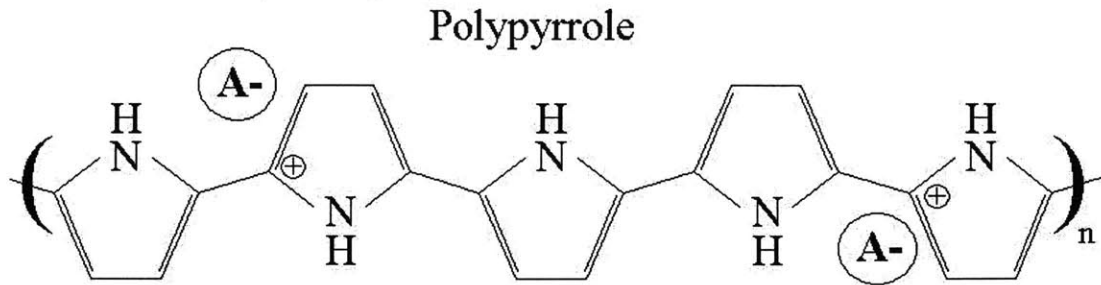


Figure 1.4: Polypyrrole with local charge carriers.

Electrical work is converted to mechanical work through chemical or electrochemical interactions that result in oxidation or reduction of the polymer chains. The oxidation state of the polymer causes a flux of ions to or from the material. This leads to conformational changes in the chain structure and an increase (or decrease) in volume of the material. Using this mechanism, this class of materials has been able to produce many forms of bending gel “fingers” [1.13][1.20][1.21], self-folding boxes (on a micro scale) [1.22], and underwater swimming devices that mimic the motion of a fish [1.20][1.23]. NASA is considering this type of material for the robotic arm on an interplanetary vehicle, as well as a lens dust wiper [1.24]. Because they are lightweight, they have excellent power-to-weight ratios as well.

Currently, there are several areas of understanding that prevent the implementation of these useful materials. Perhaps the most important of these is the lack of an accurate and predictive constitutive model. For example, in an engineering application, a designer may wish to predict the strains and displacements caused by a specific actuation mechanism and loading. A constitutive model predicts the strain response to a given stress field (or vice-versa). In the case of a conducting polymer actuator, the displacement would be predicted given the applied voltage and loading, for example. The degree of accuracy of these predictions under a variety of loading conditions indicates the quality of the constitutive model.

Actuation of a conducting polymer is the result of molecular level interactions. Advances in material processing make it conceivable that future materials could be rationally designed from the molecular level up, tailoring material properties to achieve a desired performance. Once again, a constitutive model whose underpinnings lay in the molecular structure of the material is a major stepping stone in the endeavor to create new and better performing actuators. Indeed, it may be possible to prescribe from the constitutive model, *a priori*, the necessary molecular structure to subsequently develop a better performing material.

Another class of active polymer that has been investigated extensively are those activated by changes in pH. Marra [1.15] and Marra, Ramesh, and Douglas [1.25]

studied a specific active polymer gel (poly(acrylic acid)-poly(vinyl alcohol) or PVA-PAA) that is responsive to changes in pH. Marra cites three forces that balance to determine the equilibrium swelling level of PVA-PAA. First, the cross-linked polymer gel network (as in Figure 1.2) has a specific equilibrium volume. Elastic forces resist any changes from this equilibrium state. Next, there is a pressure associated with the mixing of polymer and interstitial fluid, which will be explored in detail in the body of the work (see Chapter 3). Lastly, Marra cites the presence of charged side groups (like the positive local charges shown in Figure 1.4) as a source of internal forces. In order to maintain neutrality within the gel, the free ions from the surrounding fluid enter to balance the local charge. Regardless of the number of fixed charges, the concentrations of ions within the gel will always be greater than the concentrations in the surrounding fluid. As a result, the gel absorbs more water and expands in order to reduce the concentration gradients. Flory [1.26] describes the ionic pressure, π_i , within the gel due to the fixed charges by:

$$\pi_i = R\Theta \left(\frac{ic}{z} - \nu(c_i^* - c_i) \right), \quad (1.1)$$

where i is the number of fixed charges per polymer unit, c is the molar concentration of polymer units, z is the valence of the fixed charges, ν is the number of different ionic species present in the gel, c_i is the molar concentration of the free ions within the gel, c_i^* is the molar concentration of free ions in the surrounding fluid, R is the universal gas constant, and Θ is the absolute temperature.

Marra studied PVA-PAA extensively as a model gel. PVA and PAA have the following chemical structures:

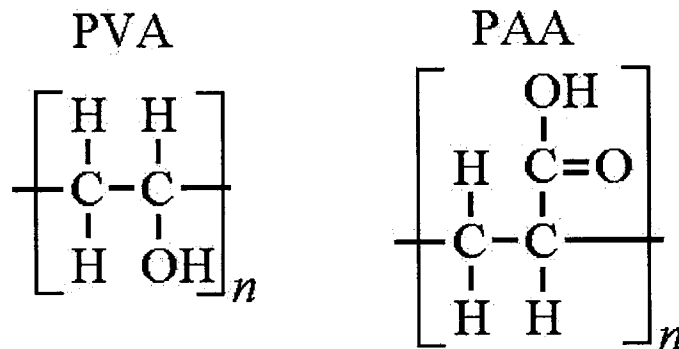


Figure 1.5: The chemical structures of PVA and PAA.

Using solvent casting and crosslinking techniques (see [1.15], Sections 2.3 and 2.4), PVA and PAA can be formed into a relatively simple, safe, and easy to fabricate actuating gel. The PVA-PAA gel has the following chemical structure:

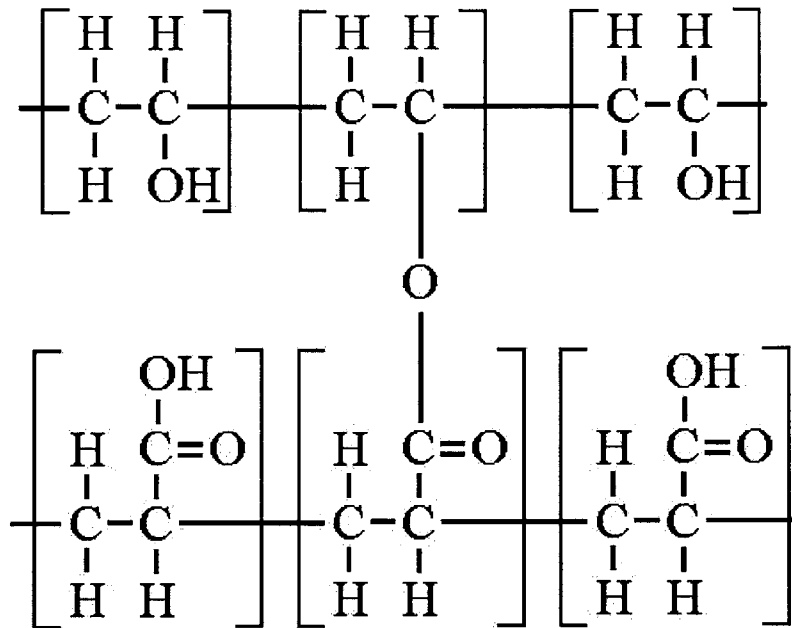


Figure 1.6: The chemical structure of PVA-PAA gel.

The reversible swelling caused by changes in pH may be understood by representing the PVA-PAA system schematically as in Figure 1.2:

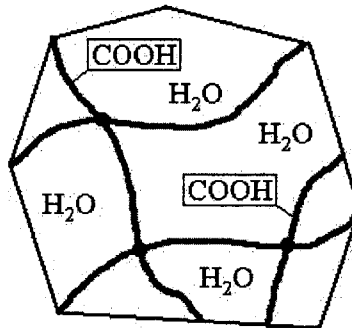


Figure 1.7: Schematic of a PVA-PAA gel immersed in neutral water.

The carboxyl side-groups on the PAA monomers are shown explicitly in Figure 1.7 because they are involved in the chemical reactions that make actuation possible. If the gel in Figure 1.7 is immersed in basic solution, these carboxyl side-groups react with the free (OH^-) hydroxide ions to form water molecules, leaving fixed negative charges on the polymer network. This creates ionic forces that cause the network to absorb more water (swell) and expand in volume. The network elasticity forces balance this swelling until a new equilibrium is reached. Likewise, placing the network in an acidic solution causes the free (H^+) hydrogen ions to bond to fixed negative charges on the polymer network. This neutralizes the gel and the elastic forces cause water to be expelled from the system and the volume to contract. This reversible cycle is given in Figure 1.8:

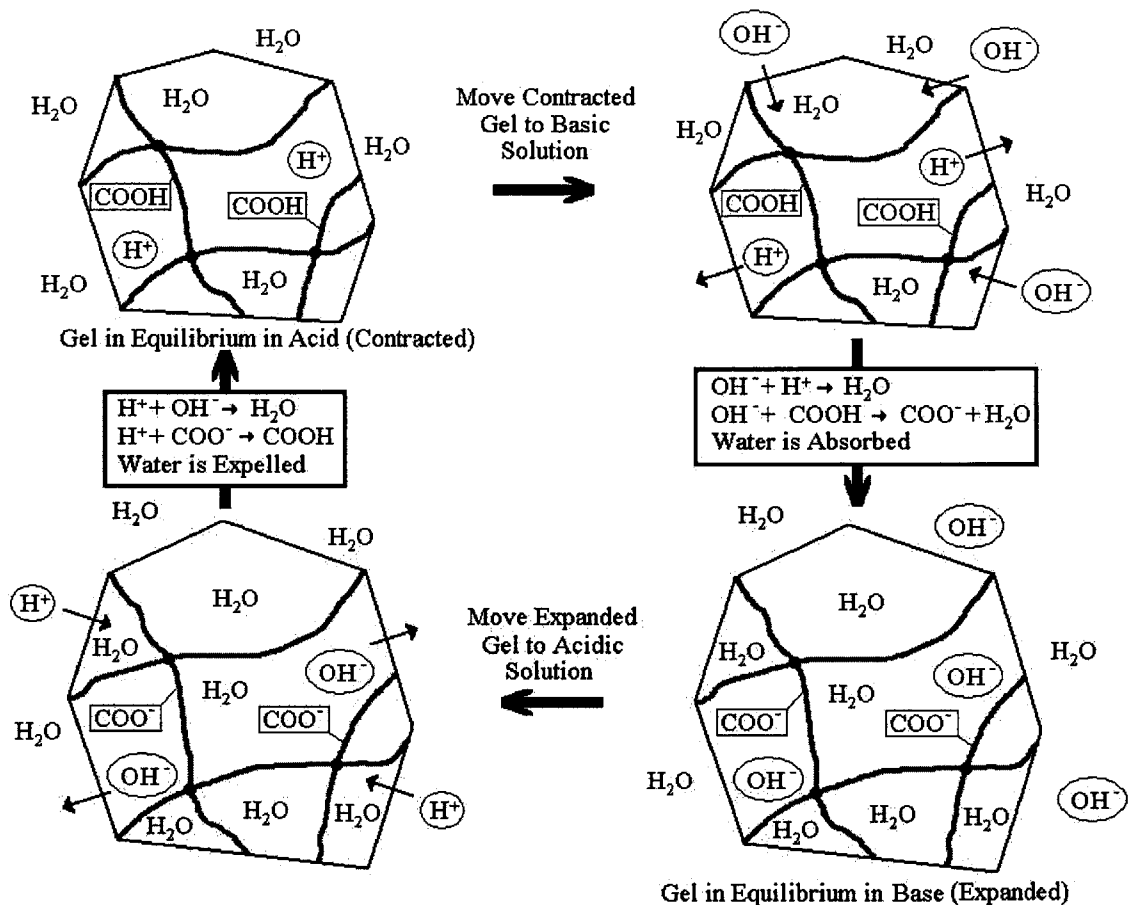


Figure 1.8: Expansion and contraction of a PVA-PAA gel. When a contracted gel is moved to a basic solution, the free ions diffuse in and out due to concentration gradients. The carboxyl side-groups then react with the free hydroxide ions to form water molecules, leaving fixed negative charges on the polymer network. Ionic forces are created, causing the gel to absorb water and expand. When placed in an acid, the free ions again diffuse in and out of the gel. The free hydrogen ions then bond to the fixed negative charges and neutralize the gel. The ionic forces are eliminated, water is expelled, and the gel contracts [1.15 – Figure 1.7].

Marra developed a finite-deformation elastic constitutive model utilizing an evolving internal variable to describe the mechanical behavior of active polymer gels, applied specifically to the PVA-PAA system. The material parameters used in the constitutive model are determined from uniaxial and biaxial test performed on the PVA-PAA gels in both the fully expanded and fully contracted states.

Temperature changes in the surrounding environment have also been observed as a mechanism for actuation. Matsuo and Tanaka [1.16] reported discontinuous volume-phase transitions in spherical *N*-isopropylacrylamide gels. The phenomena they observe are interpreted in a similar way to the familiar gas-liquid phase transition, and appear to be universal to any type of gel. The gel is swollen at lower temperatures and undergoes a sharp collapse at a higher transitional temperature. The transition point varies between about 34°C and 60°C, depending on the concentration of the ionizable group in the network. Matsuo and Tanaka explore

the first-order kinetics of the swelling/shrinking of the gel and model it as a collective diffusion process. They report that the time constant for the process varies approximately with r^2 , though there are several discrepancies between the model and the experimental data including a “slowing down” when the final transition temperature is near the transition threshold and a plateau region during the shrinking process. They also observe the differences between swelling and shrinking, most strikingly the formation of “bubbles” on the surface of the spheres during shrinking that resemble the local swelling of weak portions of an inflated balloon.

Introducing magnetic nanoparticles into the polymer gel has created a completely different type of polymeric actuator. Zrínyi, Szabó, and Barsi [1.17] call these magnetic field sensitive gels *ferrogels*. The ferrofluid that surrounds the polymer network is a colloidal dispersion of magnetic particles with a typical size of about 10 nm. When an external magnetic field is applied, an instantaneous shape distortion occurs and dissipates upon removal of the field. In their review of magnetic field sensitive polymeric actuators [1.17], Zrínyi, Szabó, and Barsi reported the behavior of a PVA hydrogel filled with magnetite (Fe_3O_4) particles.

Adhesive forces attached the magnetite particles in the swelling liquid to the network chains. When no external magnetic field is present, the collection of randomly oriented single domain particles gives the gel no net magnetization. Under the action of a magnetic field, the particles tend to align and produce a bulk magnetization. Removal of the field causes a relaxation as the magnetic dipole moments randomize over time. The gradual randomization of the internal fields can be expressed in terms of relaxation times due to Brownian rotation of the magnetic moments with the rotation of the individual particles as well as randomization due to the Néel mechanism – a rotation of the magnetic moments inside the particles. The Brownian motion is a function of temperature, and is restricted by the polymer network attached to and surrounding the particles.

This class of actuating materials seems to apply mostly towards applications of linear actuation. The changes in material properties and dimensions are highly anisotropic – depending greatly on the applied magnetic field and the microstructure of the material. Uniform changes in volume seem to be negligible. Once again, a greater understanding of magneto-elastic coupling in these gels will facilitate such applications as reversible switches, sensors, micromachines, and energy-transducing devices. Eventually, using computers and a thorough understanding of their properties, ferrogels may be coordinated and controlled as artificial muscles.

Suzuki and Tanaka [1.19] elaborated on a class of gels sensitive to ultraviolet light. The ultraviolet light initiates an ionization reaction in the gel that creates internal osmotic pressure which induces swelling. When the light is removed, the polymer gel collapses. The process is slow because it relies on the photochemical ionization and subsequent recombination of ions. Suzuki and Tanaka found that gels

containing *N*-isopropylacrylamide and the light-sensitive chromophore, trisodium salt of copper chlorophyllin undergo phase transitions induced by visible light. Because these transitions are due only to the direct heating of the network polymers by the light, they are very fast and thus more useful in applications. Experiments were reported at a variety of temperatures, pHs, and light intensity levels.

Regardless of the actuation mechanisms, it is clear that active materials have established a niche that continues to expand into a wide variety of applications. They are already widespread in the field of energy conversion, effectively converting light, heat, electrical, chemical, and magnetic energy reversibly into mechanical work. Active polymers are also used to store and manage energy as they are integrated into fabrics and military uniforms. For example, bioresponsive polymeric fabrics are under study that enable heat, moisture, and nutrients from the human body to trigger biological reactions in the material that will suppress body odor or add water-repellency to clothing as needed [1.27]. The future of these bioresponsive materials, as well as the diverse array of active polymers described above, relies heavily and universally on a thorough understanding and characterization of the unique mechanisms that make them function.

1.1.2 History

Swelling and shrinking in polymer gels was first reported by Kuhn [1.2] and Katchalsky [1.28] in 1949. Since then, many researchers have explored this topic using a variety of different methods. Beginning with the publishing of his classic work in 1953, Flory [1.26] was the first to rigorously address the physics and chemistry of gel swelling. He used free energies and internal pressures to predict the equilibrium volume of the swelled network. Next, Tanaka and Fillmore [1.29] used a continuum mechanics-based model to predict the swelling behavior when dry, neutral gels are placed in water. Their model shows that swelling time is proportional to the square of the linear dimension of the gel and to the diffusion coefficient of the polymer network. Chiarelli and De Rossi [1.30] adapted this to their poroelastic model, where the polymer network and interstitial fluid are considered as separate materials and overall mechanical behavior is determined using mixture theory. This model is inaccurate at large deformations because it still assumes the linear elasticity of the polymer network.

Numerous attempts have been made to accurately describe swelled polymers in the large deformation regime. Nagy [1.31] and Horkay and Zrinyi [1.32] used Mooney-Rivlin material laws to describe gels. Material properties were assumed to remain constant, and only one-dimensional deformations were considered. Humphrey and Rajagopal [1.33] proposed a large-deformation finite-thermoelastic constitutive theory for elastomers that includes volume change through thermal expansion. This model only allows for relatively small volume changes compared to the swelling attainable by polymer gels. The previously described works by Marra et. al. [1.15][1.25] introduced an evolving internal state variable to model changes in material properties induced by swelling.

In 1991, a new field of active materials was opened when Baughman, Shacklette and Elsenbaumer first proposed conducting polymer-based actuators [1.34]. Since then, no fewer than thirty articles by ten or more research groups have been written on the subject of conducting polymer actuators (see [1.11], Section 2.2). These studies began with the demonstration of bilayer actuators, to be discussed in Chapter 6, which showed qualitative deformations with little quantitative information about performance. The introduction of linear actuators helped to standardize a benchmark from which different experiments could be compared. However, it was Baughman, Shacklette, and Elsenbaumer who first fully appreciated the tremendous potential of the volume changes associated with the changes in oxidation state when employed as actuators. Conducting polymer actuators show promise of outperforming mammalian muscle, but are hampered by a dependence on encapsulation in a liquid environment, as well as a consistent constitutive model. Both of these issues have been addressed in the literature (for example, see [1.35]), but there is substantial room for improvement.

Madden, et al. [1.35] have explored the material properties and performance of conducting polymer actuators. They have made substantial contributions to the field in the understanding of the fundamental actuation mechanisms, and the relationships between fundamental limiting material properties such as ionic diffusion rate, charge carriers, strain to charge ratio, and salt draining. The understanding of the limitations on performance of existing conducting polymers will provide directions for improvement in future generations.

Besides those works outlined in Section 1.1.1, many other researchers have made advances that impact the field of active materials. For example, Garikipati, et al [1.36], have treated biological tissue growth and resorption in a continuum mechanics setting. Their treatment uses balance laws and constitutive relations to deduce the relationships between multiple species (solid and fluid). They note the full extent of coupling between mass transport and mechanics that emerges from the thermodynamics. These deductions have direct analogies to the systems of polymers and interstitial fluids that will be explored extensively in the following chapters.

Smela [1.37] recently provided an excellent review of the use of electroactive polymer actuators in commercial biomedical applications. She notes the growing interest in systems with lifelike (biomimetic) movements and the difficulties that conventional actuators have in achieving these motions. Bilayer strips operating in liquid electrolytes and in air are reviewed and discussed, as well as linear actuators and microactuators. Smela asserts the usefulness of these materials in commercial applications such as blood vessel connectors, Braille displays, cochlear implants, artificial sphincters, microvalves, and steerable catheters; however, an improved understanding of how the synthesis conditions determine the material properties, as well as a predictive physics-based model that captures the dominant actuation mechanisms is needed. The future study of these materials should be focused on characterization of the actuation mechanisms, optimization of the actuator design, and consistent and thorough attention to performance metrics such as strain, stress, work, and lifetime [1.37].

1.2 Objective

The primary goal of this thesis is to develop a three-dimensional constitutive model of active polymeric materials, including changes in material volume and properties due to actuation.

1.3 Scope of the Work

This thesis first reviews the basic principles of continuum mechanics, followed by a review of the classical and current statistical mechanics based constitutive models for rubber-like materials (Chapter 2). Then, the theoretical model for reversibly swelling active polymer gels is presented (Chapter 3). Different material responses to some common loadings subject to a swelled state are then presented and discussed (Chapter 4). Next, the model is incorporated into an updated and complete solution of a problem previously addressed in the literature, the swelling of a particle-filled elastomer (Chapter 5). The theory is also applied to the classical example of a bilayer strip (Chapter 6). Finite element analysis is implemented for verification (Chapters 5) as well as the conclusion and discussion of future work (Chapter 6).

1.4 Reference

- [1.1] *Contact Lenses*, O. Dabiezies (ed.), vol. 1, 2 ed. Boston, MA: Little Brown and Company, 1988.
- [1.2] W. Kuhn, *Experimentia* 5:318, 1949.
- [1.3] J. W. Breitenbach, H. Karlinger, *Monatsh Chem* 80:211, 1949.
- [1.4] A. Katchalsky, A. Oplatka, Proc 4th Intern Cong Rheology, part 1. E. H. Lee and A. L. Copley (eds), Interscience Publishers, p. 73, 1965.
- [1.5] Y. Osada, Advances in polymer sciences. Springer, New York, 82:1, 1987.
- [1.6] D. DeRossi, K. Kajiwara, Y. Osada, A. Yamauchi (eds), Polymer gels. Plenum Press, New York, 1991.
- [1.7] Y. Osada, J. P. Gong, *Prog Polym Sci*, Pergamon Press, 18:187, 1993.
- [1.8] Y. Osada, S. B. Ross-Murphy, *Scientific American*, 268:82, 1993.
- [1.9] A. Wassermann, Size and shape changes of contractile polymers. Pergamon Press, New York, 1960.
- [1.10] A. H. Clark, S. B. Ross-Murphy, *Adv Polym Sci*, 83:57, 1987.
- [1.11] J. D. W. Madden, *Ph. D. Thesis*, MIT, Boston, MA, 2000.
- [1.12] Y. Hirose, T. Shiga, A. Okada, T. Kurauchi, "Gel actuators driven by and electrical field," *Journal of Materials Science*, vol. 28, pp. 21-26, 1993.
- [1.13] T. Shiga, Y. Hirose, A. Okada, T. Kurauchi, "Electrically driven polymer gel finger working in the air," *Journal of Intelligent Material Systems and Structures*, vol. 4, pp. 553-557, 1993.
- [1.14] Y. Osada, M. Hasebe, "Electrically activated mechanochemical devices using polyelectrolyte gels," *Chemistry Letters*, pp. 1285-1288, 1985.

- [1.15] S. P. Marra, *Ph.D. Thesis*, The Johns Hopkins University, Baltimore, MD, 2000.
- [1.16] E. S. Matsuo, T. Tanka, "Kinetics of discontinuous volume-phase transition of gels," *Journal Chemical Physics*, vol. 89, pp. 1695-1703, 1988.
- [1.17] M. Zrínyi, D. Szabó, L. Barsi, "Magnetic Field Sensitive Polymeric Actuators," Y. Osada and D. E. DeRossi (Eds.) *Polymer Sensors and Actuators*. New York, Springer, New York, pp. 385-408, 2000.
- [1.18] A. H. Mitwalli, T. A. Denison, D. K. Jackson, S. B. Leeb, T. Tanaka, "Closed-loop feedback control of magnetically-actived gels," *Journal of Intelligent Material Systems and Structures*, vol. 8, pp. 596-604, 1997.
- [1.19] A. Suzuki, T. Tanaka, "Phase transition in polymer gels induced by visible light," *Nature*, vol. 346, pp. 345-347, 1990.
- [1.20] T. Kurauchi, T. Shiga, Y. Hirose, A. Okada, "Deformation behaviors of polymer gels in electric field," *Polymer Gels Fundamentals and Biomedical Applications*, D. De Rossi, K. Kajiwara, Y. Osada, and A. Yamauchi, Eds. New York: Plenum Press, pp. 237-246, 1991.
- [1.21] R. Lumia, M. Shahinpoor, "Microgripper design using electro-active polymers," *Proceedings of the 1999 SPIE Smart Structures and Materials Symposium, Electroactive Polymer Actuators and Devices*, Y. Bar-Cohen (ed.), vol. 3669, pp. 322-329, 1999.
- [1.22] E. Smela, O. Inganäs, I. Lundström, *Science*, 268, p. 1735, 1995.
- [1.23] M. Shahinpoor, "Conceptual design, kinematics and dynamics of swimming robotic structures using ionic polymeric gel muscles," *Smart Mater Struct.*, vol. 1, pp 91-94, 1992.
- [1.24] Y. Bar-Cohen, S. Leary, M. Shahinpoor, J. O. Harrison, J. Smith, "Electro-Active Polymer (EAP) actuators for planetary applications," *Proceedings of the 1999 SPIE Smart Structures and Materials Symposium, Electroactive Polymer Actuators and Devices*, Y. Bar-Cohen (ed.), vol. 3669, pp. 57-63, 1999.
- [1.25] S. P. Marra, K. T. Ramesh, A. S. Douglas, "Characterization and modeling of compliant active materials," *Journal of the Mechanics and Physics of Solids*, Vol. 51 (9), pp. 1723-1743, 2003.
- [1.26] P. J. Flory, *Principles of Polymer Chemistry*. Ithaca, NY: Cornell University Press, 1953.
- [1.27] A. Fowler, D. J. Ellis, S. B. Warner, J. Morgan, M. Toners, "Development of Bio-Active Fabrics," *National Textile Center Brief: June 2001*, Materials Competency M00-D3, p. 22.
- [1.28] A. Katchalsky, "Rapid swelling and deswelling of reversible gels of polymeric acids by ionization," *Experimentia*, vol. 5, pp 319-320, 1949.
- [1.29] T. Tanaka, D. J. Fillmore, "Kinetics of swelling of gels," *Journal of Chemical Physics*, vol. 70, pp. 1214-1218, 1978.
- [1.30] P. Chiarelli, D. De Rossi, "Determination of mechanical parameters related to the kinetics of swelling in an electrically activated contractile gel," *Progress in Colloid and Polymer Science*, vol. 78, pp. 4-8, 1988.
- [1.31] M. Nagy, "Some new aspects of research on polymer gels," *Colloid and Polymer Science*, vol. 263, pp. 245-265, 1985.

- [1.32] F. Horkay, M. Zrínyi, “Studies on mechanical and swelling behavior of polymer networks on the basis of the scaling concept. 6. Gels immersed in polymer solutions,” *Journal of Macromolecular Science – Physics*, vol. B25, pp. 307-334, 1986.
- [1.33] J. D. Humphrey, K. R. Rajagopal, “Finite thermoelasticity of constrained elastomers subject to biaxial loading,” *Journal of Elasticity*, vol. 49, pp. 189-200, 1998.
- [1.34] R. H. Baughman, R. L. Shacklette, R. L. Elsenbaumer, “Micro electromechanical actuators based on conducting polymers,” P. I. Lazarev, Editor, Topics in Molecular Organization and Engineering, Vol. 7: Molecular Electronics. Dordrecht: Kluwer, 1991, 267.
- [1.35] P. G. A. Madden, J. D. W. Madden, P. A. Anquetil, N. A. Vandesteeg, I. W. Hunter, “The relation of conducting polymer actuator material properties to performance,” *IEEE Journal of Oceanic Engineering*, 29 (3), pp. 696-705, July 2004.
- [1.36] K. Garikipati, E. M. Arruda, K. Grosh, H. Narayanan, S. Calve, “A continuum treatment of growth in biological tissue: the coupling of mass transport and mechanics,” *Journal of the Mechanics and Physics of Solids*, IN PRESS.
- [1.37] E. Smela, “Conjugated Polymer Actuators for Biomedical Applications,” *Adv. Mater.*, 15, pp. 481-494, March 17 2003.

Chapter 2: Review of Continuum Mechanics and A Statistical Mechanics Based Constitutive Model of Rubber Elasticity

Continuum mechanics is a tool for describing the macroscopic mechanical behavior of materials. The subject of continuum mechanics roughly comprises the following basic ingredients (see for example Holzapfel [2.1], Ogden [2.2], or Slaughter [2.3]):

- (i) kinematics (the study of motion and deformation)
- (ii) balance principles (the mathematical description of the fundamental laws of physics governing the motion of a continuum; for example, mass balance and equilibrium)
- (iii) constitutive laws describing the material dependent relationships between quantities (e.g. stress-strain, stress-strain rate, strain-viscosity)

All of these ingredients take place at the microscopic level, indeed, at the atomic level. Atoms move around and stretch their bonds while exchanging energy with neighbors. But the billions (trillions!) of atoms involved in even the smallest material volumes make an atomistic approach to understanding unattainable in most situations. Continuum mechanics amounts to an approximation of the situation. Quantities like density, temperature, and velocity are all averages of a large group of atoms in a small volume of material. A very large group of data comprising all the information about each atom in a larger body is thus reduced drastically to a few useful quantities, which are more easily understood and manipulated. Let us review each of the basic ingredients in turn.

2.0 List of Symbols

The continuum mechanics notation given below will be used throughout the work, essentially following that of Gurtin [2.4]:

| | |
|--|--|
| P | Material point of a body in the reference configuration |
| $\mathbf{X}(P)$ | Vector function giving the position of point P in a reference configuration |
| $\mathbf{x}(\mathbf{X})$ | Vector function giving the position of point P in the deformed configuration |
| $\mathbf{F}(\mathbf{X}) \equiv \left(\frac{\partial \mathbf{x}}{\partial \mathbf{X}} \right)$ | Deformation gradient |
| $J = \det \mathbf{F} > 0$ | Determinant of \mathbf{F} |
| $\mathbf{F} = \mathbf{R}\mathbf{U} = \mathbf{V}\mathbf{R}$ | Polar decompositions of \mathbf{F} |
| \mathbf{U}, \mathbf{V} | Right and left stretch tensors; positive definite and symmetric |
| \mathbf{R} | Rotation tensor; proper orthogonal |
| $\lambda_i > 0$ | Principal stretches |

| | |
|---|---|
| $\mathbf{C} = \mathbf{F}^T \mathbf{F}$, $\mathbf{B} = \mathbf{F} \mathbf{F}^T$ | Right and left Cauchy-Green strain tensors |
| $\mathbf{E} = \frac{1}{2} (\mathbf{F}^T \mathbf{F} - \mathbf{I})$ | Green-Lagrange strain tensor |
| \mathbf{T} | Cauchy (true) stress tensor |
| \mathbf{P} | First Piola-Kirchhoff (nominal) stress tensor |
| $\Theta > 0$ | Absolute temperature |

2.1 Kinematics

Kinematics is the study of motion and deformation. At each instant in time, a body occupies a unique region Ω in space. One may select arbitrarily an initial time $t = 0$ at which the region Ω_0 the body occupies is called the initial configuration. It is most convenient to select an initial time at which the body is undeformed and under no external loading. This is the undeformed or *reference configuration* of the body. At some time $t > 0$, the body occupies a new region Ω_t called the deformed or *current configuration*:

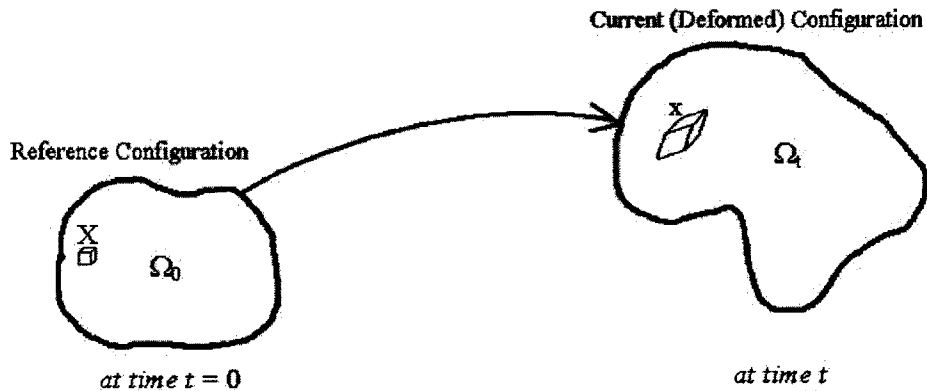


Figure 2.1: The reference and current configurations of a body occupying region Ω

The location of each particle P of material in the reference position is identified by its position vector \mathbf{X} relative to some arbitrary origin O . In the deformed configuration, the location of point P is given by the position vector \mathbf{x} . Unless otherwise noted, scalar, vector, and tensor quantities are denoted with uppercase letters in the reference configurations and lowercase letters in the current configuration.

In general, each particle in the reference configuration must have a one-to-one mapping to a particle in the deformed configuration. The *displacement* of a particle in a body relates its deformed position to its reference position:

$$\mathbf{u}(\mathbf{X}, t) = \mathbf{x}(\mathbf{X}, t) - \mathbf{X} \quad (2.1)$$

Displacements are measurable quantities. The velocity field and acceleration field may be written:

$$\mathbf{v}(\mathbf{X}, t) = \frac{\partial \mathbf{x}(\mathbf{X}, t)}{\partial t}, \quad \mathbf{a}(\mathbf{X}, t) = \frac{\partial \mathbf{v}(\mathbf{X}, t)}{\partial t} = \frac{\partial^2 \mathbf{x}(\mathbf{X}, t)}{\partial t^2} \quad (2.2)$$

Deformation occurs when there is relative displacement between internal points. The most fundamental quantity used to describe the deformation of a material point is the deformation gradient \mathbf{F} , a second-order tensor defined by

$$\mathbf{F}(\mathbf{X}) \equiv \left(\frac{\partial \mathbf{x}(\mathbf{X})}{\partial \mathbf{X}} \right) = \text{Grad } \mathbf{x}(\mathbf{X}) \quad (2.3)$$

We can rearrange the differential in (2.3) to obtain

$$\mathbf{F}(\mathbf{X})d\mathbf{X} = d\mathbf{x} \quad (2.4)$$

Equation (2.4) describes how an arbitrary line element $d\mathbf{X}$ transforms under the deformation to the line element $d\mathbf{x}$. Because a non-zero line element in the reference configuration may not be annihilated, $d\mathbf{x}$ must be non-zero and $\mathbf{F}d\mathbf{X} \neq 0$. If $\mathbf{F}d\mathbf{X} \neq 0$ for all $d\mathbf{X} \neq 0$, then \mathbf{F} is a non-singular tensor. This imposes the equivalent, but more conveniently manipulated restriction

$$\det \mathbf{F} \neq 0 \quad (2.5)$$

The volume ratio J gives the ratio of the current volume to the reference volume, and is defined by

$$J \equiv \det \mathbf{F} > 0 \quad (2.6)$$

Strain is a tensor measure of deformation independent of rotation and can be described in many ways depending on the choice of configuration used to evaluate strain as well as the manner in which stress is described (discussed later). The right and left Cauchy-Green tensors, \mathbf{C} and \mathbf{B} respectively, used predominantly throughout this work are given by:

$$\mathbf{C} = \mathbf{F}^T \mathbf{F} \quad (2.7)$$

$$\mathbf{B} = \mathbf{F} \mathbf{F}^T \quad (2.8)$$

Both strains are symmetric positive definite (such that $\mathbf{u} \cdot \mathbf{C} \mathbf{u} > 0$ for all $\mathbf{u} \neq 0$).

The *stretch* λ is the ratio of the current length of a material line element to its reference length. Because a non-zero material length in the reference configuration must have greater than zero length in any deformed configuration, $\lambda > 0$.

Any deformation characterized by \mathbf{F} may be decomposed into a pure stretch and a pure rotation. The unique polar decompositions of \mathbf{F} are:

$$\mathbf{F} = \mathbf{R} \mathbf{U} = \mathbf{V} \mathbf{R}, \quad (2.9)$$

where \mathbf{U} and \mathbf{V} are the right (or material) and left (or spatial) stretch tensors respectively. The rotation tensor \mathbf{R} is proper orthogonal ($\mathbf{R}^T \mathbf{R} = \mathbf{I}$, where \mathbf{I} is the identity tensor). The eigenvalues of the stretch tensor are the *principal stretches*, λ_i . The symmetry of \mathbf{C} and \mathbf{B} are evident by substituting \mathbf{U} and \mathbf{V} into (2.7) and (2.8):

$$\mathbf{C} = \mathbf{U}^T \mathbf{R}^T \mathbf{R} \mathbf{U} = \mathbf{U}^T \mathbf{U} = \mathbf{U}^2 \quad (2.10)$$

$$\mathbf{B} = \mathbf{V} \mathbf{R} \mathbf{R}^T \mathbf{V}^T = \mathbf{V} \mathbf{V}^T = \mathbf{V}^2 \quad (2.11)$$

Also, given that \mathbf{R} is a proper orthogonal rotation tensor, $\det \mathbf{R} = 1$. Since $\det \mathbf{F} > 0$ then

$$\det \mathbf{U} > 0 \quad (2.12a)$$

$$\det \mathbf{V} > 0 \quad (2.12b)$$

Now that we have a framework from which to understand and express the motion and deformation of a material, we must establish a method for relating that deformation to the internal forces it produces.

2.2 Stress

The motions described in the previous section give rise to interactions between neighboring material points. Important among these interactions is *stress*, a measure of the intensity of force per unit area. Stress is a second-order tensor. Different stress tensors may be defined with respect to the reference configuration, the current configuration, or some intermediate material position. Depending on the situation, a specific measure of stress may be most convenient.

A *traction vector* represents a force vector measured per unit surface area. The vector \mathbf{t} represents the force per unit area in the current configuration and is called the *Cauchy* (or *true*) *traction vector*. Whereas, the vector \mathbf{p} is the *first Piola-Kirchhoff* (or *nominal*) *traction vector*, as reproduced from [2.1] in Figure 2.2, and is defined in the reference configuration as the force per unit reference area:

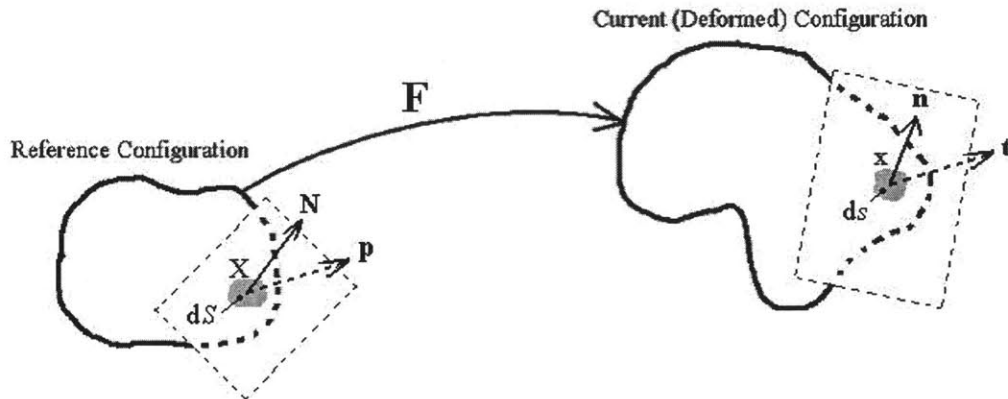


Figure 2.2: Traction vectors acting on infinitesimal surface elements with outward unit normals [2.1]

Figure 2.2 shows an imaginary plane cutting through a body intersecting the material point given by \mathbf{X} . In the reference configuration, the vector \mathbf{N} is the unit vector normal to the cutting surface S . The nominal traction vector \mathbf{p} is associated with infinitesimal area dS at point \mathbf{X} . In the current configuration, the Cauchy

traction vector \mathbf{t} points in the same direction as \mathbf{p} and is associated with the current infinitesimal area ds and the unit normal \mathbf{n} .

Cauchy's stress theorem states that there exist unique second-order tensor fields \mathbf{T} and \mathbf{P} such that

$$\mathbf{t}(\mathbf{x}, t, \mathbf{n}) = \mathbf{T}(\mathbf{x}, t)\mathbf{n}, \quad (2.13)$$

and

$$\mathbf{p}(\mathbf{X}, t, \mathbf{N}) = \mathbf{P}(\mathbf{X}, t)\mathbf{N}, \quad (2.14)$$

where \mathbf{T} is the *Cauchy* (or *true*) *stress tensor* and \mathbf{P} symbolizes the *first Piola-Kirchhoff* (or *nominal*) *stress tensor*.

The two stresses are alternative representations of the same state of stress; if given one, the other can be determined using Nanson's formula. Nanson's formula is a relation between a material surface in the reference and current configurations (see for example [2.1] – [2.4]). It maps a surface area and its normal from reference configuration to current configuration:

$$ds = J \mathbf{F}^{-T} dS \quad (2.15)$$

Using Nanson's formula, the two stresses in (2.13) and (2.14) are related:

$$\mathbf{P} = J \mathbf{T} \mathbf{F}^{-T}, \quad (2.16)$$

or

$$\mathbf{T} = \mathbf{T}^T = J^{-1} \mathbf{P} \mathbf{F}^T \quad (2.17)$$

As with any second-order tensor, we may solve the eigenvalue problem to obtain principal stresses and principal directions:

$$[\mathbf{T} - T_i \mathbf{1}]\mathbf{n}_i = \mathbf{0}; \quad \text{for } |\mathbf{n}_i| = 1, \quad (2.18)$$

where T_i are the three principal normal stresses that correspond to three principal directions specified by eigenvectors \mathbf{n}_i .

2.3 Constitutive Equations

A constitutive theory attempts to model real behavior of materials using mathematical models. The principles of statistical mechanics, along with the laws of thermodynamics, are used to model polymer networks, as developed in the following sections.

2.3.1 Statistical Mechanics

The statistical mechanics treatment begins with the assumption of a material structure consisting of randomly oriented long molecular chains. The direction in space of each link in the polymer chain is entirely random and bears no relation to the direction of any other link in the chain. To visualize the situation, one may picture, for example, a molecule of polyethylene containing thousands of C-C bonds. Each of these bonds has a rotational degree of freedom along one axis. Because the number of links in the chain, n , is very large (ranging from 10^2 to 10^9) and each link has a degree of flexibility, the chain will take on a randomly kinked shape. It is appropriate to picture this randomly kinked chain as a very long piece of string. Using the random walk model and classic statistical arguments (e.g. refer to Flory [2.5] or Doi [2.6]), we may write the probability distribution of the end-to-end length, r , of an isolated polymer chain as:

$$p(r) = \left(\frac{3}{2\pi nl^2} \right)^{3/2} \exp\left(\frac{-3r^2}{2nl^2} \right), \quad (2.19)$$

where l is the length of each link in the chain [2.7]. The probability distribution in (2.19) is well known – it is a Gaussian statistical distribution. The probability density of a chain lying between r and $r+dr$ is

$$P(r) = 4\pi r^2 p(r) \quad (2.20)$$

A typical example of this distribution is given in Figure 2.3:

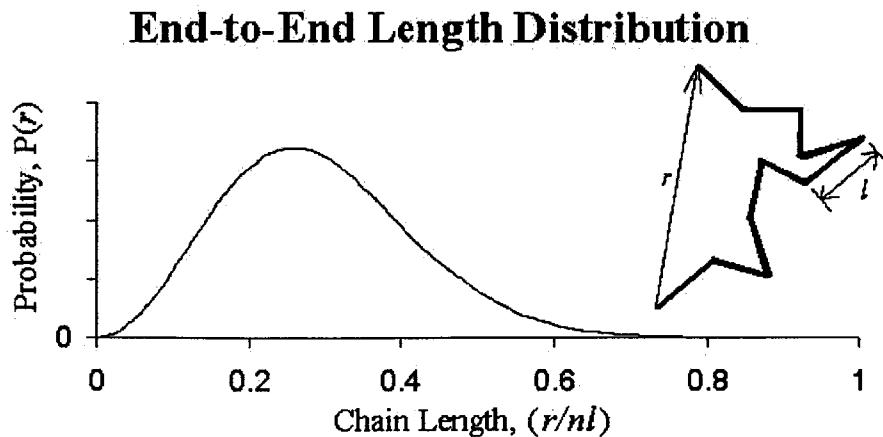


Figure 2.3: The Gaussian statistical distribution of polymer chain end-to-end lengths.

The entropy of the statistical chain is found according to the general principles of statistical thermodynamics from the Boltzmann result that the entropy of a system is proportional to the logarithm of the number of configurations available to it. If we fix one end of the chain at the origin and the other within a small volume element $d\tau$, the number of configurations available is given by the probability density multiplied by that volume element, $p(r)d\tau$. Therefore, the entropy of a single chain is

$$s = k_B \ln(p(r)d\tau), \quad (2.21)$$

where k_B is Boltzmann's constant.

Next, we substitute the probability function from (2.19) to obtain the entropy for a single chain:

$$s = k_B \left\{ \frac{3}{2} \ln \left(\frac{3}{2\pi n l^2} \right) - \frac{3r^2}{2nl^2} + \ln(d\tau) \right\} \quad (2.22)$$

Under tension, each polymer chain stretches to accommodate the deformation. Because this stretching reduces the number of possible configurations the chain can take, the configurational entropy will decrease. It is important to note that the tension in the chain is not caused by a change in energy, but by the change in entropy. The release of this tension acts to return the chain to a state with more allowable configurations, a state with higher entropy. It is for this reason that polymer chains are sometimes called entropy springs.

The entropy of a single chain, as derived in (2.22), is a useful result from which to derive the change in entropy of a polymer network under some arbitrary deformation. Kuhn [2.8] recognized the fact that the elasticity of rubber (perhaps the most common and most studied of the polymer gels) derives from the thermal motion of the polymer chains. He derived a simple but physically insightful classical theory of rubber elasticity that is still practical today. It hinged on a few critical assumptions, the validity of which will be explored.

The fundamental assumptions based on the original theory of Kuhn are reproduced here as they are given in [2.9]:

1. The network contains N_c chains per unit volume, a chain being defined as the segment of molecule between successive points of cross-linkage. A cross-link is a chemical junction point between molecular chains. Cross-linking produces a coherent network that does not allow all the molecules to move independently, as they would in a liquid.
2. The average squared initial end-to-end distance between cross-linkage sites is taken to be the root-mean square end-to-end distance, $\langle r_0^2 \rangle$. Applying (2.21) to this definition implies:

$$\langle r_0^2 \rangle = \frac{\int_0^\infty r^2 P(r) dr}{\int_0^\infty P(r) dr} = nl^2 \quad (2.23)$$

3. There is no change of volume due to mechanical loading.
4. The network deforms affinely: the components of length of each chain are assumed to deform microscopically in the same ratio as the corresponding dimensions of the macroscopic material.
5. The entropy of the network is the sum of the entropies of each individual chain, as given in (2.22).

Stretching a chain from its initial length, r_0 , to its deformed length, r , results in a change in entropy. To illustrate, suppose a rectilinear coordinate system is employed such that

$$\langle r_0^2 \rangle = \langle x_{10}^2 \rangle + \langle x_{20}^2 \rangle + \langle x_{30}^2 \rangle, \quad (2.24)$$

and the current end-to-end length is thus given by

$$\langle r^2 \rangle = \langle x_1^2 \rangle + \langle x_2^2 \rangle + \langle x_3^2 \rangle, \quad (2.25)$$

where the $\langle \rangle$ indicate the expected or average value of the expression within.

The change in entropy of a single chain due to deformation is determined by comparing the entropy of the deformed position (also called the “current configuration”) to the entropy of the initial position (also called the “reference configuration”) using equation (2.22):

$$\Delta s = s - s_0 = k_B \left\{ \frac{3}{2} \ln \left(\frac{3}{2\pi nl^2} \right) - \frac{3r^2}{2nl^2} + \ln(d\tau) \right\} - k_B \left\{ \frac{3}{2} \ln \left(\frac{3}{2\pi nl^2} \right) - \frac{3r_0^2}{2nl^2} + \ln(d\tau_0) \right\} \quad (2.26)$$

Note that the first term from (2.22) cancels out. It is constant because the number of bonds and the bond length for a given molecule do not change in the current context. Furthermore, in actual practice we are only concerned with the differences of entropy between two states, so this term will always be ignorable.

This reduces (2.26) to the following, upon rearranging terms:

$$\Delta s = k_B \left\{ -\frac{3r^2}{2nl^2} + \frac{3r_0^2}{2nl^2} \right\} + k_B \left\{ \ln \left(\frac{d\tau}{d\tau_0} \right) \right\} \quad (2.27)$$

For the moment, let us adhere to the incompressibility assumption 3 above and conclude that the differential volume element, $d\tau$, must remain the same in the deformed and reference configurations, and thus drop the volume ratio term from (2.27). We are left with a simplified version of the change in entropy for a single chain:

$$\Delta s = -k_B \left\{ \frac{3}{2nl^2} (r^2 - r_0^2) \right\} \quad (2.28)$$

The affine deformation assumption implies that the deformed configuration of a material point may be simply represented, as in (2.25), in terms of its reference position and the macroscopic principal stretch components:

$$\langle r^2 \rangle = \langle x_1^2 \rangle + \langle x_2^2 \rangle + \langle x_3^2 \rangle = \langle \lambda_1^2 x_{10}^2 \rangle + \langle \lambda_2^2 x_{20}^2 \rangle + \langle \lambda_3^2 x_{30}^2 \rangle \quad (2.29)$$

Observe that (2.28) may now be rewritten in terms of its components as

$$\Delta s = -k_B \left\{ \frac{3}{2nl^2} (x_{10}^2 (\lambda_1^2 - 1) + x_{20}^2 (\lambda_2^2 - 1) + x_{30}^2 (\lambda_3^2 - 1)) \right\} \quad (2.30)$$

The vector r_0 , whose length is given by $r_0^2 = x_{10}^2 + x_{20}^2 + x_{30}^2$, has no preference for any direction. Therefore, the components of r_0 must be indistinguishable and so must, on average, be of equal length:

$$x_{10}^2 = x_{20}^2 = x_{30}^2 = \frac{r_0^2}{3} \quad (2.31)$$

Using this observation, (2.30) is generalized to

$$\Delta s = -k_B \left\{ \frac{3}{2nl^2} \left(\frac{r_0^2}{3} (\lambda_1^2 + \lambda_2^2 + \lambda_3^2 - 3) \right) \right\} \quad (2.32)$$

We can further simplify (2.32) by incorporating assumption 2 for the representative value of the initial chain length, $\langle r_0^2 \rangle = nl^2$

$$\Delta s = -k_B \left\{ \frac{1}{2} (\lambda_1^2 + \lambda_2^2 + \lambda_3^2 - 3) \right\} \quad (2.33)$$

Finally, if there are N_c chains per unit volume, as stipulated in assumption 1, and if the total entropy of the network is the sum of the entropies of each individual chain, as required by assumption 5, then the total change in entropy of the network per unit reference volume in terms of the principal stretch state is

$$\Delta S = -\frac{1}{2} N_c k_B (\lambda_1^2 + \lambda_2^2 + \lambda_3^2 - 3). \quad (2.34)$$

If we relax assumption 3 and allow for a volume change, the additional term found in (2.26) is relevant. Following the same procedure as above (see for example Wall and Flory [2.10], Flory [2.11], Bischoff *et al.* [2.12]), the total entropy change including the effects of volume change is

$$\Delta S = -\frac{1}{2} N_c k_B (\lambda_1^2 + \lambda_2^2 + \lambda_3^2 - 3) + N_c k_B \ln(J) \quad (2.35)$$

where $J = \lambda_1 \lambda_2 \lambda_3 = \sqrt{I_3}$ is the volume ratio. This term is usually negligible for purely mechanical loadings, however it is significant for the proper development of the swelling framework to be discussed in the next chapter.

2.3.2 Strain-Energy Functions

2.3.2.1 Thermodynamics

The elastic strain energy function for a material may be developed using thermodynamic principles in conjunction with (2.35). From the first law of thermodynamics, the change in internal energy Δe of a process per unit mass is

$$\Delta e = \Delta Q + \Delta W \quad (2.36)$$

where ΔQ is the heat absorbed by the system and ΔW is the work done on the system by external forces. If we assume the material is purely elastic (i.e. the material returns reversibly to its reference configuration upon unloading), then the second law defines the entropy change ΔS :

$$\Theta \Delta S = \Delta Q, \quad (2.37)$$

where Θ is the absolute temperature.

For an *ideal* rubber, internal energy is assumed to be a function of Θ alone (see for example Treloar [2.9] chapters 2 and 13). Consequently, for a given reference temperature the change in internal energy, e , during an isochoric deformation \mathbf{F} is zero [2.1]:

$$e(\mathbf{F})|_{\Theta} = 0 \quad (2.38)$$

Now (2.36) may be simplified,

$$-\Delta Q = \Delta W, \quad (2.39)$$

and (2.37) may be substituted,

$$\Delta W = -\Theta \Delta S. \quad (2.40)$$

Substituting the change of entropy derived from the Gaussian statistical mechanics approach in (2.34), the work done on the polymer network to deform it from the stress-free reference position to the current deformed position for an isochoric deformation is

$$U_G = \frac{1}{2} N_c k_B \Theta (\lambda_1^2 + \lambda_2^2 + \lambda_3^2 - 3). \quad (2.41)$$

A subscript is used in (2.41) and henceforth to indicate which statistical model the strain-energy was derived from. In this case, U_G indicates a form obtained using Gaussian statistics.

To account for the usually negligible compressibility effects, we must include the additional entropy term due to volume change from (2.35):

$$U_G = \frac{1}{2} N_c k_B \Theta (\lambda_1^2 + \lambda_2^2 + \lambda_3^2 - 3) - N_c k_B \Theta \ln(J) \quad (2.42)$$

Incompressibility is often assumed because intermolecular interactions provide a high stiffness resisting volume change, as evidenced by a large bulk modulus for polymer gels. When compressibility effects are included, the strain-energy function must also include the internal energy contribution to volume change, expressed as

$$e = \frac{1}{2} K_B (J - 1)^2, \quad (2.43)$$

where K_B is the bulk modulus.

Thus, the final form for the Gaussian strain-energy function, including compressibility effects is

$$U_G = \frac{1}{2} N_c k_B \Theta (\lambda_1^2 + \lambda_2^2 + \lambda_3^2 - 3) - N_c k_B \Theta \ln(J) + \frac{1}{2} K_B (J - 1)^2 \quad (2.44)$$

The Gaussian statistical model is appropriate at small to medium stretches. Referring back to (2.19) and Figure 2, the magnitude of the stretch in the polymer chains may be quantified by r/nl , where l is the length of each chain link, n is the number of links in the chain, and r is the end-to-end length of a particular polymer chain. As the individual polymer chains approach the limits of their extensibility ($r/nl \rightarrow 1$), equation (2.19) no longer applies and the “non-Gaussian” behavior of the material dominates the statistical distribution of the chain lengths. This non-Gaussian transition becomes apparent for $r/nl \approx 0.4$ [5]. Additional chain statistics must be utilized to accurately model the locking behavior of the polymer chains in this regime. Many other hyperelastic models attempt to account for these changes. For example, Arruda and Boyce [2.13] present the “8-chain” model that incorporates a locking stretch for large deformations via Langevin statistics. The 8-chain model can be visualized as a unit cube with polymer chains of length $r_0 = \sqrt{nl}$ on each diagonal connecting the geometric center to each vertex at an initial angle θ_0 , as in Figure 2.4.

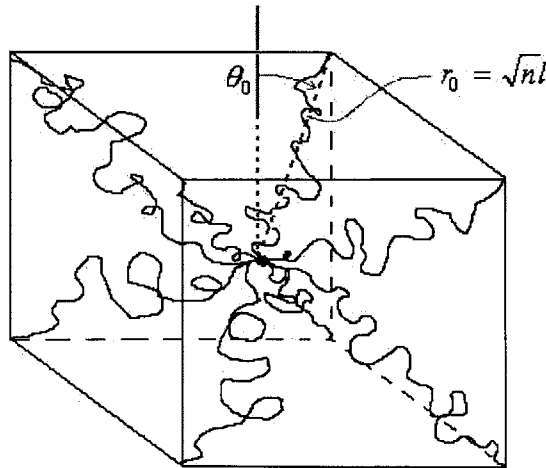


Figure 2.4: 8-chain model representative volume element

Each chain is initially of length r_0 . When the material is deformed, the chains stretch by λ_c and rotate from initial angle θ_0 to angle θ to accommodate the deformation, as shown (in 2-dimensions) in Figure 2.5:

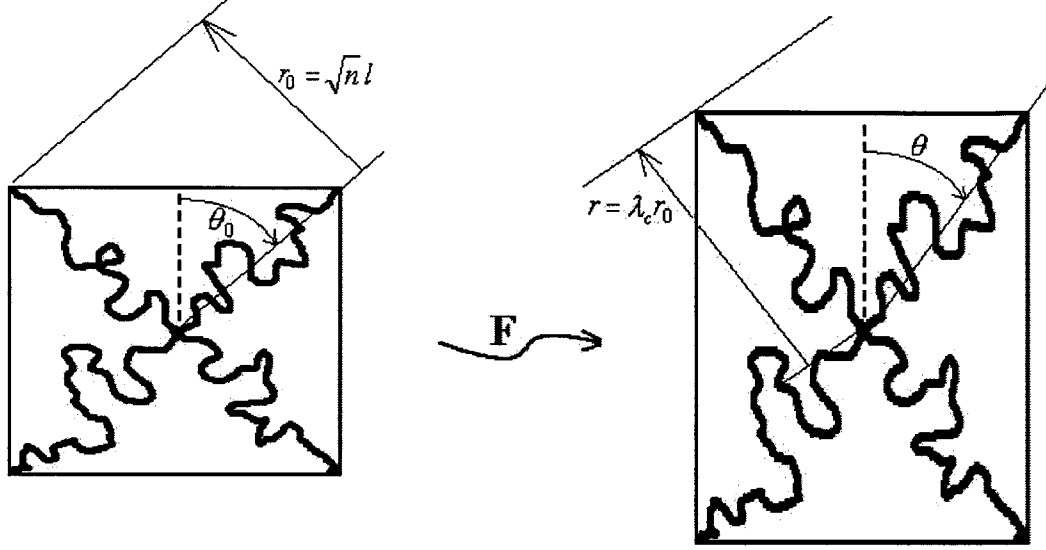


Figure 2.5: Deformation of the 8-chain polymer network under a tension loading.

From kinematical arguments, it can be shown that the stretch on each chain in the network is identical in magnitude, and equal to the root mean square of the principal stretches:

$$\lambda_{chain} = \left[\frac{1}{3} (\lambda_1^2 + \lambda_2^2 + \lambda_3^2) \right]^{1/2} = \frac{\sqrt{I_1}}{\sqrt{3}} \quad (2.45)$$

Using Langevin statistics, the resulting strain energy function in the case of incompressibility is given by:

$$U_{8ch} = N_c k_B \Theta \sqrt{n} \left[\beta_{chain} \lambda_{chain} + \sqrt{n} \ln \left(\frac{\beta_{chain}}{\sinh \beta_{chain}} \right) \right] \quad (2.46)$$

$$\beta_{chain} = L^{-1} \left(\frac{\lambda_{chain}}{\sqrt{n}} \right) \quad (2.47)$$

where the inverse of the Langevin function, defined as $L(\gamma) \equiv \coth \gamma - 1/\gamma$, models the locking of the polymer chains at high stretches. Including compressibility effects, the additional entropy term due to volume change, and the intermolecular energy term, the strain-energy function is

$$U_{8ch} = N_c k_B \Theta \sqrt{n} \left[\beta_{chain} \lambda_{chain} + \sqrt{n} \ln \left(\frac{\beta_{chain}}{\sinh \beta_{chain}} \right) + \frac{\beta_0}{3} \ln \left(\frac{1}{J} \right) \right] + \frac{1}{2} K_B (J - 1)^2, \quad (2.48)$$

where $\beta_0 = L^{-1} \left\{ \frac{1}{\sqrt{n}} \right\}$ and K_B is the bulk modulus.

2.3.2.2 Stress

Incompressible Materials

The principal values of the Cauchy (true) stress can be obtained by proper differentiation of the strain energy density function:

$$T_i = \lambda_i \frac{\partial U}{\partial \lambda_i} - p^* \quad [\text{no sum on } i], \quad (2.49)$$

where p^* is the additional pressure determined by satisfying boundary conditions for an incompressible material [2.13]. Equivalently, noting that the incompressible form of the Gaussian model is only dependent on I_1 , the Cauchy Stress tensor may be expressed in terms of the left Cauchy-Green tensor given in (2.8) by

$$\mathbf{T} = 2 \frac{\partial U}{\partial I_1} \mathbf{B} - p^* \mathbf{1} \quad (2.50)$$

Incompressible Gaussian Material

In the Gaussian material described by (2.41), the Cauchy stress predicted by Gaussian statistics for an incompressible material is

$$T_i = N_c k_B \Theta \lambda_i^2 - p^* \quad (2.51)$$

$$\mathbf{T} = N_c k_B \Theta \mathbf{B} - p^* \mathbf{1} \quad (2.52)$$

Incompressible 8-chain (Non-Gaussian) Material

Additionally, (2.49) may be differentiated using (2.46) for the strain-energy function to obtain the Cauchy stress corresponding to the 8-chain model. We start by defining

$$\chi \equiv \frac{dL^{-1}\left(\frac{\lambda_{ch}}{\sqrt{n}}\right)}{d\lambda_{ch}}, \quad (2.53)$$

where $\lambda_{ch} = \lambda_{chain}$ from (2.45).

Recalling (2.47), we may write

$$L(\beta) = L\left(L^{-1}\left(\frac{\lambda_{ch}}{\sqrt{n}}\right)\right) = \frac{\lambda_{ch}}{\sqrt{n}}. \quad (2.54)$$

Using the chain rule,

$$\frac{dL}{d\beta} \frac{d\beta}{d\lambda_{ch}} = \frac{d\left(\frac{\lambda_{ch}}{\sqrt{n}}\right)}{d\lambda_{ch}}, \quad (2.55)$$

which is equivalent to

$$\left(\frac{-1}{\sinh^2 \beta} + \frac{1}{\beta^2} \right) \frac{d\beta}{d\lambda_{ch}} = \frac{1}{\sqrt{n}}. \quad (2.56)$$

Thus we conclude that

$$\chi = \frac{dL^{-1}\left(\frac{\lambda_{ch}}{\sqrt{n}}\right)}{d\lambda_{ch}} = \frac{d\beta}{d\lambda_{ch}} = \frac{1}{\sqrt{n}} \left(\frac{\beta^2 \sinh^2 \beta}{\sinh^2 \beta - \beta^2} \right) \quad (2.57)$$

Using this result, we can solve (2.49) using the 8-chain model:

$$\begin{aligned} T_i + p^* &= \lambda_i \frac{\partial U_{8ch}}{\partial \lambda_i} = \lambda_i \frac{\partial U_{8ch}}{\partial \lambda_{ch}} \frac{\partial \lambda_{ch}}{\partial \lambda_i} \\ &= N_c k_B \Theta \sqrt{n} \lambda_i \left\{ \lambda_{ch} \frac{\partial \beta}{\partial \lambda_{ch}} + \beta + \sqrt{n} \frac{\sinh \beta}{\beta} \left(\frac{\frac{\partial \beta}{\partial \lambda_{ch}} (\sinh \beta - \beta \cosh \beta)}{\sinh^2 \beta} \right) \right\} \frac{\partial \lambda_{ch}}{\partial \lambda_i} \end{aligned} \quad (2.58)$$

If we note that $\frac{\partial \lambda_{ch}}{\partial \lambda_i} = \frac{\lambda_i}{3\lambda_{ch}}$, and use the result of (2.57), we can write the complete expression for the Cauchy stress obtained from differentiation of the 8-chain model strain energy function as:

$$T_i = \frac{N_c k_B \Theta \sqrt{n} \lambda_i^2}{3\lambda_{ch}} \left(\left(\frac{\beta^2 \sinh^2 \beta}{\sinh^2 \beta - \beta^2} \right) \left(\frac{\lambda_{ch}}{\sqrt{n}} + \frac{1}{\beta} - \frac{\cosh \beta}{\sinh \beta} \right) + \beta \right) - p^* \quad (2.59)$$

The expression can be further simplified by noting that the underlined term in (2.59) cancels itself exactly. Thus we are left with a simple form for the Cauchy stress, more appropriate for use in moderate and high stretching regimes:

$$T_i = \frac{N_c k_B \Theta \sqrt{n}}{3\lambda_{ch}} \beta \lambda_i^2 - p^* \quad (2.60)$$

The Cauchy stress tensor can be similarly derived and is found to be

$$\mathbf{T} = \left(\frac{N_c k_B \Theta \sqrt{n}}{3\lambda_{ch}} \beta \right) \mathbf{B} - p^* \mathbf{1} \quad (2.61)$$

Compressible Materials

For a compressible material, in general $J = \lambda_1 \lambda_2 \lambda_3 \neq 1$, and the form of (2.49) and (2.50) is slightly modified [2.2]:

$$T_i = J^{-1} \lambda_i \frac{\partial U}{\partial \lambda_i}, \quad [\text{no sum on } i] \quad (2.62)$$

or

$$\mathbf{T} = J^{-1} \frac{\partial U}{\partial I_1} \mathbf{B} + \frac{\partial U}{\partial J} \mathbf{1}. \quad (2.63)$$

Compressible Gaussian Material

Substituting the complete Gaussian strain-energy function from (2.44) yields the predicted Cauchy stress including compressibility effects:

$$T_i = J^{-1} N_c k_B \Theta (\lambda_i^2 - 1) + K_B (J - 1), \quad (2.64)$$

or

$$\mathbf{T} = J^{-1} N_c k_B \Theta (\mathbf{B} - \mathbf{I}) + K_B (J - 1) \mathbf{I}. \quad (2.65)$$

Compressible 8-chain (Non-Gaussian) material

For the compressible 8-chain material, the strain-energy function in (2.48) is differentiated and the Cauchy stress is modified, giving

$$T_i = \frac{J^{-1} N k_B \Theta \sqrt{n} \lambda_i^2}{3 \lambda_{ch}} \beta - \frac{1}{3} N k_B \Theta \sqrt{n} \beta_0 + K_B (J - 1), \quad (2.66)$$

or

$$\mathbf{T} = \left(\frac{J^{-1} N k_B \Theta \sqrt{n}}{3 \lambda_{ch}} \beta \right) \mathbf{B} - \frac{1}{3} N k_B \Theta \sqrt{n} \beta_0 \mathbf{1} + K_B (J - 1) \mathbf{I}. \quad (2.67)$$

2.4 Reference

- [2.1] G. A. Holzapfel, Nonlinear Solid Mechanics: A Continuum Approach for Engineering. Chichester, New York: Wiley, 2000.
- [2.2] R. W. Ogden, Non-Linear Elastic Deformations. Mineola, New York: Dover Publications, 1984.
- [2.3] W. S. Slaughter, The Linearized Theory of Elasticity. Boston, Birkhauser, 2002.
- [2.4] M. E. Gurtin, An Introduction to Continuum Mechanics. New York: Academic Press, 1981.
- [2.5] P. J. Flory, Principles of Polymer. New York: Oxford University Press, 1975.
- [2.6] M. Doi, Introduction to Polymer Physics. Oxford: Clarendon Press, 1996.
- [2.7] J. S. Bergström and M. C. Boyce, "Deformation of Elastomeric Networks: Relation between Molecular Level Deformation and Classical Statistical Mechancis Models of Rubber Elasticity," *Macromolecules*, **34**, 614, 2001.
- [2.8] Kuhn From 1934.
- [2.9] L. R. G. Treloar, The Physics of Rubber Elasticity. New York: Oxford University Press, 1975.
- [2.10] F. T. Wall and P. J. Flory, "Statistical thermodynamics of rubber elasticity," *J. Chem. Phys.*, **19**, 1435, 1951.
- [2.11] P. J. Flory, "Thermodynamic relations for high elastic materials." *Trans. Faraday Soc.*, **57**, 829, 1961.
- [2.12] J. E. Bischoff, E. M. Arruda, and K. Grosh, "A new constitutive model for the compressibility of elastomers at finite deformations," *Rubb. Chem. Techn.*, **74**, 541, 2001.
- [2.13] E. M. Arruda and M. C. Boyce, "Constitutive models of rubber elasticity: A review," *Rubber Chemistry and Technology*, **73**, 505, 2000.

Chapter 3: Swelling

The mechanics of swelling of elastomeric materials has been extensively addressed in the literature and is reasonably well understood. Recent interest in the mechanics of active polymers, gels, and soft biological tissues has led to a renewed interest in the mechanics of swelling of polymeric and polymeric-like materials where reversible swelling is the primary functional activation mechanism of many of these materials. This chapter provides a continuum mechanics framework for swelling and stretching of elastomeric materials while retaining the underlying statistical mechanics treatment of deformation of macromolecular networks.

Swelling of a macromolecular network acts to alter its mechanical response; in turn, mechanical loading also has some influence on swelling. The thermodynamics and mechanics of swelling and the influence of swelling on mechanical stretching are well documented in Flory and Rehner [3.1], Flory [3.2], Treloar [3.3], and Treloar [3.4]. A brief review of various statistical mechanics based models of this phenomenon was recently provided in Boyce and Arruda [3.5]. As background, we detail the mechanics of swelling and mechanical stretching of an isotropic macromolecular network in the context of a finite deformation kinematics framework for a Gaussian material. A few illustrating examples of the effect of swelling on mechanical stretching are then presented. This framework will then be utilized in Chapter 5 for a micromechanics model of swelling in filled elastomers and gels, and in Chapter 6 for the deflection of a bilayer strip caused by swelling of one of the layers.

3.1 Kinematics

The kinematic framework will begin by noting that swelling is a macroscopically stress-free process (as will be discussed below, swelling results in internally balanced stresses where osmotic pressure is balanced by macromolecular tension, but macroscopically the swelling process is stress-free). Furthermore, we begin by focusing our study on principal stretch deformations only (this will be generalized later). Therefore, the deformation gradient is taken to be rotation free and will be expressed, for now, in terms of principal stretch components Λ_i . The deformation gradient can be multiplicatively decomposed into mechanical (elastic) and swelling components (e.g. see [3.4] and [3.5]) as shown in Figure 3.1:

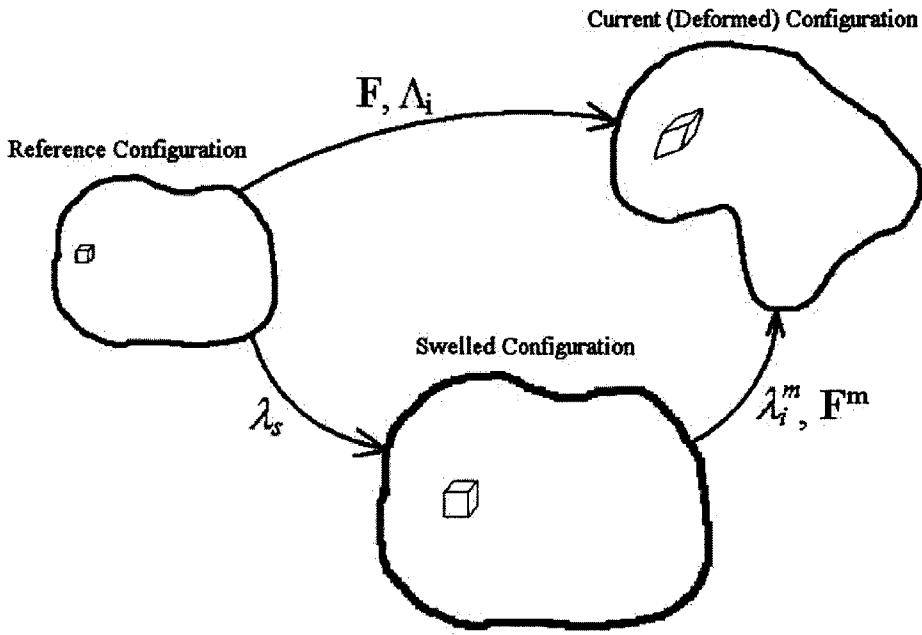


Figure 3.1: Schematic representation of the multiplicative decomposition, $\Lambda_i = \lambda_i^m \lambda_s$

The decomposition in Figure 3.1 is represented mathematically as

$$\Lambda_i = \lambda_i^m \lambda_s \quad (3.1)$$

where Λ_i are the principal values of the total stretch, λ_i^m are the principal values of the mechanical stretch, and λ_s is the isotropic swelling stretch. Thus the volumetric swelling ratio is $J_s = \frac{V_s}{V_0} = \lambda_s^3$. Note that in the polymer physics and chemistry literature, swelling is typically given with respect to the dry state and is expressed in terms of volume fraction of polymer with respect to the dry state, v_p ; thus, $\lambda_s = v_p^{-1/3}$.

The multiplicative decomposition can be conceptualized in two ways: (1) the elastomer is first swelled by λ_s and then subjected to mechanical stretch λ_1^m ; or (2) the polymer is subjected to both swelling and mechanical stretching, whereby λ_s is the configuration achieved upon elastically unloading to a macroscopically stress free state. In either event, it is important to recognize that the intermediate configuration λ_s is not only one of different volume, but also one with different properties due to the isotropically expanded (stretched) state of the macromolecular network. The effect of swelling on properties will be detailed below in the discussion of the statistical mechanics and thermodynamics of swelling.

This kinematic framework is easily generalized to arbitrary finite deformations as described by the deformation gradient, \mathbf{F} , where $\mathbf{F} = \frac{\partial \mathbf{x}}{\partial \mathbf{X}}$, where \mathbf{x} is the current position of a material point and \mathbf{X} is the reference position. \mathbf{F} may be multiplicatively decomposed into mechanical and swelling gradients:

$$\mathbf{F} = \mathbf{F}^m \mathbf{\Lambda}_s, \quad (3.2)$$

where the swelling deformation gradient, $\mathbf{\Lambda}_s = \lambda_s \mathbf{I}$, is a diagonal stretch tensor of equal components; \mathbf{F}^m is the mechanical deformation gradient which can be multiplicatively polar decomposed into rotation and stretch components

$$\mathbf{F}^m = \mathbf{R}^m \mathbf{U}^m = \mathbf{V}^m \mathbf{R}^m. \quad (3.3)$$

The mechanical left Cauchy Green tensor is given by:

$$\mathbf{B}^m = \mathbf{F}^m \mathbf{F}^{mT} \quad (3.4)$$

The total stretch invariants and corresponding mechanical stretch invariants are

$$\begin{aligned} I_1 &= \text{trace}(\mathbf{B}) = \Lambda_1^2 + \Lambda_2^2 + \Lambda_3^2, \\ I_2 &= (\text{trace } \mathbf{B})^2 - \text{trace } (\mathbf{B}^2) = \Lambda_1^2 \Lambda_2^2 + \Lambda_2^2 \Lambda_3^2 + \Lambda_1^2 \Lambda_3^2, \\ I_3 &= \det(\mathbf{B}) = (\Lambda_1 \Lambda_2 \Lambda_3)^2; \end{aligned} \quad (3.5a)$$

and,

$$\begin{aligned} I_1^m &= \text{trace}(\mathbf{B}^m) = \lambda_1^2 + \lambda_2^2 + \lambda_3^2, \\ I_2^m &= (\text{trace } \mathbf{B}^m)^2 - \text{trace } (\mathbf{B}^{m2}) = \lambda_1^2 \lambda_2^2 + \lambda_2^2 \lambda_3^2 + \lambda_1^2 \lambda_3^2, \\ I_3^m &= \det(\mathbf{B}^m) = (\lambda_1 \lambda_2 \lambda_3)^2. \end{aligned} \quad (3.5b)$$

3.2 Constitutive Equations of Swelling Behavior

3.2.1 Statistical Mechanics of Swelling

Macroscopically, swelling involves the influx of liquid into a material. Perhaps the most accessible example is the swelling of a sponge in water. The sponge starts out in a dry (reference) state and swells into a wet (swollen) state. In general, this transformation is accompanied by a change in material properties and dimensions. The typical and most familiar response is a softer sponge with an increased volume.

Microscopically, the picture is more subtle and complex. Let us examine the polymer gel developed in the previous sections. When immersed in a liquid, fluid ions will migrate into the polymer network. As these particles insert themselves into the polymer matrix, contending forces will equilibrate. The force that drives the influx is derived from the entropy of mixing. Using statistical thermodynamics, it is simple to show that particles of different types prefer a completely mixed state. The classical example involves two different pure gases in a chamber with a partition between them. When the partition is removed, the tendency to maximize entropy results in a uniform mixture. The greater entropy of the mixture as compared with the pure separated components arises entirely from the greater number of arrangements available in the solution. If there are n_1 particles of one gas and n_2 particles of the other, the total change in entropy from the unmixed state to the completely mixed state is [3.2]:

$$\Delta S_M = -k_B (n_1 \ln v_1 + n_2 \ln v_2) \quad (3.6)$$

where $v_i = \frac{n_i}{n_1 + n_2}$ is the number fraction of the i^{th} specie or, more conveniently, when the particles are of the same size, the volume fraction. The entropy change in (3.6) is called the entropy of mixing.

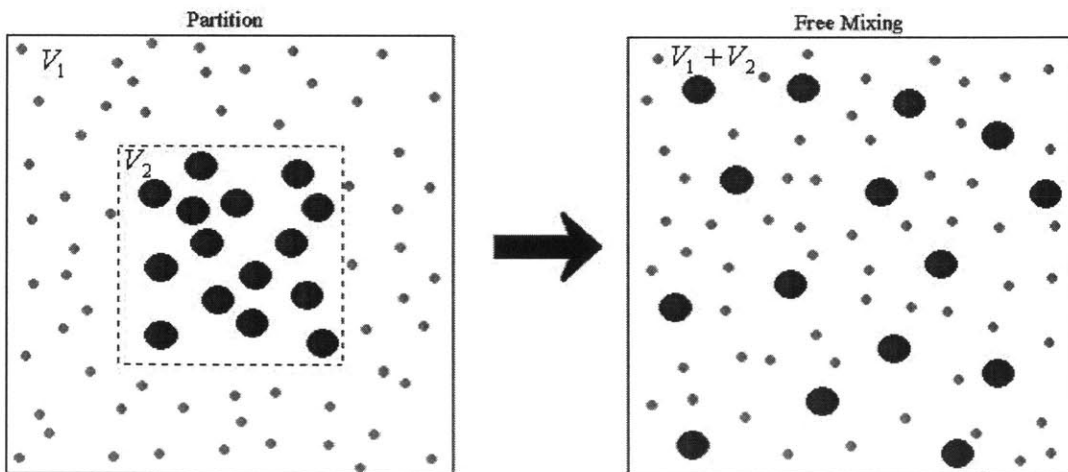


Figure 3.2: A rigid chamber with two types of particles initially separated and then allowed to mix.

Figure 3.2 shows a simplified representation of the mixing of particles in a rigid container of volume $V_1 + V_2$. In this example, there are two species of particles, with $n_1 > n_2$. A partition divides the two “gases” and is subsequently removed to allow the particles to freely mix. The entropy of the system is maximized by the random motions of the particles – more configurations are available to the system, so the entropy has increased.

Ideal gases are modeled as point particles that are chemically inert. But in the case of the polymer gel, the mixing particles are constrained. Furthermore, the expression for the entropy of mixing in (3.6) assumes an approximate interchangeability of the molecules in the solution, which cannot hold for polymer solutions in which the polymer molecules are thousands or more times the size of the solvent molecules. Flory [3.6] considers the long chain molecule to be composed of x chain segments, each of which is equal in size to a solvent molecule. Using this convenient definition of x , the ratio of the molar volumes of the solute and solvent, the assumptions required to analyze the polymer solution are equivalent to the those of the simple mixing of ideal gases. The insertion of each ion stretches the polymer network, and also gives rise to local intermolecular forces. At the equilibrium point, the entropy increase from mixing is balanced exactly by a decrease in entropy due to the stretching of the polymer chains, and so it is no longer thermodynamically favorably for the material to take on more fluid. The tension developed by the chain stretching is balanced by the *osmotic pressure* of the fluid. Equilibrium is reached when the influx of fluid particles equals the out flux, and corresponds to a balance between the osmotic pressure and the restoring tension of the stretched polymer chains.

Figure 3.3 replaces the mixing of rigid particles with the swelling/mixing of a polymer interacting with surrounding fluid particles:

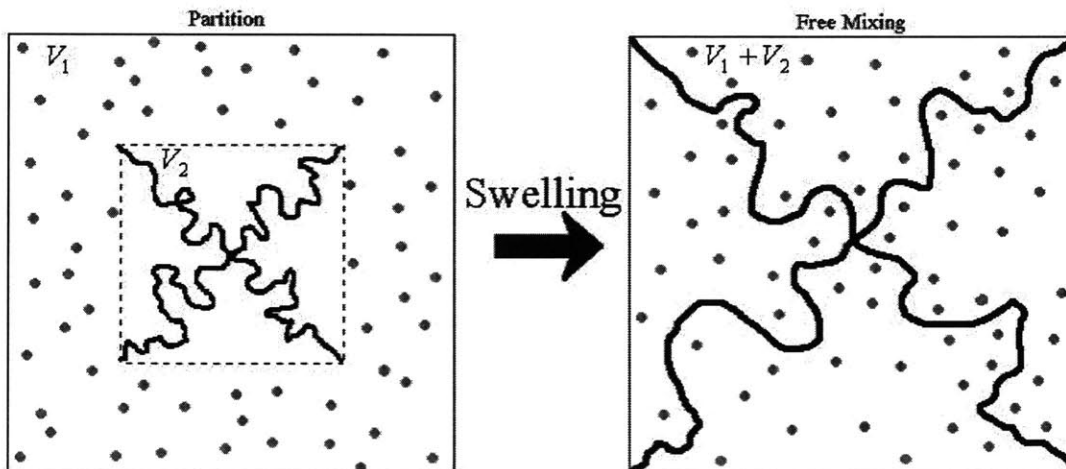


Figure 3.3: Schematic of a polymer separated from fluid particles and then allowed to mix (swell)

The schematic presented in Figure 3.3 is exactly the same case as that presented in Figure 3.1 of an elastomer first swelled by λ_s . The total change in configurational entropy per unswollen volume is determined by substituting the stretch λ_s for the total stretch Λ from (3.1) into (2.34):

$$\Delta S'_s = -\frac{1}{2} N_c k_B (3\lambda_s^2 - 3) \quad (3.7)$$

where the prime on $\Delta S'_s$ indicates the entropy is per unit unswollen volume.

From (3.7), we can calculate the entropy change in the swelled molecular network due to configurational changes in the polymer chains alone, which can be represented equivalently as

$$\Delta S'_s = -\frac{1}{2} N_c k_B (3v_p^{-2/3} - 3) \quad (3.8)$$

The total entropy change is simply the entropy increase due to mixing (3.6) combined with the configurational entropy decrease due to the chain stretching (3.8):

$$\Delta S'_{total} = \Delta S'_s + \Delta S'_M, \quad (3.9)$$

The mixing entropy in (3.9) must be formulated per unit reference volume. As such, (3.6) is first divided by the reference volume V_2 :

$$\Delta S'_M = \frac{-k_B (n_1 \ln v_1 + n_2 \ln v_2)}{V_2} \quad (3.10)$$

Next, note that the volume fraction v_2 is simply the previously introduced volume fraction of polymer v_p , equivalently the inverse of the volume ratio J . The volume fraction of solute, v_1 , can be expressed in this binary system as $1 - v_p$. Additionally, the ratio n_2/V_2 is simply the number of solute sized chain segments (x) times the number of chain molecules per unit reference volume (N_c). The number of solute sized chain segments, x , is just the ratio of the molar volumes of solute and solvent. Therefore, n_2/V_2 is equivalent to xN_c , which must be the same as the concentration of the unmixed solute N_{sol} . Put more simply, if a chain segment is chosen to occupy the same amount of volume as a solute molecule, then there must be the same number of solute molecules per unit volume as there are chain segments per unit volume. The number of solute molecules per reference volume, n_1/V_2 , by algebraic manipulation may be expressed in terms of the concentration of the unmixed solute, N_{sol} , and the volume ratio as $n_1/V_2 = xN_c(J - 1)$. The reduced form for the entropy of mixing per unit unswollen volume is

$$\Delta S'_M = -k_B x N_c \left((J - 1) \ln(1 - v_p) + \ln v_p \right) \quad (3.11)$$

The total change in entropy per unit unswollen (reference) volume is

$$\Delta S'_{total} = -k_B N_c \left(\frac{3}{2} (v_p^{-2/3} - 1) + x \left((J-1) \ln(1-v_p) + \ln v_p \right) \right) \quad (3.12)$$

When the partition in Figure 3.3 is removed and the polymer gel is allowed to swell, it comes to an equilibrium swelled state corresponding to an exact balance between the mixing and configurational entropy changes. The total entropy change given in (3.12) must be zero at the equilibrated state. At this equilibrium, a slight increase in the swelled volume will cause an unfavorable decrease in configurational entropy, while a slight decrease in the swelled volume pays the penalty of the decrease in mixing entropy. Henceforth, the analysis assumes that sufficient time has passed to reach the equilibrium state.

Next, a mechanical stretch is applied to the swelled polymer. The discussion hinges on carefully observing that the entropy change due to mechanical stretching from the swelled state is with respect to the unswelled state. It is given as

$$\Delta S' = \Delta S'_{total} - \Delta S'_s \quad (3.13)$$

The configurational entropy change in the network due to mechanical loading is determined by subtracting the entropy change due to swelling from the total entropy change:

$$\Delta S' = -\frac{1}{2} N k_B \left[\Lambda_1^2 + \Lambda_2^2 + \Lambda_3^2 - 3v_p^{-2/3} \right] \quad (3.14)$$

Using (3.1), we can rewrite (3.11) as

$$\Delta S' = -\frac{1}{2} N k_B \left[\lambda_1^2 v_p^{-2/3} + \lambda_2^2 v_p^{-2/3} + \lambda_3^2 v_p^{-2/3} - 3v_p^{-2/3} \right] \quad (3.15)$$

or

$$\Delta S' = -\frac{1}{2} N k_B v_p^{2/3} \left[\lambda_1^2 + \lambda_2^2 + \lambda_3^2 - 3 \right] \quad (3.16)$$

Once again, the emphasis is that $\Delta S'$ is the entropy change due to mechanical loading with respect to the unswollen state and is per unit unswollen volume.

The entropy change per unit swollen volume, ΔS , is

$$\Delta S = \Delta S' \frac{V_o}{V_s} = \Delta S' v_p. \quad (3.17)$$

Substituting (3.16) into (3.17), and still assuming mechanical incompressibility yields the important result:

$$\Delta S = -\frac{1}{2} N k_B v_p^{1/3} \left[\lambda_1^2 + \lambda_2^2 + \lambda_3^2 - 3 \right] \quad (3.18)$$

3.2.2 Strain-Energy Functions of Swelling Behavior

3.2.2.1 Thermodynamics

Including swelling behavior changes the thermodynamics of the situation only slightly from that formulated in section 2.3.2.1. The strain energy function is determined from the change in entropy using the result from (2.40), however, we must now determine the effect of $p\Delta V$ work that was previously negligible.

For mechanical loadings, the change in volume is so small that $p\Delta V$ is neglected. Referring to Figure 3.1, observe that the swelling causes a small volume element to expand, such that the change in volume is no longer small. The polymer chains within this volume element must also expand, in a more or less affine manner. Thus, the volume change causes tension in the polymer network. But the polymer is macroscopically stress free – it does not try to collapse in on itself. Therefore a force must be balancing the tension in the chains. That force is hydrostatic and is the aforementioned osmotic pressure. During the swelling process, some fluid has diffused via osmosis into the polymer matrix. The osmotic pressure, Π , is the pressure necessary to reverse osmosis and return the polymer to the unswelled state. The osmotic pressure can be determined, for example using the Gaussian model from (2.51), by substituting the pure swelling deformation:

$$\Pi = -N_c k_B \Theta \lambda_s^2 \quad (3.19)$$

This pressure exactly counterbalances the micro-tension in the polymer chains once equilibrium has been reached, as shown in Figure 3.4:

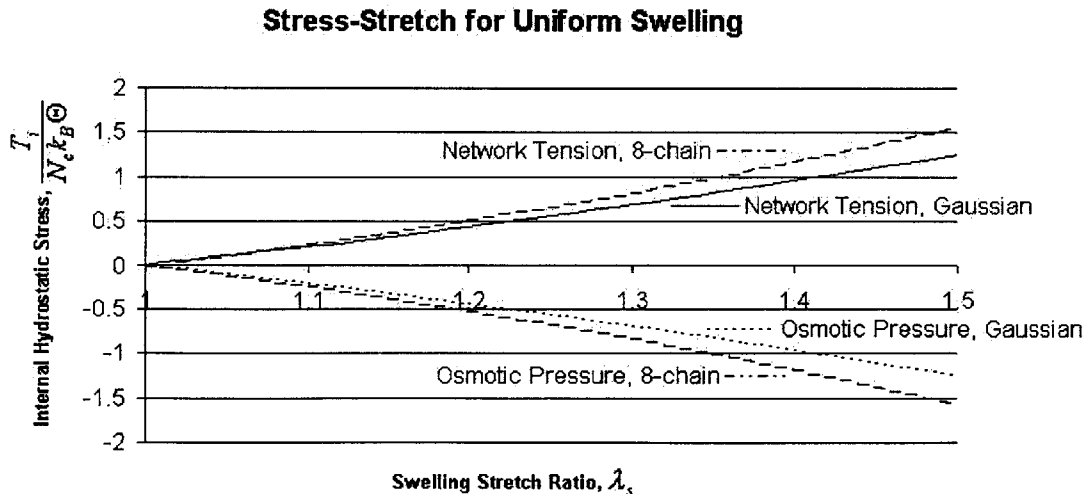


Figure 3.4: The balance of network tension and osmotic pressure in a swelled polymer using the Gaussian model compared to the 8-chain model ($n = 20$).

Thus, we conclude that the $p\Delta V$ term makes no contribution to the strain energy density function due to swelling. The decreased entropy caused by stretching the polymer chains is exactly matched by the increased entropy of mixing.

We can conclude from the above reasoning that the strain energy function per unit swollen volume, assuming mechanical incompressibility is given by

$$U_G = \frac{1}{2} N_c k_B \Theta v_p^{\frac{1}{3}} (\lambda_1^2 + \lambda_2^2 + \lambda_3^2 - 3). \quad (3.20)$$

This corresponds to a strain energy function per unit unswollen volume of

$$U'_G = \frac{1}{2} N_c k_B \Theta v_p^{-\frac{2}{3}} (\lambda_1^2 + \lambda_2^2 + \lambda_3^2 - 3) \quad (3.21)$$

Proceeding along analogous lines, we can write the strain energy function including swelling effects for the 8-chain model per unit swollen volume as

$$U_{sch} = v_p N k_B \Theta \sqrt{n} \left[\beta_{chain} \Lambda_{chain} + \sqrt{n} \ln \left(\frac{\beta_{chain}}{\sinh \beta_{chain}} \right) - \beta_s \lambda_s - \sqrt{n} \ln \left(\frac{\beta_s}{\sinh \beta_s} \right) \right] \quad (3.22)$$

$$\Lambda_{chain} = \left[\frac{1}{3} (\Lambda_1^2 + \Lambda_2^2 + \Lambda_3^2) \right]^{\frac{1}{2}} = \frac{\sqrt{I_1}}{\sqrt{3}} \quad (3.23)$$

$$\beta_{chain} = L^{-1} \left(\frac{\Lambda_{chain}}{\sqrt{n}} \right) \quad (3.24)$$

$$\beta_s = L^{-1} \left[\frac{\lambda_s}{\sqrt{n}} \right] \quad (3.25)$$

Note that λ_{chain} from (2.45) is replaced by Λ_{chain} in (3.22) and (3.24). Refer to [3.5] for a detailed account of this derivation.

3.2.2.2 Stress

The stress developed in the polymer network is a combination of the network tension balancing the osmotic pressure due to swelling, as shown in Figure 3.4, and the response due to the specific mechanical loading.

The Cauchy stress is determined by differentiating the strain-energy function with respect to the total stretch Λ_i . Using the Gaussian strain-energy function (3.2) at a fixed state of swelling, the principal values for the Cauchy stress may be solved for in terms of the principal mechanical stretches relative to the swollen state:

$$T_i = \Lambda_i \frac{\partial U_G}{\partial \Lambda_i} - p^* = Nk_B \Theta v_p^{\frac{1}{3}} \lambda_i^2 - p^* \quad (3.26)$$

It is also useful to express the Cauchy stress in terms of components relative to the dry state:

$$T_i = Nk_B \Theta v_p \Lambda_i^2 - p^* \quad (3.27)$$

The Cauchy stress tensor in terms of stretch relative to the swollen state is

$$\mathbf{T} = 2 \frac{\partial U}{\partial I_1} \mathbf{B} - p^* \mathbf{1} = Nk_B \Theta v_p^{\frac{1}{3}} \mathbf{B}^m - p^* \mathbf{1} \quad (3.28)$$

Likewise, the Cauchy stress tensor in terms of stretch measures relative to the dry state is

$$\mathbf{T} = Nk_B \Theta v_p \mathbf{B} - p^* \mathbf{1} \quad (3.29)$$

It is important to note that the Cauchy stress is the true stress, so (3.28) and (3.29) are equivalent statements. The stresses involved are the same in each case, whereas the deformations are expressed relative to different reference states (\mathbf{B} is with respect to the original configuration, \mathbf{B}^m is with respect to the swollen configuration).

Following a similar procedure, the swelling effects may be incorporated into the 8-chain model for an alternate form of the Cauchy stress by differentiating (3.22), assuming mechanical incompressibility. The principal Cauchy stresses relative to the swollen state are

$$T_i = \frac{Nk_B \Theta v_p^{\frac{2}{3}} \sqrt{n} \lambda_i^2}{3\lambda_{ch}} \beta_{chain} - p^*, \quad (3.30)$$

$$\text{where } \lambda_{ch} = \sqrt{\frac{1}{3}(\lambda_1^2 + \lambda_2^2 + \lambda_3^2)} = \sqrt{\frac{1}{3}(\text{trace}(\mathbf{B}^m))}.$$

The Cauchy stress tensor can be similarly derived and is found to be

$$\mathbf{T} = \left(\frac{Nk_B \Theta v_p^{\frac{2}{3}} \sqrt{n}}{3\lambda_{ch}} \beta_{chain} \right) \mathbf{B}^m - p^* \mathbf{1} \quad (3.31)$$

Relative to the dry state, these stresses are expressed as

$$T_i = \frac{Nk_B \Theta v_p^{\frac{1}{3}} \sqrt{n} \Lambda_i^2}{3\Lambda_{ch}} \beta_{chain} - p^* \quad (3.32)$$

and

$$\mathbf{T} = \left(\frac{Nk_B \Theta v_p^{\frac{1}{3}} \sqrt{n}}{3\Lambda_{ch}} \beta_{chain} \right) \mathbf{B} - p^* \mathbf{1}. \quad (3.33)$$

3.3 Reference

- [3.1] P. J. Flory and J. Rehner Jr., *J. Chem. Phys.* **11**, 512, 1943.
- [3.2] P. J. Flory, Principles of Polymer Chemistry. Ithaca, NY: Cornell University Press, 1953.
- [3.3] L. R. G. Treloar, *Trans. Faraday Soc.* **40**, 59, 1944.
- [3.4] L. R. G. Treloar, The Physics of Rubber Elasticity. New York: Oxford University Press, 1975.
- [3.5] M. C. Boyce and E. M. Arruda, "Swelling and mechanical stretching of elastomeric materials," *Mathematics and Mechanics of Solids*, **6**, 641-659, 2001.
- [3.6] P. J. Flory, Statistical Mechanics of Chain Molecules. New York: Oxford University Press, 1989.

Chapter 4: Examples and Results

The preceding chapters have introduced and reviewed a great deal of material, the utility of which may not be fully appreciated without experimentation, data gathering, and subsequent comparison and analysis. In lieu of physical testing, the following section presents useful results from “thought experiments” gleaned from the most important concepts in the previous chapters, and using the numerical methods outlined above. A comparison to physical data reported in the literature is included near the end of this chapter.

For example, it was stated in Chapter 2 that at moderate to high stretches, the Gaussian statistical model is no longer appropriate and the 8-chain model is offered as a more accurate substitute in the high stretch regime. Examine the difference between the two models at various levels of cross-link density in Figure 4.1:

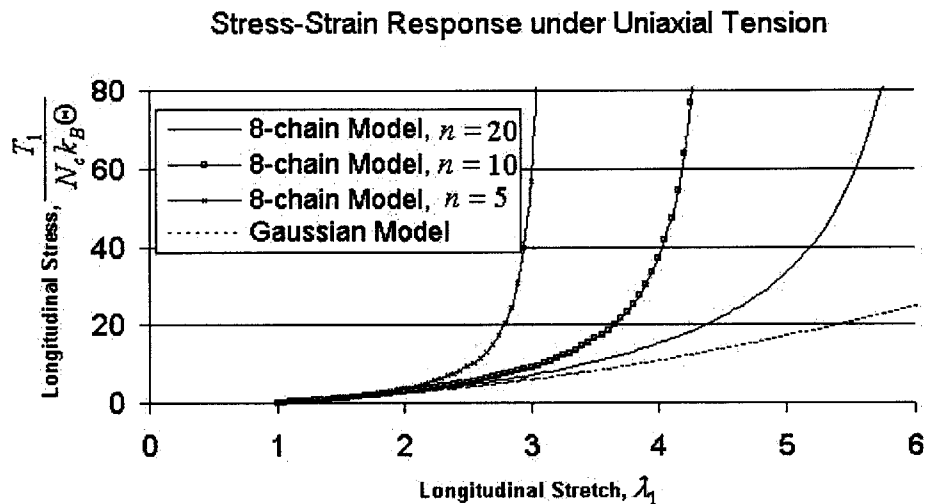


Figure 4.1: Comparison of Gaussian and 8-chain models for simple tension ($n=20$)

Note that in the low stretch regime, the two models are almost coincident. As the applied stretch increases, the 8-chain models with higher cross-link density (a lower value of “ n ”) predict a higher stress due to chain-locking phenomena. Because a lower n indicates the number of chains between cross-links is smaller, the effects of chain locking are observed more dramatically, and always at lower applied stretches. The transitional stretch state where the Gaussian and 8-chain model begin to noticeably diverge corresponds to a chain stretch of about 40% of the limiting extensibility.

Figure 4.1 was developed using a simple spreadsheet and an imaginary bar of some material. The material is initially in the unswelled, undeformed condition. This is the stress-free reference state corresponding to a principal stretch state of $\lambda_1 = \lambda_2 = \lambda_3 = 1$. Then, to simulate uniaxial tension along the first principal stretch

direction, the value of λ_1 is incremented upwards ($\lambda_1 > 1$) with the constraints that 1) $\lambda_2 = \lambda_3$ (uniform contraction in the lateral direction) and 2) $\lambda_1 \lambda_2 \lambda_3 = 1$ (no mechanical volume change).

Now let us examine the same figure, with an additional plot (bold lines) of each model at a moderate swelling state of $\lambda_s = 1.20$:

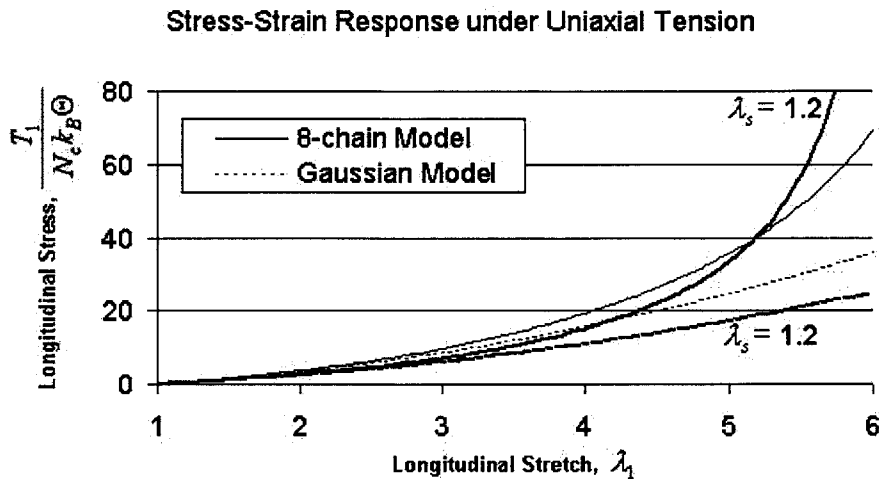


Figure 4.2: Comparison of Gaussian and 8-chain models for simple tension ($n=20$) including swelling effects

While there is once again some ambiguity as to which point the departure between Gaussian behavior and 8-chain behavior becomes important, it is clear that the introduction of swelling has had a significant effect on the higher stretch regime. Because the polymer network is pre-stretched by the swelling action, it reaches the locking stretch more quickly than the unswelled counterpart. This means the departure from Gaussian behavior happens more rapidly at lower stretches and much higher deviations in the models' stress predictions are observed in the moderate to high stretch regime. The higher the swelling ratio, the more pronounced this effect will be.

Throughout this thesis, swelling is often taken to be an independent parameter that the experimenter can assign to some convenient value. In reality, swelling occurs as a result of an entropy imbalance that depends delicately on the solvent and solute characteristics. It is very difficult to properly measure in a controlled environment. Though this paper often takes the swelling ratio to be some constant parameter, it is important to note that it is a dependent variable. The equilibrium swelling value for a Gaussian material can be predicted by plotting the total entropy of mixing and chain stretching from equation (3.12) and finding the point where the total entropy is maximized. For example, Figure 4.3 gives a plot of entropy versus swelling ratio for some arbitrary material exposed to some solute:

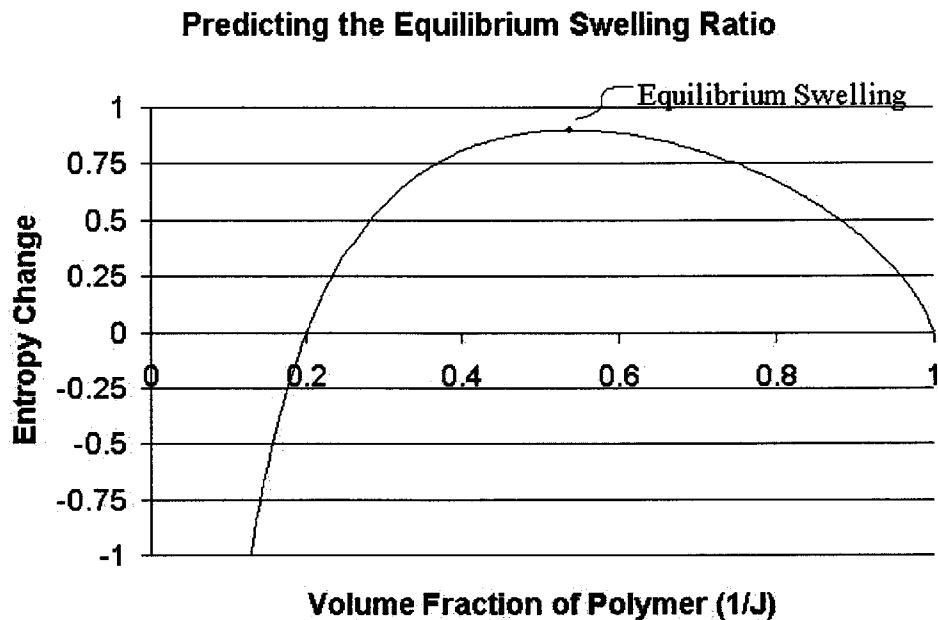


Figure 4.3: The total entropy change at different swelling ratios for a Gaussian polymer/solute.

The curve in Figure 4.3 is traversed by starting at the far right end. The polymer is completely unswelled and has just been immersed in solution. Initially, the entropy of mixing makes it favorable for the polymer to take on more solute and swell (decrease its volume fraction). The polymer chains are well below their limiting extensibilities, and the decrease in entropy from network stretching is no match for the increased entropy of mixing. As we continue to swell the polymer, the network stretching becomes more significant until the point at which the entropy increase from mixing becomes exactly balanced by the decrease in possible arrangements for the network. This is the equilibrium point, often assumed to take on convenient values, but in reality a dependent variable. It occurs where the total entropy is maximized.

Now recall Figure 3.4, which showed the value of the (dimensionless) osmotic pressure at different swelling ratios. This pressure is exactly balanced by the hydrostatic tension, p , in the polymer network, where $p = \frac{1}{3}(T_{11} + T_{22} + T_{33})$. A portion of that tension is attributed to the balance of osmotic pressure, while the remainder is due to the mechanical loading. Figure 4.4 shows the hydrostatic tension due to the osmotic pressure as well as the total hydrostatic tension, p , for uniaxial tension at a fixed swelling ratio of $\lambda_s = 1.20$, as in Figure 4.2. Note that the hydrostatic tension and osmotic pressure are on a different scale (the right axis) from the uniaxial tension (the left axis):

Stress-Strain Response under Uniaxial Tension

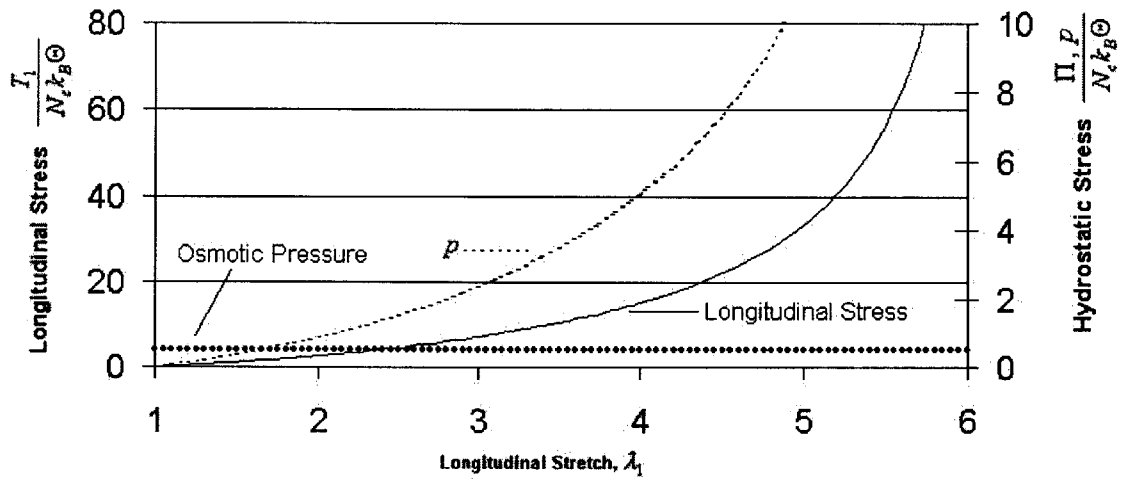


Figure 4.4: Osmotic pressure and total hydrostatic tension (Right Axis) during uniaxial loading (Left Axis).

At a fixed degree of swelling, the osmotic pressure is independent of the deformation, remaining constant throughout. Notice in the unloaded state ($\lambda_1 = \lambda_2 = \lambda_3 = 1$), the network tension exactly balances the osmotic pressure resulting in zero overall hydrostatic stress. As the polymer network is deformed, the macroscopic tension increases and the total hydrostatic tension, p , increases with it. Within the low and moderate stretch regimes, the magnitude of the osmotic pressure is significant compared to the total hydrostatic network tension. But in the high stretch regime, the osmotic term quickly becomes insignificant.

Regardless of the hydrostatic pressure, swelling has a significant effect on material behavior. In general, increased swelling ratios cause a more compliant initial response, but also activate the locking mechanism at lower strains, producing higher stresses in the moderate to large deformation region. Using the 8-chain model, Figure 4.5 shows a typical polymeric material under uniaxial tension at a variety of swelled states. The transition to the locking regime takes place much more quickly in response to higher levels of swelling:

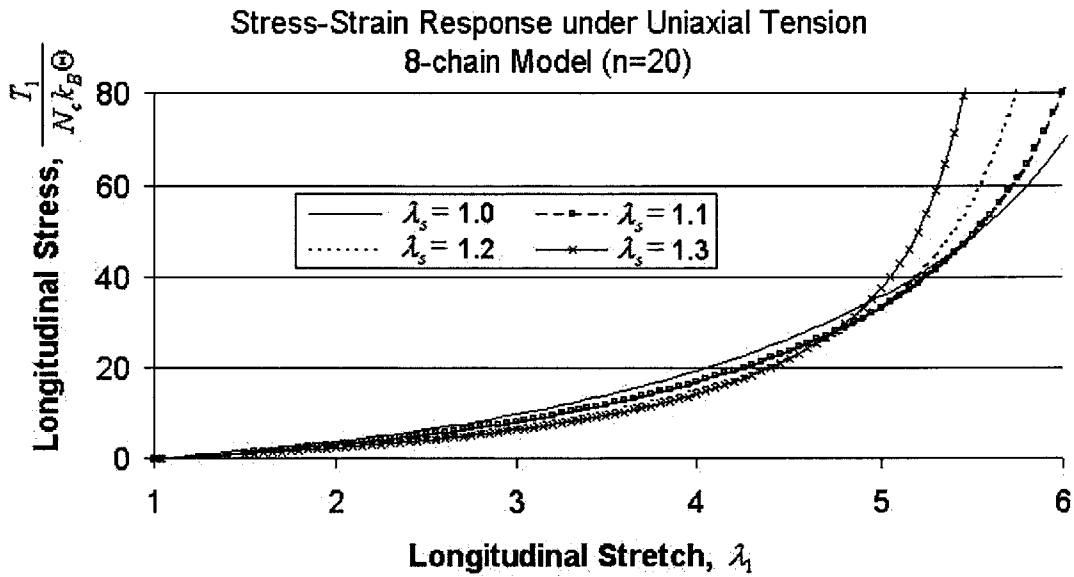


Figure 4.5: Stress-strain response to uniaxial tension and swelling, 8-chain model

The same plot is reproduced in Figure 4.6 using the Gaussian material model. Notice that this material model fails to capture the important effects swelling has on the higher stretch regimes. Once again, the Gaussian model is appropriate at low stretches, and preferred due to its simplicity, but simply a bad predictor at high stretch, especially under swelling action:

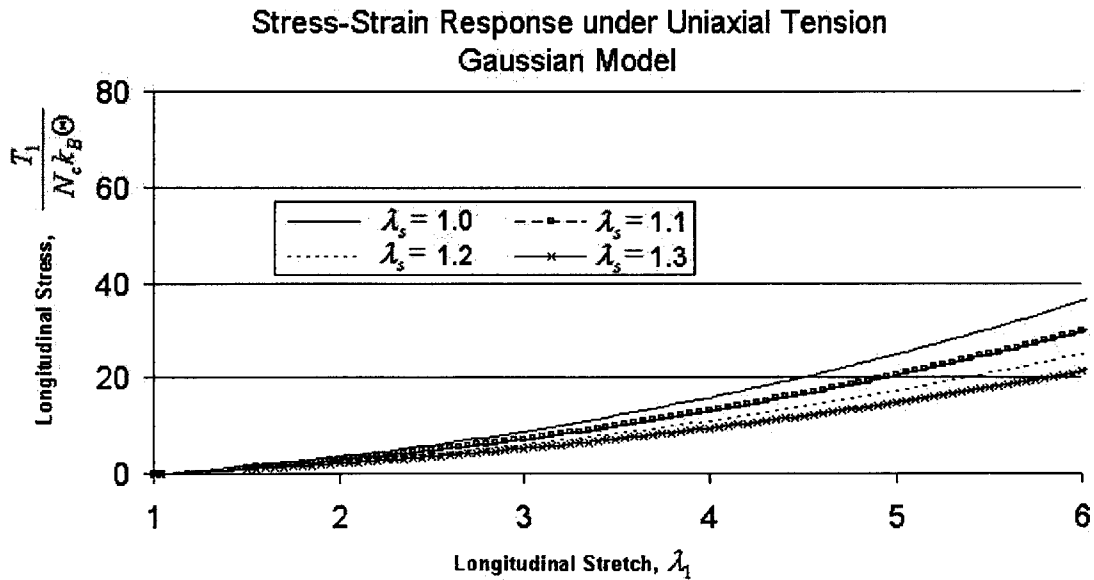


Figure 4.6: Stress-strain response to uniaxial tension and swelling, Gaussian model

Now examine the previous figures in the low stretch regime, where the predictions coincide:

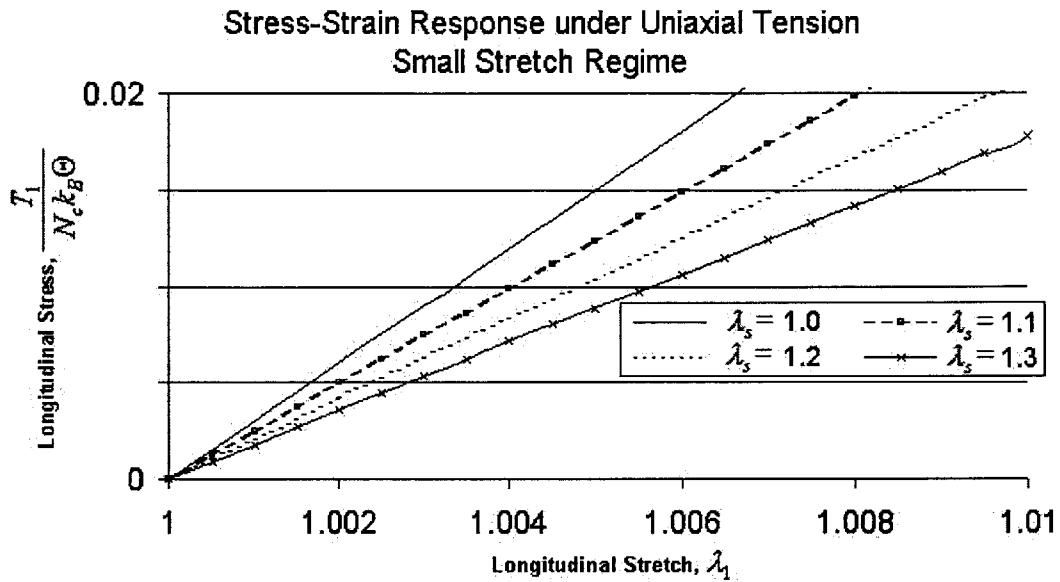


Figure 4.7: Stress-strain response to uniaxial tension, small stretch regime

The difference in initial stiffness between the highly swelled ($\lambda_s = 1.3$) and the unswelled case is about a factor of 2. The familiar example of a sponge, softer when wet (swollen) and more rigid when dry, is apparent in Figure 4.7 and of obvious importance to many applications.

The 8-chain model directly incorporates the cross-link density of the polymer network. As such, the density and degree of long-range interactions between polymer chains can be easily explored by varying the parameter n , the average number of chains between successive cross-links, as in Figure 4.8:

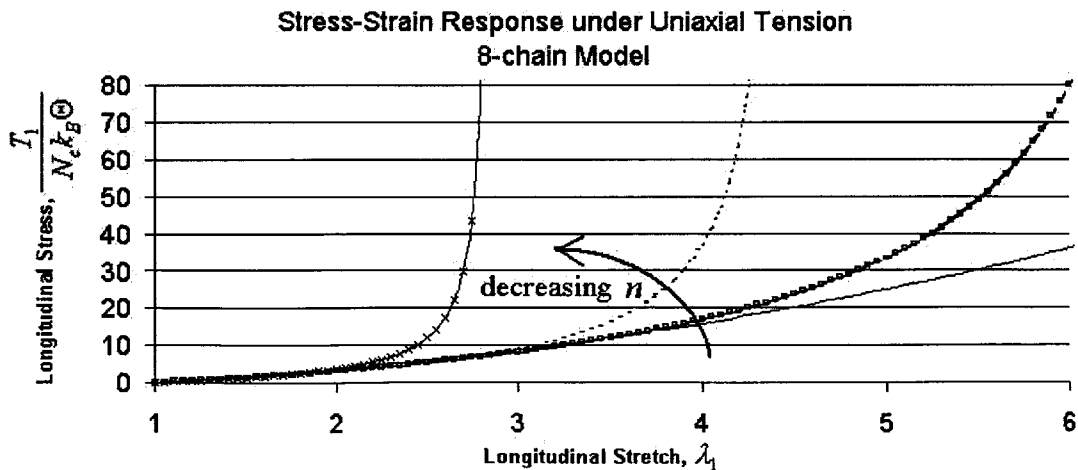


Figure 4.8: Stress-strain response to uniaxial tension, varying cross-link density

The previous plots show uniaxial tension, because it is perhaps the most straightforward test to understand and simplest to model. Other common loadings include uniaxial compression (Figure 4.9) and simple shear (Figure 4.10):

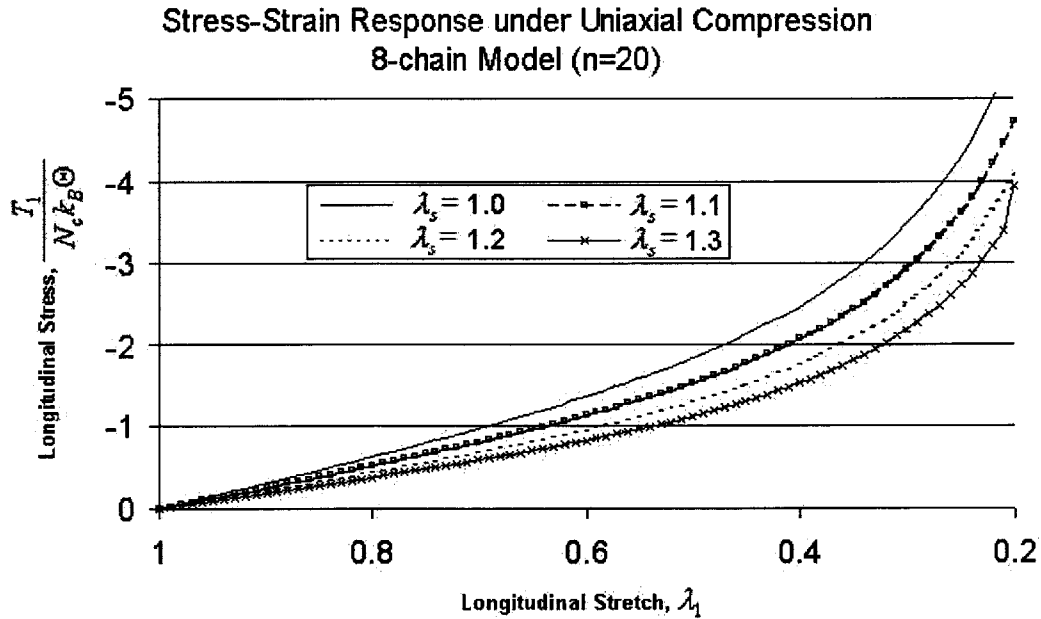


Figure 4.9: Stress-strain response to uniaxial compression with swelling

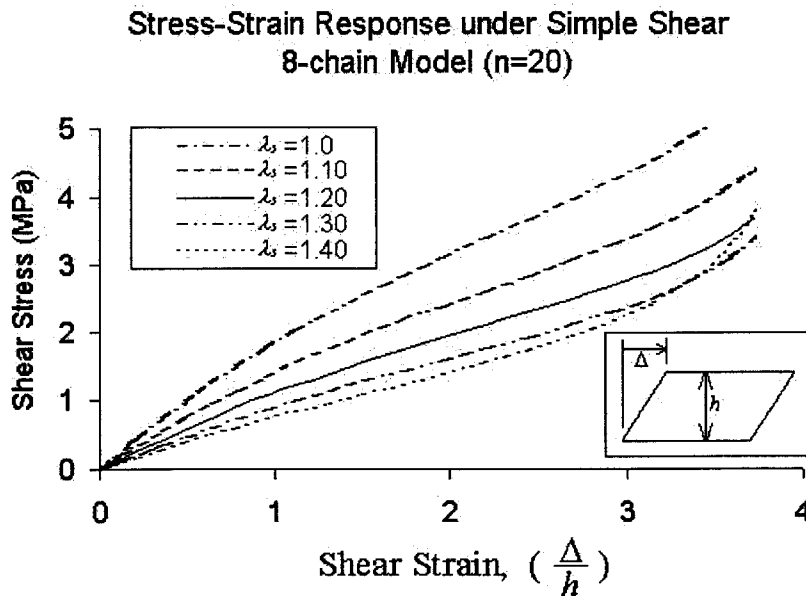


Figure 4.10: Stress-strain response to simple shear with swelling

The same trends hold true under shear and compression loads: the initial response is more compliant and the more swollen materials tend to reach locking stretch (and higher stresses) sooner.

Lastly, it may be instructive to fit the material model developed in Chapter 3 to physical data gathered from a swelled deformation. In a recent study closely related to the subject of this thesis, Marra, Ramesh, and Douglas [4.1] characterized a compliant active material (PVA-PAA). Notably, they present data collected from a polymer gel under uniaxial tension in the unswelled ($\lambda_s = 1.0$) and swelled ($\lambda_s = 1.32$) states, reproduced in Figure 4.11:

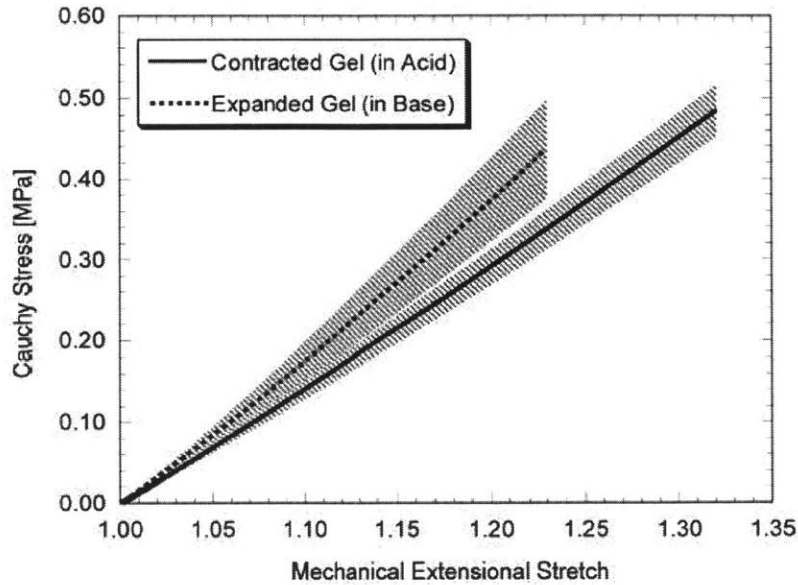


Figure 4.11: Average Cauchy stress versus extensional stretch for contracted and expanded PVA-PAA gel specimens undergoing uniaxial deformation. The shaded regions indicate the uncertainty bounds of each curve [4.1 – Figure 5].

They go on to use Ogden’s model, consisting of six independent variables to predict the following stress-strain behavior:

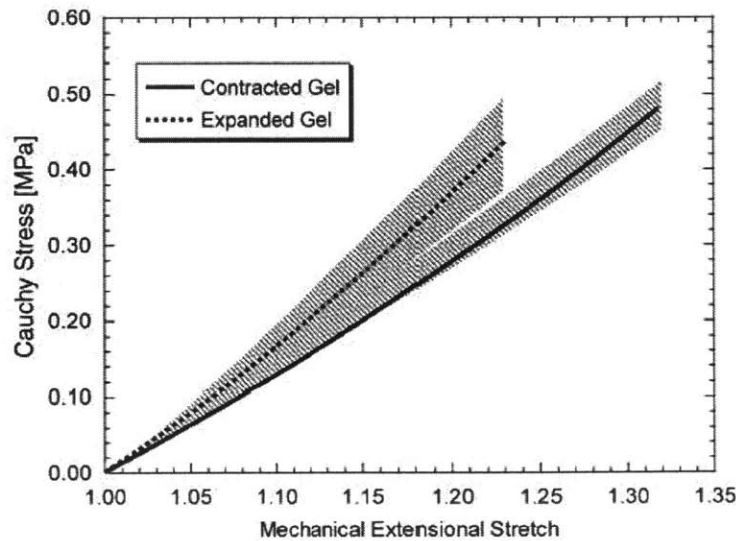


Figure 4.12: Cauchy stress versus extensional stretch for contracted and expanded PVA-PAA gel specimens undergoing uniaxial deformation using an Ogden form of the free-energy function [4.1].

Figure 4.12 was developed using the Ogden form of the free-energy function, along with the fact that the Cauchy stress tensor, \mathbf{T} , is related to the deformation via the free-energy, ψ :

$$\mathbf{T} = \frac{1}{J} \left(2\mathbf{F} \frac{\partial \psi}{\partial \mathbf{C}} \mathbf{F}^T - p\mathbf{I} \right). \quad (4.1)$$

The Ogden form of the free-energy function is derived in [4.1] as

$$\psi = \sum_{i=1}^N \frac{2\mu_i}{b_i^2} (\lambda_1^{b_i} + \lambda_2^{b_i} + \lambda_3^{b_i} - 3). \quad (4.2)$$

The six parameters used to develop the prediction in Figure 4.12 are reproduced in Table 4.1:

| | Fully contracted gel | Fully expanded gel |
|---------|----------------------|--------------------|
| A | 1 | 1.32 |
| N | 2 | 2 |
| μ_1 | 0.90 MPa | 1.8 MPa |
| b_1 | 2.0 | 2.0 |
| μ_2 | -0.51 MPa | -2.5 MPa |
| b_2 | -0.8 | -0.8 |

Table 4.1: Material parameters for Ogden form of the free-energy function for contracted and expanded PVA-PAA gel [4.1 – Table 1].

We may compare the above predictions with the 8-chain model and its three variables ($\lambda_s, Nk_B\Theta, n$). In Figure 4.13, the experimental data from Figure 4.11 has been blotted out and replaced by the 8-chain prediction superimposed for $n = 2.29$ and $Nk_B\Theta = 0.32$ MPa in the unswelled and swelled ($\lambda_s = 1.32$) states:

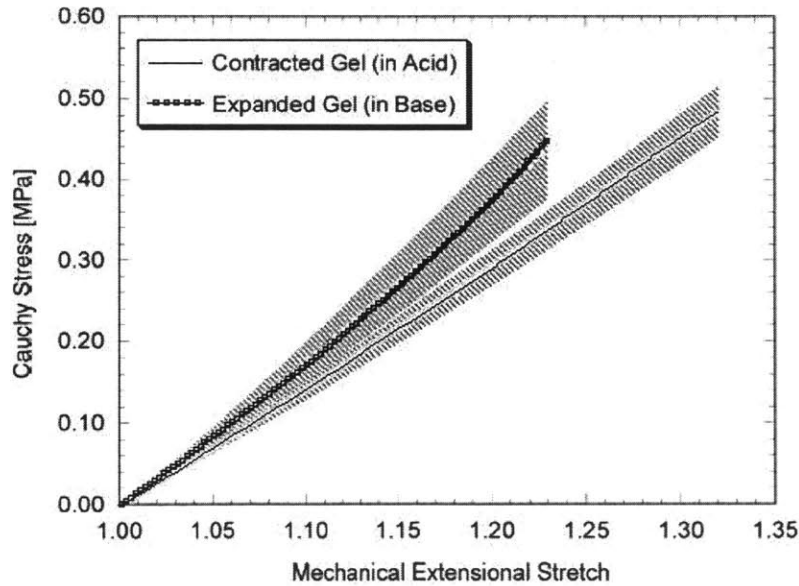


Figure 4.13: Cauchy stress versus extensional stretch for contracted and expanded PVA-PAA gel specimens undergoing uniaxial deformation using the 8-chain Arruda-Boyce form of the strain-energy function.

Besides providing an excellent fit for the data, the 8-chain model uses only 3 parameters, one of which (λ_s) has been specified by the experiment. At the high crosslink density specified, the swelled state is initially more rigid than the unswelled state, and quickly moves towards a locking stretch around $\lambda = 1.4$.

Biaxial experiments are much harder to physically conduct, though simple to predict using a computational model. In [4.1], the authors present biaxial and equibiaxial extension tests in addition to the uniaxial results. Presumably because of the size of the sample specimen and difficulty eliminating clamping effects, the results presented in [4.1] are sample specific (force vs. displacement as opposed to stress vs. strain/stretch). Because no direct comparison can be made with sample specific data, Figure 4.14 depicts the prediction of material behavior using the same parameters from Figure 4.13 for the same material undergoing equibiaxial extension.

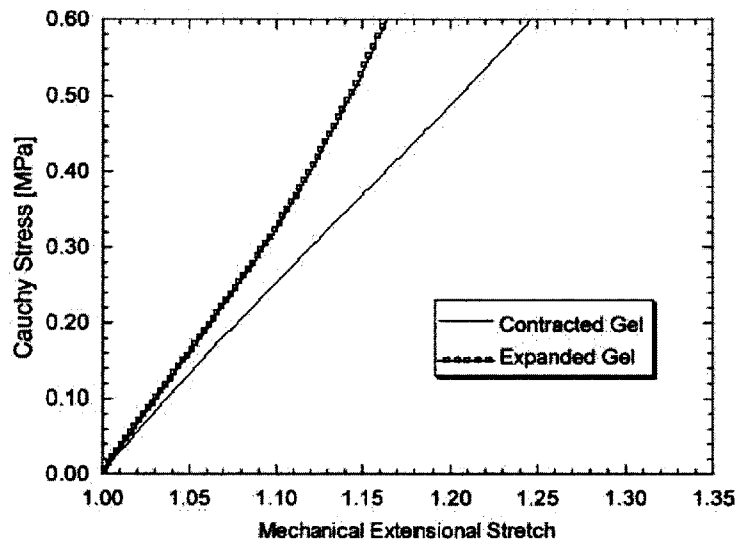


Figure 4.14: Cauchy stress versus extensional stretch for contracted and expanded PVA-PAA gel specimens undergoing equibiaxial deformation ($\lambda_1 = \lambda_2$) using the 8-chain Arruda-Boyce form of the strain-energy function ($n = 2.29$, $Nk_B\Theta = 0.32$ MPa, $\lambda_s = 1.32$).

The purpose of this chapter was to provide the reader with a better feel for the physical effects swelling has on material behavior. By exploring the Gaussian and 8-chain models under various loading conditions, some intuitive insights may easily be confirmed and expanded upon. Most importantly, note that swelling action causes a more compliant initial behavior under many loading types, but also triggers chain locking at lower stretches. These results are more pronounced with higher swelling and higher cross-link density. While this chapter has been an overview of general material behavior under simple loadings, Chapter 5 provides a detailed and rigorous analysis of a specific loading set on a filled material.

Reference

- [4.1] S. P. Marra, K. T. Ramesh, and A. S. Douglas, "Characterization and modeling of compliant active materials," *Journal Mech. Phys. Solids*, **51** (9), pp. 1723-1743, SEP 2003.

Chapter 5: Application: Filled Polymers

5.1 Filler Polymers: Background

Actuating polymers reversibly change shape (swell) and material properties (stiffness) in response to some external stimulus. Changes in pH and electric fields are a common driving force for this actuation. Because of the high tensile strengths attainable in polymer fibers, conducting polymers (e.g. polypyrrole) may respond with forces greater than 200 MPa – exceeding that of mammalian skeletal muscle by up to two orders of magnitude [5.1]! However, these materials often prove ineffectual because the time constant for actuation is on the order of 25 seconds, and so the power delivered is inadequate for most applications. In order to improve the time response, conducting (non-actuating) fillers may be added to the elastomer. Depending on the volume fraction of filler, the speed of actuation in the polymer matrix may improve greatly. However, this benefit is offset by a change in the mechanical properties of the composite as a whole. That is, the introduction of non-swelling particles introduces internal stress and restricts the actuation to volume changes smaller than those in the unfilled matrix. The objective of this section is to determine the magnitude of these stresses and the amount of reduction in swelling as a function of volume fraction of filler particles.

Berriot, et al, has formulated this problem in [5.2], but solves it using linear elasticity, though a nonlinear material model (e.g. Gaussian) and large deformation kinematics are simple and more appropriate for this situation. Thus, we will follow Berriot's lead in structuring the problem, but pursue a closed-form solution from the framework established in the previous section, as well as finite element analysis.

First, we must make some assumptions. The elastomer matrix material is assumed to have the same properties with or without the particle filler. The filler particle is taken to be perfectly rigid. With the assumption that the particle is perfectly bonded to the polymer matrix, the boundary condition at the interface is one of zero displacement. Alternatively, one could specify a de-bonding strength and solve the problem in that context, but this is beyond the scope of the current focus.

Next, imagine a polymer filled with N randomly distributed particles. The particles are small enough that they may be considered points, or very small spheres. In two dimensions, a (zoomed in) cut of the material would be similar to Figure 5.1:

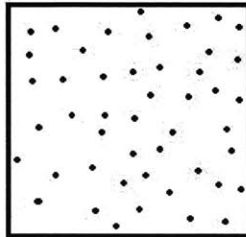


Figure 5.1: A hypothetical material randomly filled with particles

Now if we assign each bit of area in the material matrix to its closest particle neighbor, the matrix is divided into N smaller areas. Figure 5.2 depicts this division, called a Voronoi tessellation, as it applies to the example in Figure 5.1:

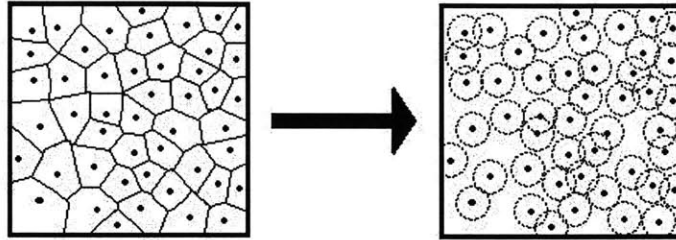


Figure 5.2: A hypothetical material divided into equivalent circular cells.

In two dimensions, the cells begin to take on the rough shape of a circle. Though more difficult to implement, the same procedure may be followed to form roughly spherical cells in three dimensions. When the number of randomly distributed particles is very large, these spherical cells take on a statistically meaningful average size, which is then used to model that material with a representative volume element of a “unit cell” or one particle in a matrix.

5.2 Spherical Shell Model

5.2.1 Kinematics and Boundary Conditions

For the following analysis, we assume a homogeneous distribution of particles throughout the elastomer matrix. Based on the volume fraction of filler, a spherical representative volume element is defined. The spherical cell of initial outer radius B_0 contains a centrally located spherical rigid filler particle of radius A_0 . This element is depicted with the origin centered with respect to the core particle and the polymer matrix shell in Figure 5.3. The matrix has outer radius B_0 in the unswollen state. The unswollen volume fraction of filler material is thus $v_{f_0} = (A_0/B_0)^3$.

The boundary value problem of interest is to determine the effective swelling ratio of the composite with respect to that of the homopolymer and to determine the stress field within the matrix material due to swelling. The problem is solved by conceptually breaking it down into a sequence of loading steps, as depicted in Figure 5.3. Starting with the unswelled composite material in Figure 5.3(a), we swell the polymer matrix assuming no adhesion to the particle to the configuration shown in Figure 5.3(b). Next, the swelled inner radius is radially displaced to coincide with the particle boundary, Figure 5.3(c). This mechanical displacement is assumed to be incompressible, and decoupled from the swelling displacement. The outer radius remains traction free but will be pulled inwards by the kinematical constraint. The last assumption we require is that of symmetry – the displacement (and stress) field is a function of radial location only in this spherical representative element:

$$r = Rf(R) \quad (5.1)$$

For an incompressible material subjected to a radially symmetric deformation, Ogden [5.3] gives the functional relationship $f(R)$ as

$$f(R) = \left(1 + \frac{A_0^3 - A^3}{R^3} \right)^{1/3} = \lambda_\theta, \quad (5.2)$$

where A is the reference inner radius and A_0 is the “deformed” inner radius. If we initially swell the polymer composite (with no adhesion) by $\lambda_s = Q_M^{1/3}$ and define this as the reference state, then $A = aQ_M^{1/3}$, where Q_M is the volumetric swelling ratio of the matrix, the inverse of ν_p . Lastly, we will define Q as the constrained volumetric swelling ratio of the composite. The ratio of Q to Q_M indicates the degree to which the filler particles inhibit swelling, for a given volume fraction ν_{f_0} of particle.

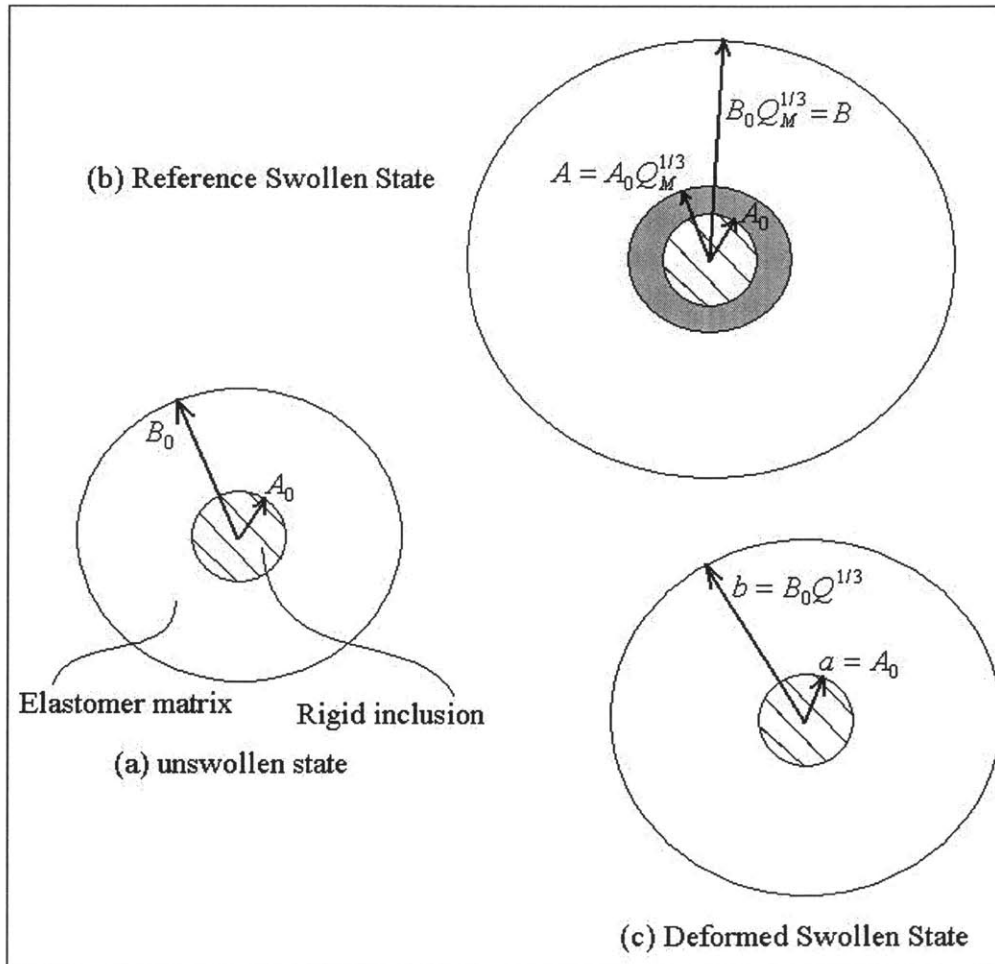


Figure 5.3: Schematic representation of the swelling of (a) a polymer layer surrounding a particle; (b) swelling with no adhesion between the particle and polymer matrix (reference configuration); (c) swelling if there is [perfect] adhesion [5.2].

The principal mechanical stretches corresponding to the spherical polar coordinates r, θ, ϕ are $\lambda_r^{-2}, \lambda_\theta, \lambda_\phi$ respectively, where λ_θ (the hoop stretches) are defined by equation (5.2). Following Ogden, the mechanical hoop stretches at $r = a$ and at $r = b$ are given by

$$\lambda_\theta|_a = 1/Q_M^{1/3} \quad (5.3)$$

$$\lambda_\theta|_b = Q^{1/3}/Q_M^{1/3} \quad (5.4)$$

The polymer matrix of the composite has been assumed to be mechanically compressible. Thus, the constrained volume swelling ratio can be solved for directly from the kinematical constraint. The inner and outer radii are known from Figure 5.3(b) and the inner radius is known in Figure 5.3(c), therefore we can solve for the outer radius in the constrained, swelled state because of the constant volume assumption. The volume in the undeformed, swelled state is equal to the volume in the deformed state:

$$\frac{4}{3}\pi(B_0^3 - A_0^3)Q_M = \frac{4}{3}\pi(B_0^3Q - A_0^3) \quad (5.5)$$

From (5.5), we may solve for the constrained swelling ratio of the composite at a given Q_M :

$$Q = Q_M \left(1 - \frac{A_0^3}{B_0^3} \right) + \frac{A_0^3}{B_0^3} \quad (5.6)$$

After some algebraic manipulation, solving for the ratio of the constrained composite swelling to the unconstrained matrix swelling yields

$$\lambda_b^3 = \frac{Q}{Q_M} = \frac{A_0^3}{B_0^3} \left(\frac{1}{Q_M} - 1 \right) + 1. \quad (5.7)$$

Volumetric Swelling at Different Filler Volume Fractions

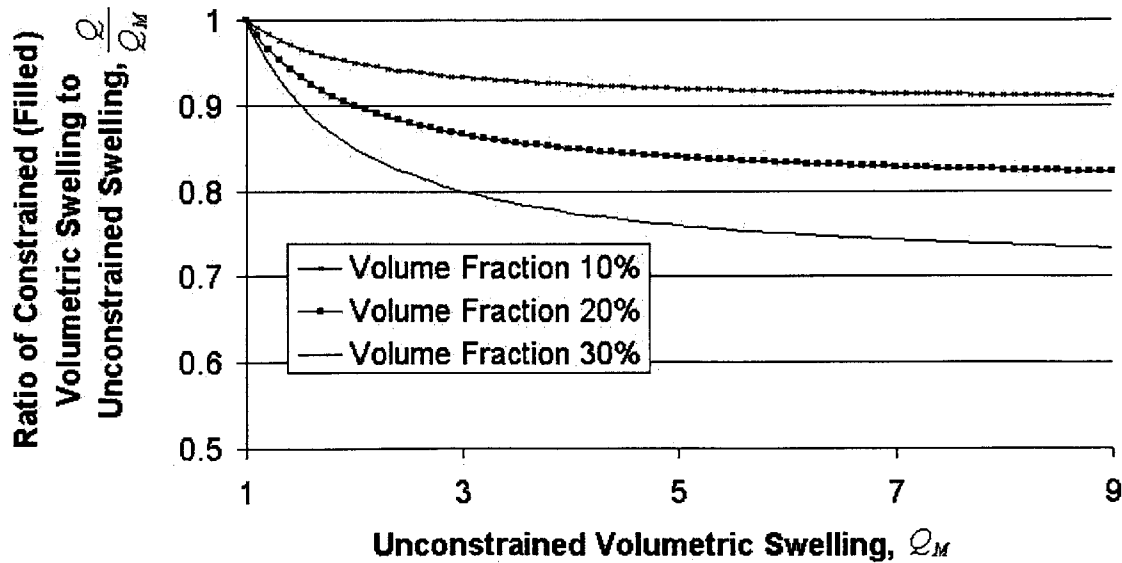


Figure 5.4: Comparison of the reduction in swelling caused by increased filler content

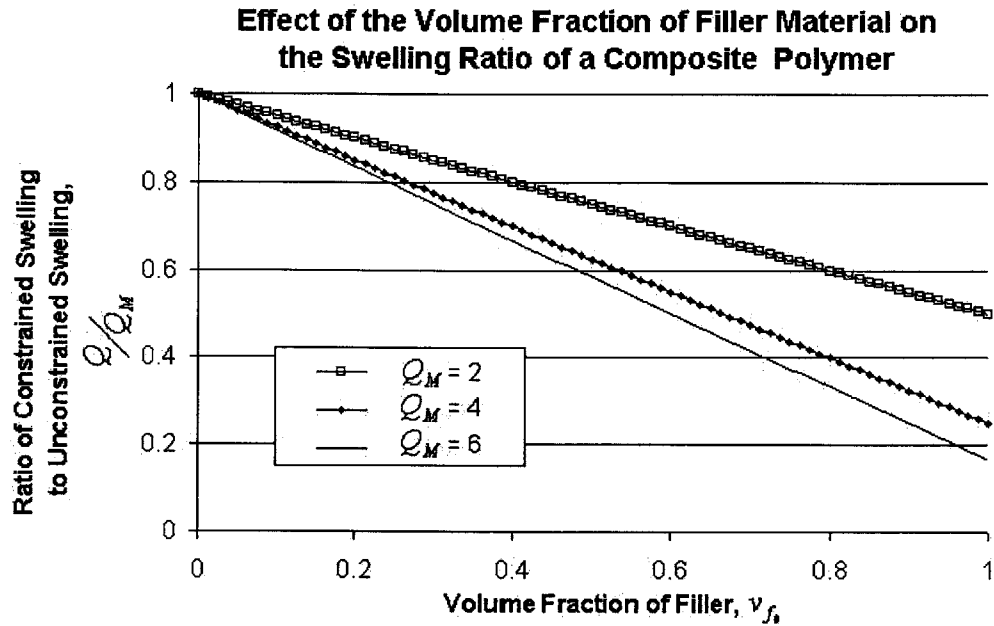


Figure 5.5: The effect of changing filler volume fractions on the equilibrium swelling ratio at a variety of unconstrained volumetric swelling levels.

Figures 5.4 and 5.5 show graphically the reduction in swelling caused by the inclusion of filler particles. The free parameters for this problem formulation are the volume fraction of particle, v_{f_0} , and the degree of swelling indicated by Q_M . Figure 5.4 depicts the variation in Q/Q_M when Q_M is changed for constant values of v_{f_0} . Note that as the volume fraction of filler is increased, the effective swelling of the composite is diminished. Thus, Figure 5.4 verifies that the inclusion of rigid (non-swelling) particles in a deformable (swelling) material will decrease the aggregate swelling of the composite. As we expect, increasing the amount (volume) of rigid particles in the composite detrimentally affects the ability of the material to undergo useful swelling. This effect is more pronounced as we “ask” for higher initial swelling in the form of Q_M .

Figure 5.5 sheds a different light on the situation. At fixed levels of matrix swelling, the volume fraction of filler particles is varied. As expected, an increase in particle content causes a decrease in effective swelling. In the limiting case of 100% filler content, no swelling is possible ($Q = 1$). The validity of our model would be called into question at this point, but in reality filler contents never approach this limit. As always, we must evaluate this analysis with some care, respecting the assumptions of homogeneity and perfect bonding that were at its premise.

5.2.2 Stress Analysis

Simple kinematic considerations go a long way towards understanding the nature of this problem, but a complete solution includes the corresponding stress fields developed in the composite. We start with the derivation of the equilibrium equation ($\text{Div } \mathbf{P} = \mathbf{0}$) in the radial direction, written in terms of the reference configuration as

$$\frac{dt_r^{(1)}}{dR} + \frac{2}{R} (t_r^{(1)} - t_\theta^{(1)}) = 0 \quad (5.8)$$

The Biot stress tensor $\mathbf{T}^{(1)}$ is the symmetric part of $\mathbf{P}^T \mathbf{R}$, where \mathbf{P} is the First Piola-Kirchhoff stress tensor and \mathbf{R} is the rotation tensor [5.3].

For the isotropic material along principal axes, we have

$$t_r^{(1)} = \frac{\partial U}{\partial \lambda_r} - p \lambda_r^{-1}, \text{ and} \quad (5.9)$$

$$t_\theta^{(1)} = \frac{\partial U}{\partial \lambda_\theta} - p \lambda_\theta^{-1}. \quad (5.10)$$

This is evaluated for $\lambda_r = \lambda^{-2}$ and $\lambda_\theta = \lambda$; and from equation (5.2) we obtain

$$R \frac{d\lambda}{dR} = -(\lambda - \lambda^{-2}) \quad (5.11)$$

Now replace the independent variable R by λ in (5.8):

$$\frac{dt_r^{(1)}}{d\lambda} = 2 \frac{(t_r^{(1)} - t_\theta^{(1)})}{\lambda - \lambda^{-2}} \quad (5.12)$$

Next, we apply the boundary conditions. The inside of the shell is effectively subjected to a uniform pressure, P_a . The outside of the shell is traction free.

Or, more succinctly:

$$t_r^{(1)} = \begin{cases} -P_a \lambda_a^2 & | R = A \\ 0 & | R = B \end{cases} \quad (5.13)$$

Let us evaluate (5.12) using the Gaussian model, whose strain energy density function, U_G , is given in equation (3.20). If we note that U may be expressed as $U(\lambda^{-2}, \lambda, \lambda)$ we may apply equation (2.49) to obtain

$$\frac{\partial U(\lambda)}{\partial \lambda} = 2(t_{\theta}^{(1)} - \lambda^{-3} t_r^{(1)}) \quad (5.14)$$

$$= 2Nk_B \Theta Q_M^{-1/3} (-\lambda^{-5} + \lambda). \quad (5.15)$$

Integrating equation (5.12) using the boundary conditions defined in (5.13) will give the pressure per unit current area on the inside radius of the shell. First, rewrite equation (5.12) in the form

$$dt_r^{(1)} = \frac{2(t_r^{(1)} - t_{\theta}^{(1)})}{\lambda(1 - \lambda^{-3})} d\lambda. \quad (5.16)$$

The pressure P_a given in (5.13) is the true pressure at the inner radius. Let us call P_r the negative Cauchy radial stress at any radius, r , and

$$t_r^{(1)} = -P\lambda^2 \quad (5.17)$$

Therefore,

$$dt_r^{(1)} = -P2\lambda d\lambda - \lambda^2 dP, \quad (5.18)$$

or

$$dt_r^{(1)} = -\frac{2t_r^{(1)}}{\lambda} d\lambda - \lambda^2 dP. \quad (5.19)$$

Next, equations (5.9) and (5.10) may be combined by eliminating the variable p and substituting λ for λ_r and λ_{θ} to form

$$\frac{1}{2} \frac{\partial U}{\partial \lambda} = t_{\theta}^{(1)} - \lambda^{-3} t_r^{(1)} \quad (5.20)$$

Solving equation (5.20) for $t_{\theta}^{(1)}$ gives

$$t_{\theta}^{(1)} = \lambda^{-3} t_r^{(1)} + \frac{1}{2} \frac{\partial U}{\partial \lambda} \quad (5.21)$$

Now substitute the results in (5.19) and (5.21) into (5.16):

$$\frac{2t_r^{(1)}}{\lambda} d\lambda - \lambda^2 dP = \frac{2\left(t_r^{(1)} - \lambda^{-3} t_r^{(1)} - \frac{1}{2} \frac{\partial U}{\partial \lambda}\right) d\lambda}{\lambda(1 - \lambda^{-3})} \quad (5.22)$$

With some manipulation, this expression may be rewritten as

$$\frac{\underline{2t_r^{(1)}}}{\underline{\lambda}} d\lambda - \lambda^2 dP = \frac{2t_r^{(1)}}{\lambda} d\lambda - \lambda^2 \frac{\partial U}{\partial \lambda} \left(\frac{1}{\lambda^3 - 1} \right) d\lambda, \quad (5.23)$$

where the underlined terms cancel. We may now perform an integration on the remaining terms in (5.23), after dividing through by the common factor λ^2 :

$$\int_{P_b=0}^{P_a} dP = \int_{\lambda_b}^{\lambda_a} \frac{\partial U}{\partial \lambda} \left(\frac{1}{\lambda^3 - 1} \right) d\lambda \quad (5.24)$$

The integration on the left side is solved using the boundary conditions from (5.13), and the expression simplifies to:

$$P_a = \int_{\lambda_b}^{\lambda_a} \frac{\partial U(\lambda)}{\partial \lambda} \left(\frac{1}{\lambda^3 - 1} \right) d\lambda \quad (5.25)$$

From the kinematic solution in (5.7), we can evaluate this integral for any differentiable strain energy density function. Here the Gaussian model is used for ease of calculation.

With some manipulation, equation (5.25) may be rewritten as

$$P_a = \int_{Q^{1/3}/Q_M^{1/3}}^{\frac{1}{Q_M^{1/3}}} \frac{2Nk_B \Theta Q_M^{-1/3} (-\lambda^{-5} + \lambda) d\lambda}{\lambda^3 - 1} \quad (5.26)$$

Equation (5.26) solves for P_a at a given unconstrained swelling state Q in terms of the parameters ν_{f_0} (in the form of Q_M), N , k_B , and Θ . The explicit solution is:

$$P_a = -2Nk_B \Theta \left[\frac{1}{4} \left(Q_M - \frac{Q_M}{Q^{4/3}} \right) + \left(1 - \frac{1}{Q^{1/3}} \right) \right] \quad (5.27)$$

Equation (5.27) is a useful result, as the true radial stress, P_a , on the inner surface (the interface between polymer and filler particle) is the largest internal stress produced in the composite as a result of the swelling. This is a useful value for studying, among other things, the debonding strength of the particle/matrix system. The result is seen in Figure 5.6 for several particle volume fractions:

Effect of Swelling on the Interfacial Pressure

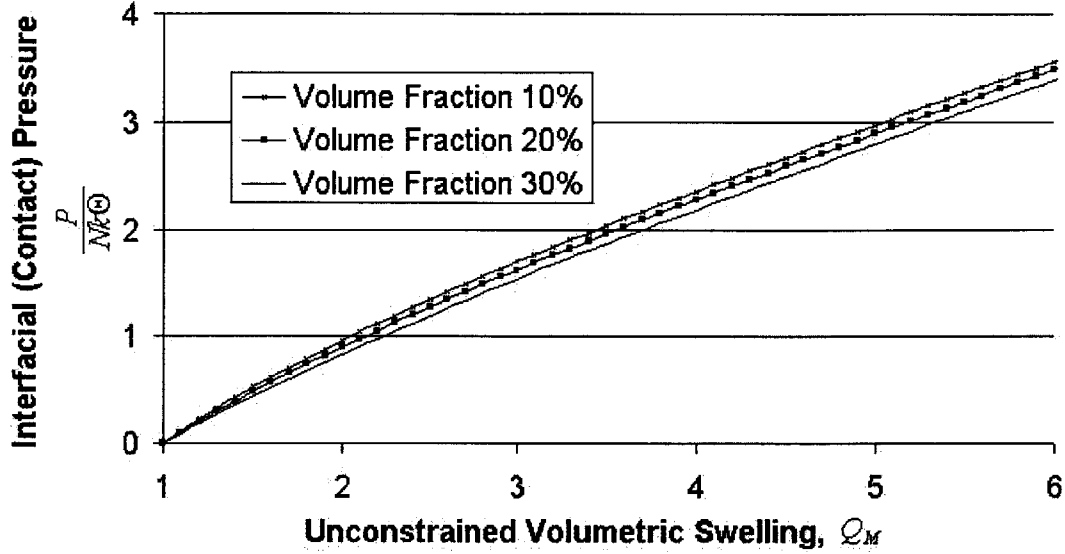


Figure 5.6: The radial interfacial (true) stress as a function of the initial swelling ratio.

The magnitude of the induced stress appears to be fairly insensitive to the volume of filler material, showing a slight decrease as the filler fraction increases. Of course, the stress profiles will deviate from Figure 5.6 for non-spherical particles, as a result of the stress concentrations induced by the more irregular shapes.

Figure 5.6 was developed using (5.13) to calculate the Biot stress, $t_r^{(1)}$, and converting it to the Cauchy (true) stress by

$$T_r = t_r^{(1)} \lambda^{-2}. \quad (5.28)$$

Note that at the interface, $\lambda^{-2} = \lambda_\theta^{-2} = \lambda_r$ is simply $\left(\frac{1}{Q_M^{1/3}}\right)^{-2}$.

The stress profile will now be determined for an arbitrary point in the sphere. The expression for λ at an arbitrary point in the thickness is easily determined from the kinematic solution in (5.7). After some algebraic manipulation, conclude that

$$\lambda_\theta = \lambda = \frac{(Q^{1/3} - 1)(r - A_0 Q_M^{1/3})}{Q_M^{2/3} (B_0 - A_0)} + \frac{1}{Q_M^{1/3}}, \text{ and} \quad (5.29)$$

$$\lambda_r = \lambda^{-2} = \left(\frac{(Q^{1/3} - 1)(r - A_0 Q_M^{1/3})}{Q_M^{2/3} (B_0 - A_0)} + \frac{1}{Q_M^{1/3}} \right)^{-2}, \quad (5.30)$$

where r is the radius in the reference configuration such that $A_0 Q_M^{1/3} \leq r \leq B_0 Q_M^{1/3}$.

Because equation (5.23) is applicable at any point in the sphere, we may change the limits of integration in (5.24) to solve for the Cauchy (true) stress T_r at every point in the thickness via

$$T_r = \lambda^{-2} t_r^{(1)} = \int_{\lambda_0}^{\frac{Q^{1/3}}{Q_M^{1/3}}} \frac{2Nk_B \Theta Q_M^{-1/3} (-\lambda^{-5} + \lambda) d\lambda}{\lambda^3 - 1}, \quad (5.31)$$

Following the same integration procedure as before, the Cauchy stress is solved for explicitly:

$$T_r = 2Nk_B \Theta Q_M^{-1/3} \left[\frac{1}{4} \left(\lambda_\theta^{-4} - \frac{Q_M^{4/3}}{Q^{4/3}} \right) + \left(\lambda_\theta^{-1} - \frac{Q_M^{1/3}}{Q^{1/3}} \right) \right]. \quad (5.32)$$

Using (5.32), (5.14) and (5.15) may be combined to solve for the circumferential tension developed in the sphere,

$$T_\theta = \lambda_\theta^{-1} \lambda_r^{-1} t_\theta^{(1)} = \lambda_\theta^{-1} \lambda_r^{-1} \left(Nk_B \Theta Q_M^{-1/3} (\lambda - \lambda^{-5}) + \lambda^{-1} T_r \right), \quad (5.33)$$

where λ_θ is defined in (5.29).

Figure 5.7 shows the radial and transverse (hoop) stress distributions along the thickness of the sphere at a variety of swelling levels and a fixed volume fraction of filler. Starting with the maximum value in tension at the interface between the particle and matrix materials ($R/A = 1$ in Figure 5.7), the radial stress attenuates to a stress-free state at the outer edge of the matrix material ($R/A = R/B \approx 2.15$ in Figure 5.7). The hoop stress is compressive, once again with a maximum value at the interface and attenuating to a smaller, though non-zero, value at the outer edge. Swelling puts more strain on the system, consequently increased stresses are expected with increased swelling:

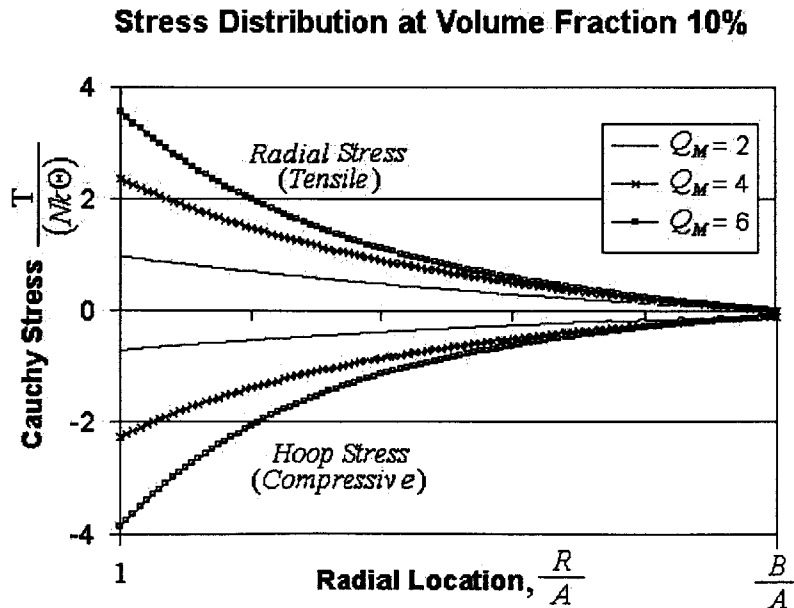


Figure 5.7: Hoop and radial stress distributions at various swelling levels. The inner radius of the matrix sphere is at $R/A = 1$, while the outermost edge is $R/A = B/A$.

Figure 5.8 displays a similar result, although the swelling is fixed and volume fractions are allowed to take a range of values. Perhaps counter-intuitively, increased volume fractions of material attenuate the stress in the system more quickly. This follows from the observation that the increase in available surface area for the matrix material to bind to the filler particles reduces the strain necessary to meet kinematic boundary conditions.

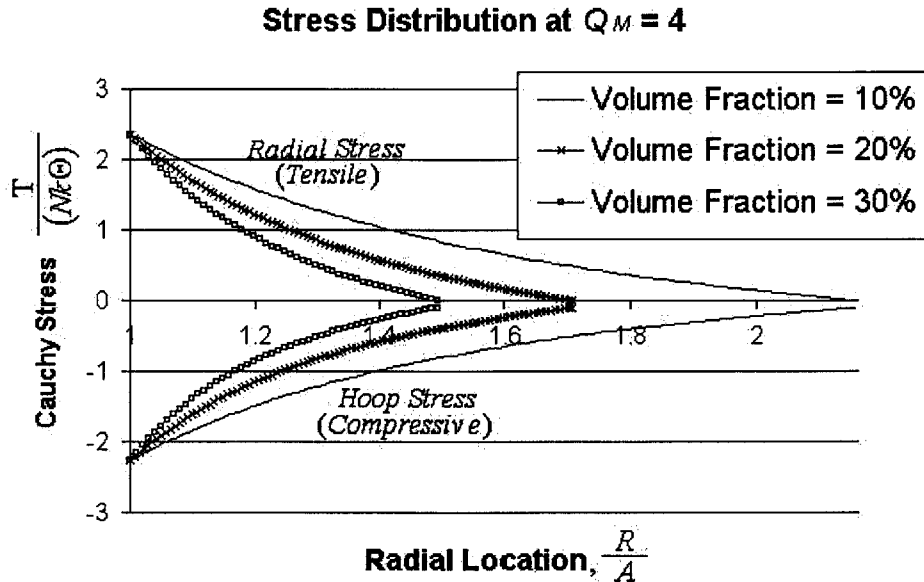
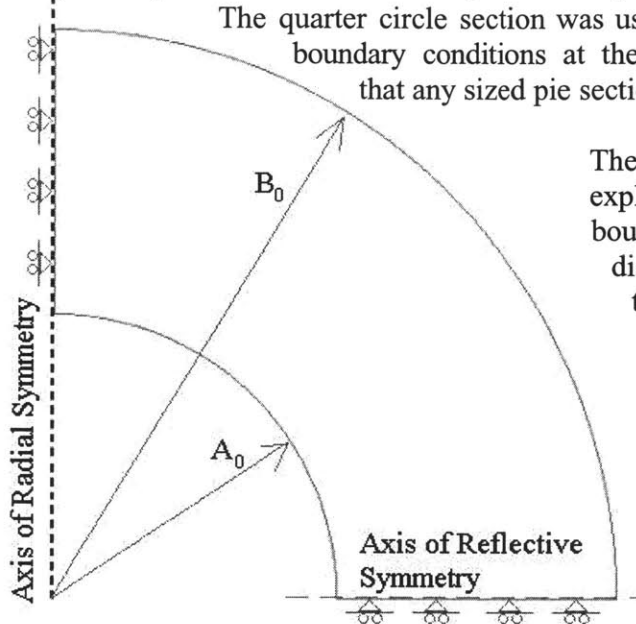


Figure 5.8: Hoop and radial stress distributions at various volume fractions of filler. The inner radius of each matrix sphere is at $R/A = 1$, while the outermost edge is $R/A = B/A$. Because the volume fractions are different, B/A corresponds to a different numerical value in each case.

5.3 Finite Element Analysis/Conclusions

This problem is now easy to implement in a finite element analysis. Using ABAQUS, a commercially available finite element software package, the axial symmetry of the situation was exploited using the geometry shown in Figure 5.9.



The quarter circle section was used because it results in convenient boundary conditions at the axis of reflexive symmetry, note that any sized pie section would be equally valid.

The rigid particle is not included explicitly in the model – it is a boundary condition (of zero displacement) on the inner radius of the shell. The other boundary conditions are a matter of symmetry – there can be no vertical displacement along the downward facing edge, and no horizontal displacement along the radial axis of symmetry. A typical mesh of this geometry might look like that found in Figure 5.10.

Figure 5.9: Axially symmetric geometry in finite element model.

Just as in the analytical case, the material must be modeled. In the finite element procedure this is accomplished by creating a user subroutine for a hyperelastic material (called a *uhyper*, refer to Appendix A). This subroutine gives the partial derivatives of the strain-energy function with respect to the stretch invariants. This is necessary to determine the stress and the stiffness of the material at each increment in the simulation.

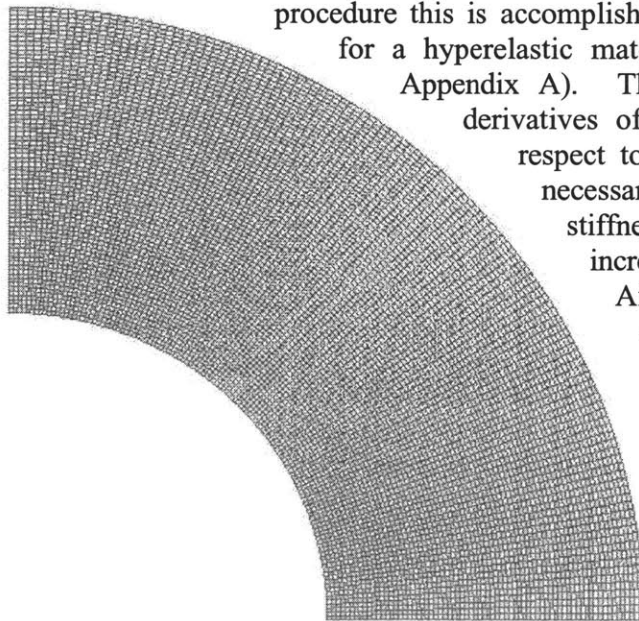


Figure 5.10: A computer generated mesh of the geometry.

After the rigid particle boundary condition of zero displacement along the inner curve is applied, all that remains is to model the swelling. Swelling effects are already included in the rigidity of the material behavior, via the user-defined subroutine. However, swelling changes the size and position of the material

elements, in addition to their stiffness. This problem was overcome by noting the similarity between thermal expansion and swelling of a material. The thermal expansion coefficient was set to $\alpha = 1$, and the initial “temperature” of the assembly was set to $T = 0$. In this manner, the “temperature” T becomes the swelling ratio λ_s (actually, $T + 1 = \lambda_s$). This simple relation is included in the user material definition to model the stiffness correctly, and gives the correct volumetric swell in element size and position.

For example, to reproduce Figure 5.7, one simply has to plot the radial and hoop stresses on a series of nodes ranging from the inner radius to the outer radius of the shell at fixed T corresponding to the desired Q_M . The geometry in Figure 5.11 produces a stress-strain curve at the volume fraction $v_{f_0} = 12.5\%$. Repeating this procedure for different particle sizes produces the array of curves found in Figure 5.7. Figure 5.11 is a snapshot of the maximum principal stress (radial stress) at a swelling level of $\lambda_s = 2$.

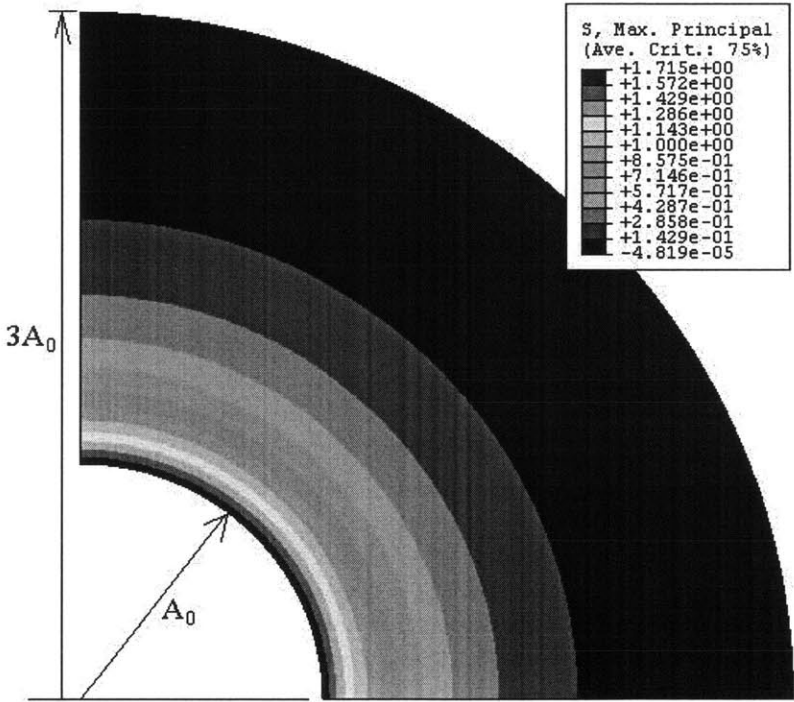


Figure 5.11: An example radial stress distribution.

Figure 5.12 is an example of data from an analytical solution (in this case, the data presented in Figure 5.8) confirmed by computational methods:

Stress Distribution at $Q_M = 4$
 $\nu_{f_0} = 10\%$

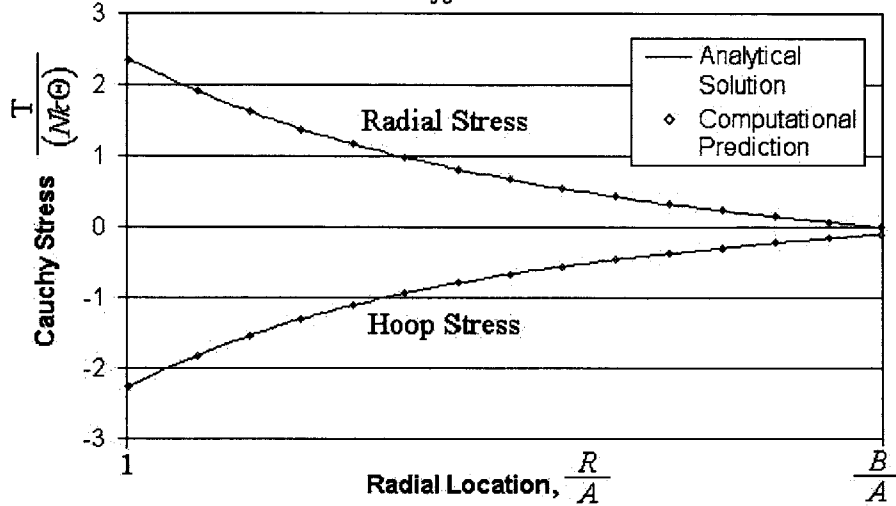


Figure 5.12: Hoop and radial stress distributions – a comparison between the analytical (closed form) solution and the computational (FEA) solution.

The results reported in this chapter were verified using finite element analysis. Computational methods admit the use of any model we choose, even those with no closed form solutions. For example, in the following section we discuss a multiparticle array subjected to swelling/tension. There are no closed form solutions, but the analysis can be performed and compared to the sphere within a sphere that has been elaborated on.

The objective of this chapter was to develop an in depth application of the theory presented in previous chapters. The application brought out the mechanics of the theory, and was the focus of the thesis. So it is reasonable to ask how realistic the solution to the problem is, as given in graphical form in Figures 5.4 through 5.8 and more or less summarized by equations (5.32) and (5.33).

Let us briefly revisit some of our assumptions, and address the validity of, and possible adjustments to, each in turn. First, we should ask if the spherical symmetry of the problem is really appropriate, and what effect would a change in the shape of the representative volume element have?

The answer to this query is straightforward and intuitive. No, the particles are not perfect spheres. Nor will they be, in general, randomly distributed throughout the matrix, and so the surrounding shell is not spherical. Some particles, like carbon black, tend to agglomerate. Also, the particles, even if spherical will have an average size but substantial variation in individual size. This will affect the final analysis. Perhaps more interestingly though, we should note that a spherical particle is probably the worst shape imaginable from a practical standpoint. Increases in the volume of rigid particles decrease the effective actuation of the composite. The purpose of the particles is to connect through the matrix to increase

the conductivity. Spheres take up the most space per surface area, and so are the worst connecting elements we could choose. A series of (oriented) long, slender cylinders would have better conductivity and less inhibition on swelling than their spherical counterparts. In a sense, perhaps the solution described by equation (5.7) is a lower bound to the reduction in swelling – since no shape could be “worse” than a sphere. However, reaching an analytical solution with a complex volume element has only a very remote chance at success. This is where finite element analysis is most useful.

The only other assumption that has real relevance in this context was the one tacitly made in equation (5.15). We assumed the material could be accurately described by the Gaussian (incompressible) constitutive model. This assumption becomes inappropriate as the individual polymer chains begin to feel the effects of their limiting extensibilities. So for higher swelling ratios, the Gaussian model is less likely to be accurate. This would become even more problematic if a mechanical loading was subsequently applied, as the chains would already have some extension. In practice, we have only to replace the strain energy density function, U , in equation (5.25) with whichever strain energy model is more appropriate, including models that allow for compressibility. The 8-chain model was described as a suitable alternative. Proceeding along the same lines will lead to better (if the chosen model is better) solutions, albeit often in a more cumbersome manner.

Lastly, we assumed that the properties of the polymer matrix were uniform and independent of the inclusion. Recall that the first step in developing the swelling theory was decoupling the stretch into mechanical and swelling components. In reality, these components may not necessarily be decoupled. Application of stress may change the swelling ratio. In this case, the inclusions produce a non-uniform stress profile in the composite. This would naturally lead to non-uniform swelling in the composite (which would change the stress distribution and so on). The tools to deal with this coupled problem are available, but beyond the scope of this chapter. Suffice it to say, at the very least, this formulation presents a first approximation to the solution of the problem.

A variety of avenues can be pursued to test the validity of the approximation in the model. These include physical testing, computational modeling, and comparison with results available in the literature. For thoroughness, all three methods should be pursued, probably in the reverse order to that given.

5.4 The Multiparticle Representative Volume Element

Danielsson [5.4] developed a multiparticle mesh generator that goes a step beyond the single particle meshes found in Figure 5.9 – 5.11. This generator creates a 3-dimensional mesh with randomly distributed (non-intersecting) spherical particles at a given volume fraction and diameter:

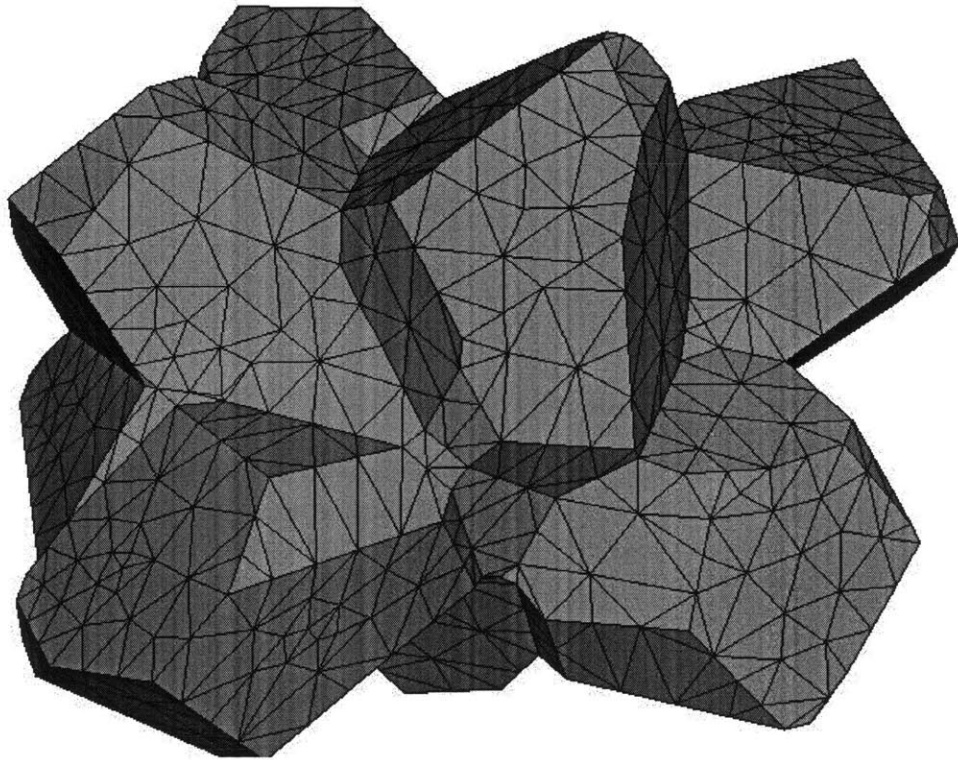


Figure 5.13: A randomly distributed multiparticle mesh ($v_{f_0} = 10\%$).

In Figure 5.14, a translucent representation of the above figure gives a clearer view of the spherical particles from the same vantage point. The boundaries of the assembly are created and constrained such that they produce a repeatable unit cell that can be perfectly surrounded by identical cells. This procedure in effect models a cutaway of a small piece of randomly filled material within a larger continuum. It is a perfect 3-dimensional analogy to the 2-d Voronoi tessellation in Figure 5.2.

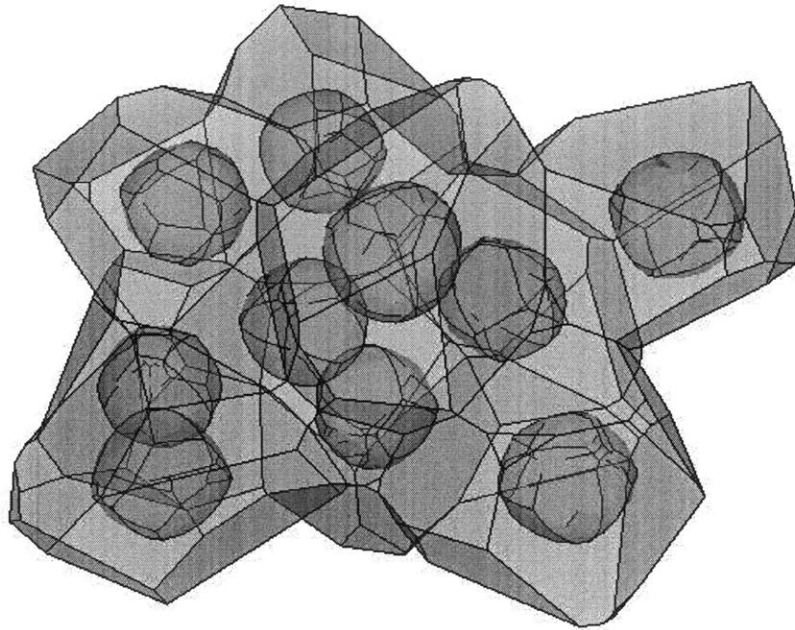


Figure 5.14: A translucent display of the multiparticle mesh ($v_{f_0} = 10\%$).

The multiparticle generator is useful for a variety of reasons. First, it reminds us of the validity of one of the basic assumptions in the analysis of the spherical cell that formed the core of this chapter, namely, that the situation could be modeled as a sphere within a sphere. It takes little imagination to see that the multi-sided shapes surrounding each particle begin to approximate a sphere:

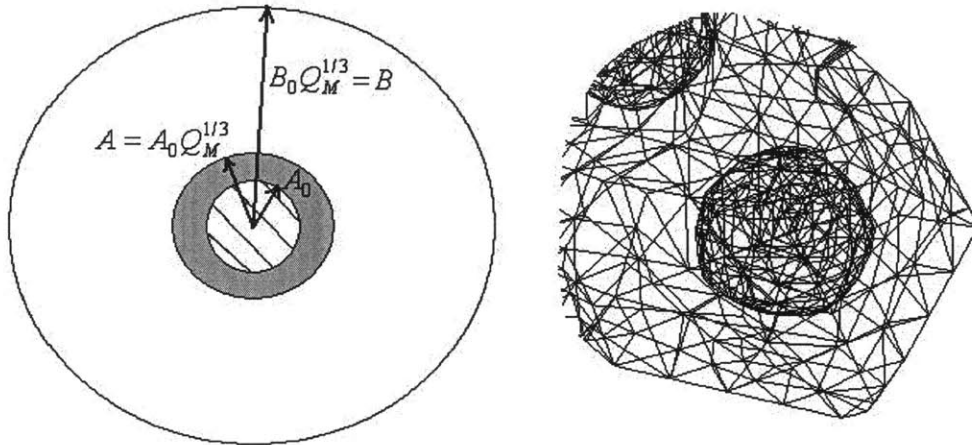


Figure 5.15: A spherical cell compared to Voronoi tessellation. Cutting away the front face of the swollen multiparticle matrix gives more insight into the stress state within the material. Figure 5.16 shows a cut in the plane of the page through the center of the particle mesh prior to deformation. The same cut is shown in Figure 5.17, after swelling has produced stress in the composite:

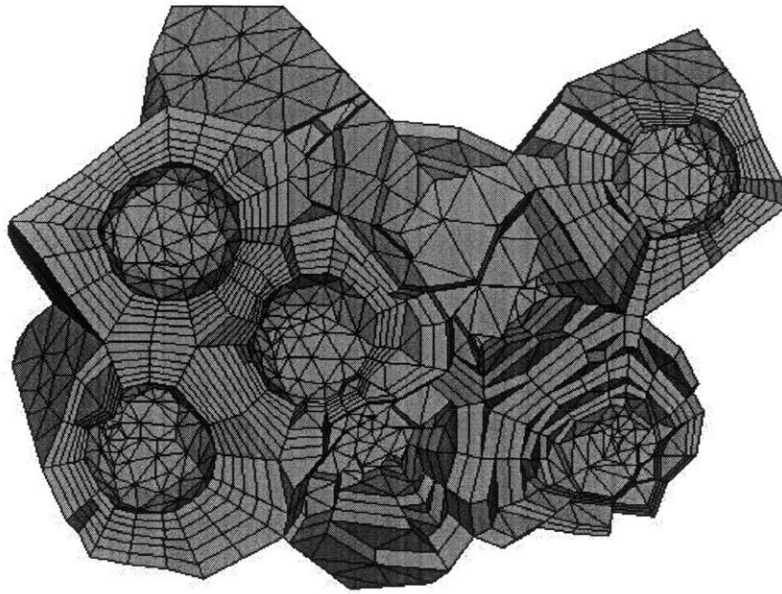


Figure 5.16: A cutaway view of the multiparticle mesh given in Figure 5.13 ($\nu_{f_0} = 10\%$).

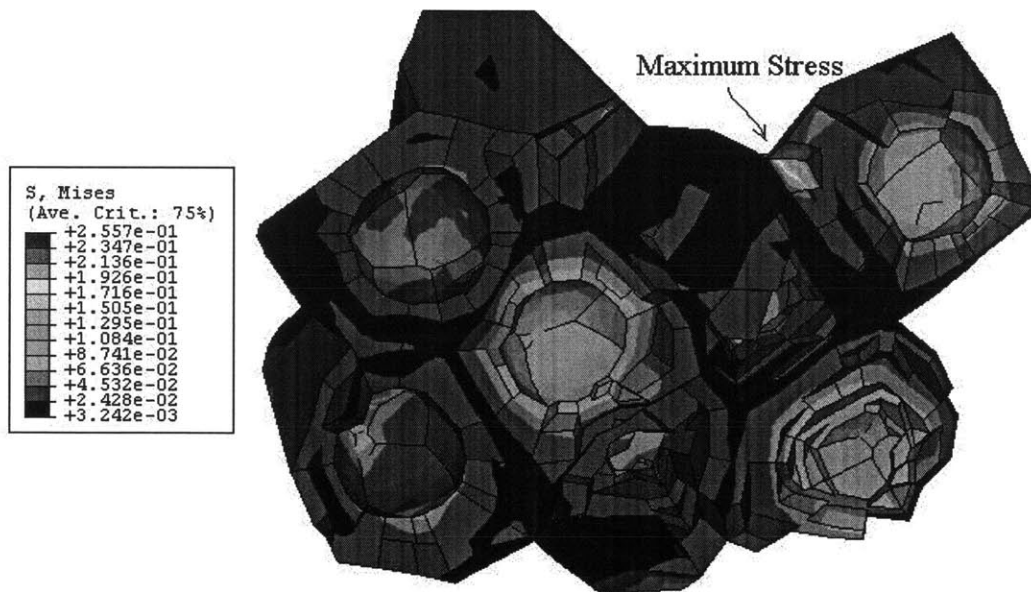


Figure 5.17: A cutaway view of the swelled multiparticle assembly with Von Mises stress ($\nu_{f_0} = 10\%$).

Examining Figure 5.17 more closely reveals some interesting trends. First, notice the stress concentration associated with the proximity of a material point to a particle. Clearly the expected trend of high stresses on the particle surfaces, dissipating outwards, is observed in this simulation. However, perhaps unexpectedly, the maximum stress in this assembly occurs not at the composite interface, but at the boundary between two adjoining particles. This is because in

our prior work, the single cell RVE has no material surrounding the outer radius, and so is traction free. In reality, this material is constrained by surrounding material, which is in turn acted upon by surrounding particles. If several particles are close together, they could create high stresses at the material elements delineating their boundaries, a phenomena not observed in the single particle simulations.

The multiparticle generator also proves useful in validating and reproducing other experiments on the single spherical cell. For example, testing could be expanded to include a loading after the swelling step, where multiple particles randomly arranged are a much better indicator of aggregate material response. The flow of stress around the unaligned rigid particles would certainly be more realistic than the stress fields observed around a single centralized particle cell.

Figure 5.18 shows the stress-strain graph for the multiparticle array deformed under uniaxial tension compared to the stress-strain characteristics for a simple bar of polymer in uniaxial tension with no swelling and with $\lambda_s = 1.2$. The filler particles increase the stiffness of the composite by approximately 40% for both the swelled and unswelled cases:

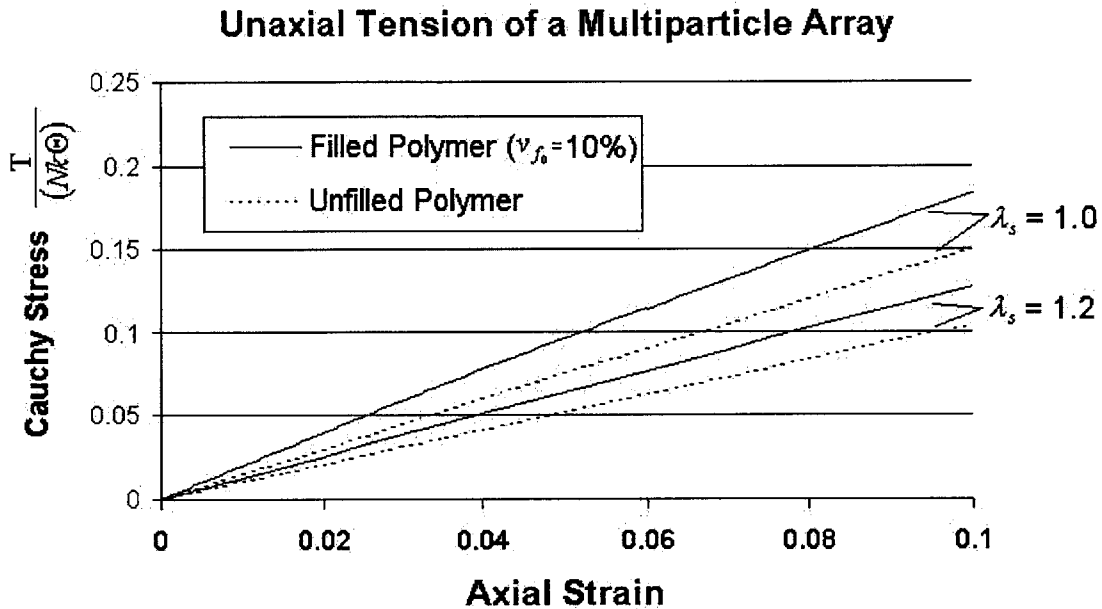


Figure 5.18: Comparison of stress-strain characteristics for the filled (multiparticle array) and unfilled polymer using the Gaussian model at two swelling levels.

5.5 The Cylindrical Representative Volume Element

Another modeling option is to use a cylindrical rigid particle embedded in a cylindrical matrix. Similar to the spherical representative volume element, the cylindrical tube can be freely swelled with no stress to a reference state, and then kinematically constrained to the rigid particle (the deformed state). The circular cylindrical tube has a reference geometry described by $A \leq R \leq B$, $0 \leq \vartheta \leq 2\pi$, and $0 \leq Z \leq L$; where R , ϑ , Z are the cylindrical polar coordinates and A and B denote the inner and outer radius of the swelled (unconstrained) cylinder of matrix material, as in Figure 5.19:

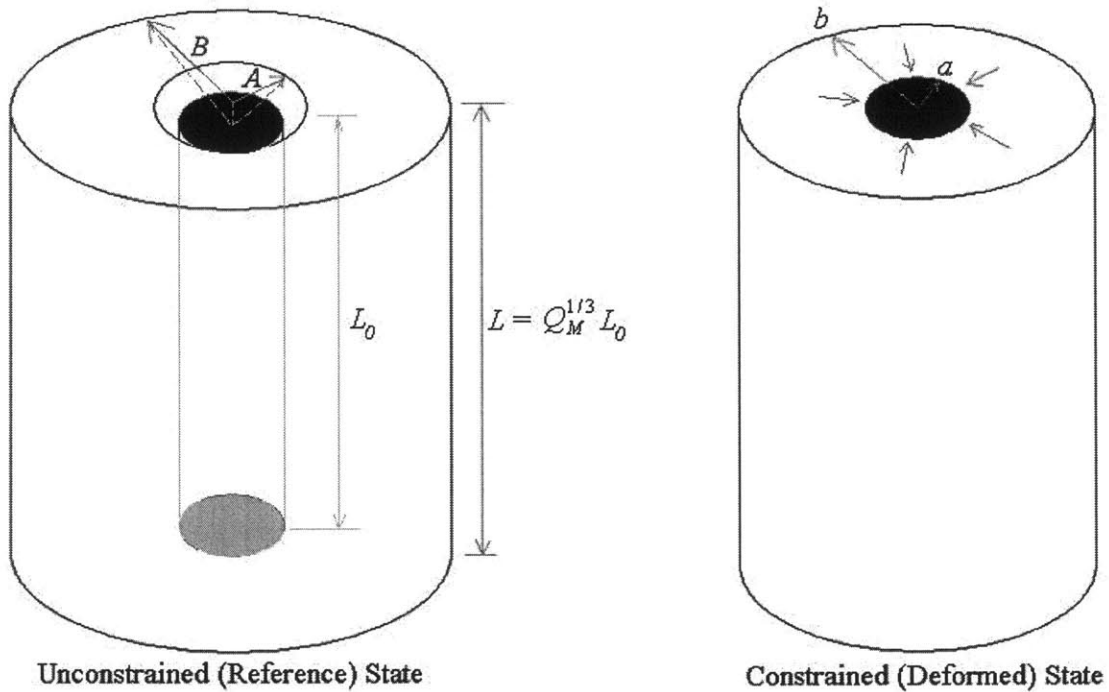


Figure 5.19: A circular cylinder with embedded cylindrical particle.

In this example, we assume that the particle is very long, and therefore the resulting stress profile is independent of the Z -position. Because the material is allowed to freely swell and then is pulled back to the cylindrical particle, $\lambda_z = 1/Q_M^{1/3}$ uniformly throughout the material, where Q_M is the volumetric swelling ratio of the matrix previously defined. Using the swelled reference state, we can compute the resulting stress distribution as a function of the radial position. The material is deformed symmetrically such that the current position (r, θ) of a material point is given by

$$r = (R)f(R), \quad \theta = \vartheta, \quad (5.34)$$

where $a \leq r \leq b$.

Similar to the spherical particle embedded within a spherical shell, the boundary conditions for this problem (i.e. the values of a and b) are easily computed from the requirement of mechanical incompressibility.

Mechanical incompressibility specifies that the volume of the cylinder in the reference state must be equal to that of the cylinder in the deformed state:

$$L(B^2 - A^2) = L_0(b^2 - a^2), \quad (5.35)$$

and note

$$L = Q_M^{1/3} L_0 \quad (5.36)$$

As before the dimensions of A and a are directly linked by the initial swelling ratio Q_M , and B and b are linked by the final swelling ratio in the radial direction Q :

$$A = Q_M^{1/3} a, \quad B = \frac{Q_M^{1/3}}{Q^{1/3}} b, \quad (5.37)$$

where Q is yet to be determined. The final swelling stretch $Q^{1/3}$ is actually the swelling stretch in only the radial ($Q_{radial}^{1/3}$) and hoop ($Q_{hoop}^{1/3}$) directions for the deformed configuration, since in the deformed state the axial swelling stretch is constrained to be $Q_{axial}^{1/3} = 1$.

Therefore, due to the anisotropy, the effective composite swelling ratio defined in (5.38) is a more meaningful variable for comparison between the unconstrained swelled state and the constrained swelled state:

$$Q_{eff} \equiv Q_{radial}^{1/3} Q_{hoop}^{1/3} Q_{axial}^{1/3} = Q^{2/3} \quad (5.38)$$

The kinematic conditions give

$$a = \frac{A}{Q_M^{1/3}} \left(= \frac{A}{\lambda_s} \right), \quad (5.39)$$

and

$$b = A Q_M^{-1/3} \sqrt{\frac{(1 - Q_M)}{(1 - Q_M Q^{-2/3})}} \quad (5.40)$$

Since a is simply the radius of the rigid cylindrical particle, we can express the boundary conditions more simply in terms of the volume fraction of filler particle, prior to swelling:

$$a = \frac{A}{Q_M^{1/3}} \quad (5.41)$$

$$b = A \sqrt{Q_M^{1/3} \left(\frac{1}{v_{f_0}} - 1 + Q_M^{-1} \right)}, \quad (5.42)$$

where v_{f_0} is the volume fraction of filler material $v_{f_0} = \frac{a^2 Q_M^{2/3}}{B^2}$.

The ratio of the effective constrained swelling to the unconstrained swelling for the cylindrical shell representative volume element is given in Figure 5.20 for several volume fractions over a range of unconstrained swelling values:

Volumetric Swelling at Different Filler Volume Fractions

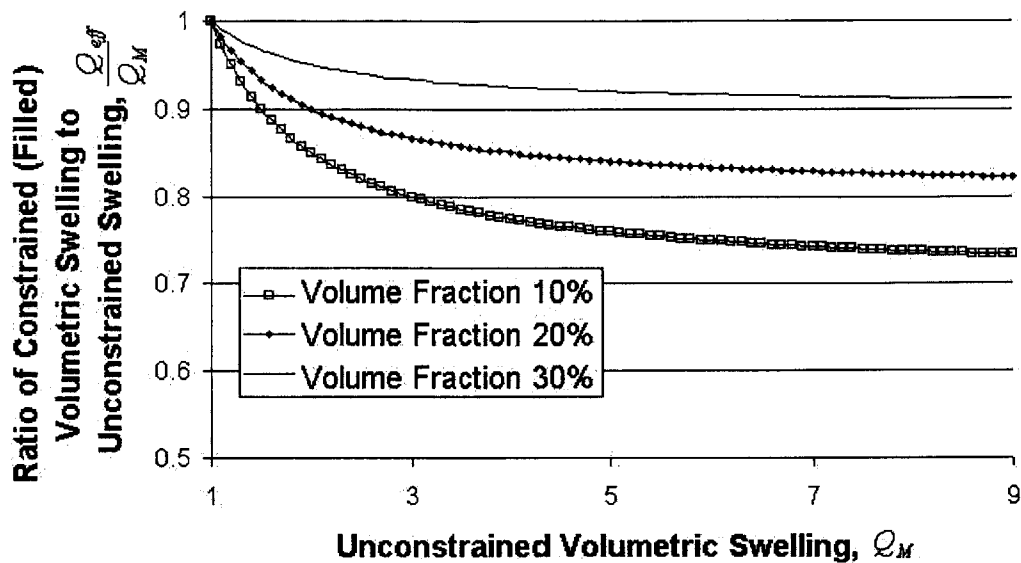


Figure 5.20: The reduction in effective composite swelling caused by increased filler content

As expected, the results obtained from the above derivation, noting the definition in (5.38), exactly correspond with those for the same volume fractions presented in Figure 5.4 for the spherical shell representative volume element.

Figure 5.21 shows the same reduction in effective swelling plotted for several unconstrained swelling ratios over the range of permissible volume fractions. This result is indistinguishable from that presented in Figure 5.5.

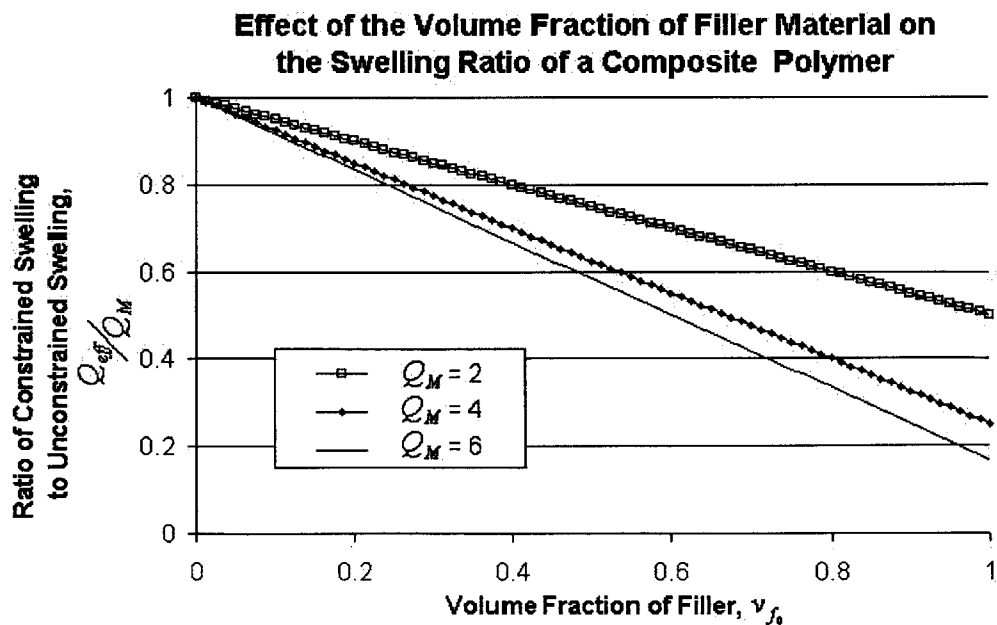


Figure 5.21: The reduction in effective composite swelling at various unconstrained swelling levels

5.6 Reference

- [5.1] J. D. W. Madden, P. G. A. Madden, and I. W. Hunter: *Polypyrrole actuators: modeling and performance*. Smart Structures and Materials 2001: Electroactive Polymer Actuators and Devices. Vol **4329**, 72, 2001.
- [5.2] J. Berroit, F. Lequeux, H. Montes, and H. Pernot, "Reinforcement of model filled elastomers: experimental and theoretical approach of swelling properties," *Polymer*, **43**, 6131-6138, 2002.
- [5.3] R. W. Ogden, Non-Linear Elastic Deformations. Mineola, New York: Dover Publications, 1984.
- [5.4] M. Danielsson, *Ph. D. Thesis*, MIT, Boston, MA, 2004.

Chapter 6: Future Work and Conclusions

6.1 Future Work: Transient Analysis and the Bilayer Strip

Many studies of conducting polymer actuators utilize “bimorphs” (bilayer strips) to demonstrate the actuation (e.g. see [6.1-6.6]). Bimorphs are bilayer structures which consist of a layer active material bonded to an inert layer. The difference in response of the two layers to the external stimulus induces large bending deflections and thus provides mechanical assist to the active response of the polymers. One of the earliest and most commonly used applications of this effect is the use of bimetallic strips as thermostats where the layers in the bilayer strip have very different thermal expansion coefficients and thus respond (expand) very differently to temperature changes. In another example, Jager, Smela, and Inganäs [6.4] created 20- μm wide “microfingers” using this principle. The “fingers” were able to grab a 30- μm fiber upon a change in electric charge state, shown schematically in Figure 6.1:



Figure 6.1: Sketch of a fiber grabbed by a microfinger (from Fig. 2 [6.4]).

In the same paper, a 670- μm long microrobot arm made of polypyrrole microactuators consisting of an “elbow,” a “wrist,” and a “hand” with two to four “fingers” was used to grab, lift, and move a 100- μm glass bead over a system of polyurethane tracks [6.4]:

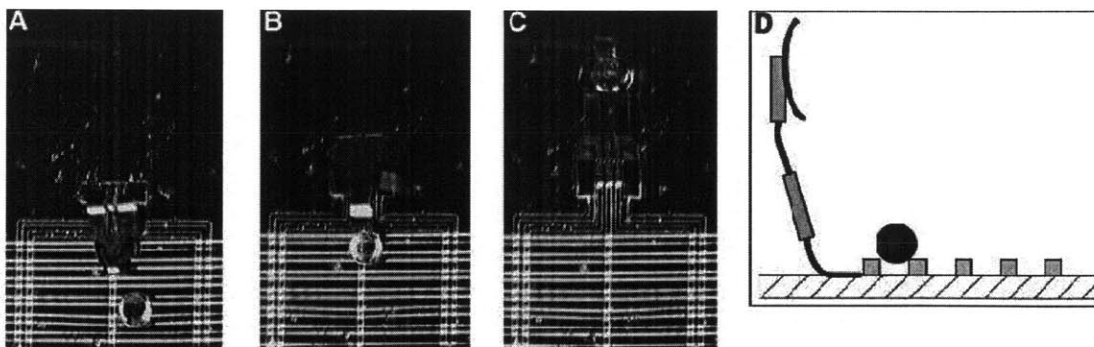


Figure 6.2: A microrobot arm moves a bead across a system of polyurethane tracks. (A) Bead is lying on track 4. (B) Bead has been moved to track 1. (C) Retracted arm holding the glass bead in its fingers. (D) Schematic picture of the setup. The distance between adjacent tracks was 60 μm , and the total displacement of the glass bead that could be achieved in this setup was $\sim 270 \mu\text{m}$ [6.4 Fig. 3].

The authors go on to demonstrate the use of these micractuator as hinges on plates, in the case of Figure 6.3 as the lid to a microcavity for biological cells [6.4]. The size of the lid is $100\ \mu\text{m}$ by $100\ \mu\text{m}$. The Polypyrrole (PPy) hinge opens and closes the cavity in response to electric stimulation.

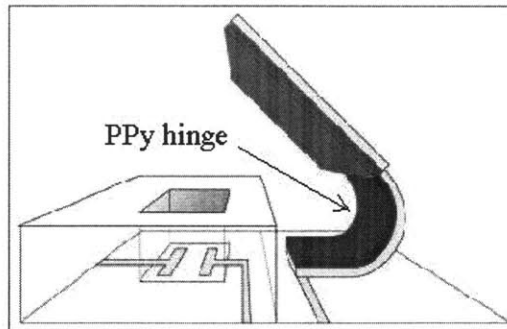


Figure 6.3: A schematic picture of a cell clinic consisting of a microcavity and lid (from Fig. 4 [6.4]).

6.1.1 Model Description

A bilayer strip is constructed by the adhesion of two dissimilar strips of material, often of the same initial thickness as in Figure 6.4:

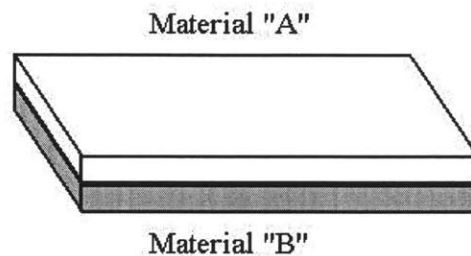


Figure 6.4: Basic schematic of a bilayer strip

Let us assume that material “A” has a large coefficient of thermal expansion, and material “B” has no sensitivity whatsoever to changes in temperature. If both strips of material are perfectly flat and adhered to each other, an increase in temperature will cause the material “A” to expand in volume, while the volume of material “B” is unchanged but still attached to the other strip. At the interface between materials, the volume change in “A” is restricted by contact with “B”, and therefore mismatched stresses develop between the two and create a bending moment. This bending moment results in the curvature of the beam depicted qualitatively in Figure 6.5:

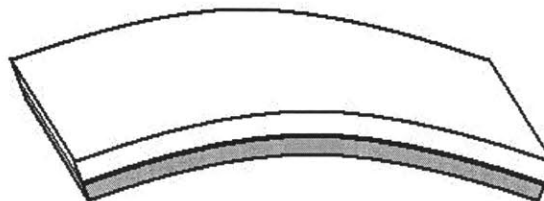


Figure 6.5: Deflection of a bilayer strip

Now if we replace material “A” with an active (swelling) polymer, such as those described in previous chapters, and material “B” with an inactive polymer or other inactive material, the situation is hypothetically the same. Instead of a temperature change prompting deflection of the strip, it could be a change in pH or electric charge, or any of the other activation mechanisms already introduced.

In his Ph.D. studies, Madden examined the performance of the encapsulated bilayer actuator presented in Figure 6.6 from Madden [6.6]. The actuator was 40-mm long, 10-mm wide, and approximately 220- μm thick. The experimental setup consists in effect of two stacked bilayer strips, where the active polypyrrole layers induce bending in the same direction, dependent upon the electrode voltage, on the top and bottom surfaces of the PMMA gel electrolyte. The bilayer strip from Figure 6.4 manifests itself in Figure 6.6 as the Polypyrrole layer (material “A”) and a symmetric half of the PMMA gel electrolyte layer (material “B”):

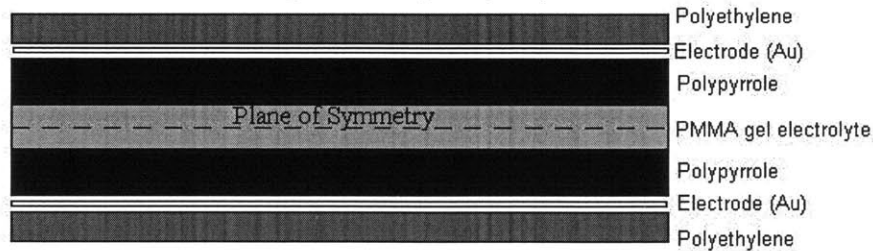


Figure 6.6: A cross section of an encapsulated bilayer actuator. Thickness of the layers are (1) Polyethylene 20 μm , (2) Au 100 nm, (3) Polypyrrole 40 μm , and (4) PMMA gel 100 μm [6.6].

Using finite element analysis, we may now model the encapsulated bilayer strip presented in Figure 6.6. Due to the plane of symmetry, only the top layer of polypyrrole and PMMA gel are modeled, such that Figure 6.6 now resembles closely Figure 6.4. In previous chapters, the swelled state of the active polymer was assumed to have reached an equilibrium state (steady state analysis). This section will present the results of the computational steady state analysis as a departure point for future work in transient behavior. Using the finite element software, ABAQUS, we start by creating the two strips of material depicted in Figure 6.4:

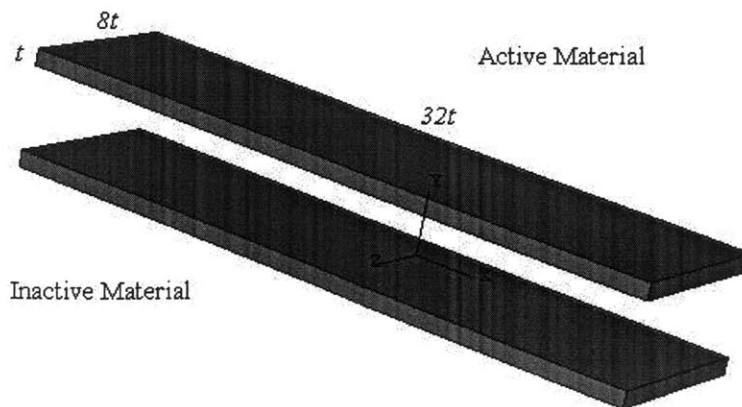


Figure 6.7: Using ABAQUS, two strips of material are instantiated. Each strip has thickness t , length $L = 32t$, and width $w = 8t$.

Next, the strips are moved into the proper alignment, though not yet adhered:

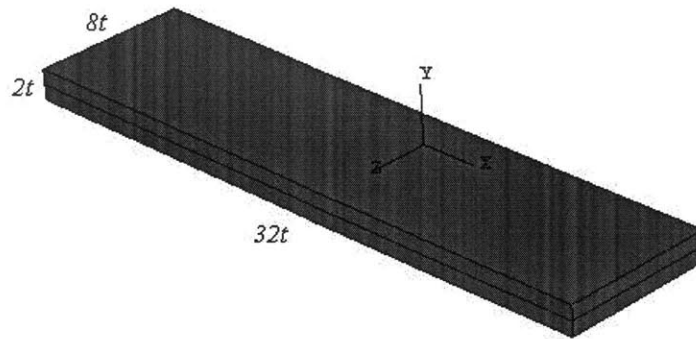


Figure 6.8: The initial bilayer strip, modeled after Figure 6.4.

At this time, it is appropriate to note and exploit additional symmetry in the formulated problem. The deformed body shown in Figure 6.5 has two planes of symmetry. They are located through the centroid of the strip and along the principal axes “X” and “Z” given in Figure 6.8. Let us now treat the computational model as only a portion cut away from the original bilayer strip along the symmetry lines:

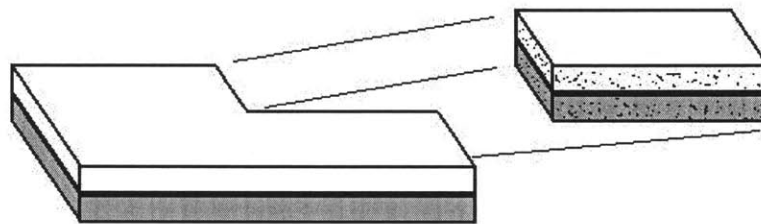


Figure 6.9: The smaller piece of material can be used to model the entire strip, because of symmetry.

The advantages of exploiting the symmetry of this problem are 1) the computational cost of modeling has been reduced by $\frac{1}{4}$ and 2) we may now more easily glimpse into the interior of the deforming material, because we have effectively cut a cross section through the symmetry planes.

Next, constraints are applied to the computational model. First, some point must be fixed in space to prevent arbitrary rigid body translation of the strip. Conveniently, the centroid of the strip is assigned the zero displacement condition:

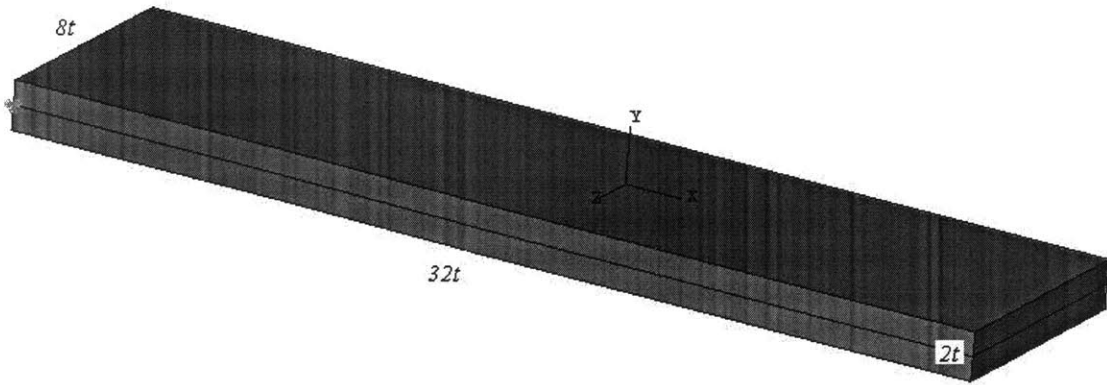


Figure 6.10: Note the position of the constrained center of the strip.

The symmetry along the front face (the $+Z$ face) of the bilayer strip constrains the plane to remain flat – i.e. no displacement is allowed in the Z direction on that plane. Likewise, the other symmetry plane (the $-X$ face) must not allow deformation in the X - direction. Finally, we adhere the two strips by enforcing zero relative displacement between the adjoining surfaces at the interface. These constraints are made graphic in Figure 6.11:

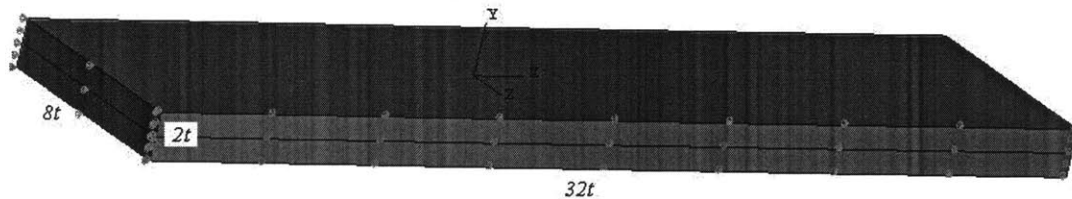


Figure 6.11: Constraints are applied along the symmetry planes.

Finally, the part is seeded and meshed with finite elements. An 8-node hybrid linear brick element was used for this analysis, as in Figure 6.12:

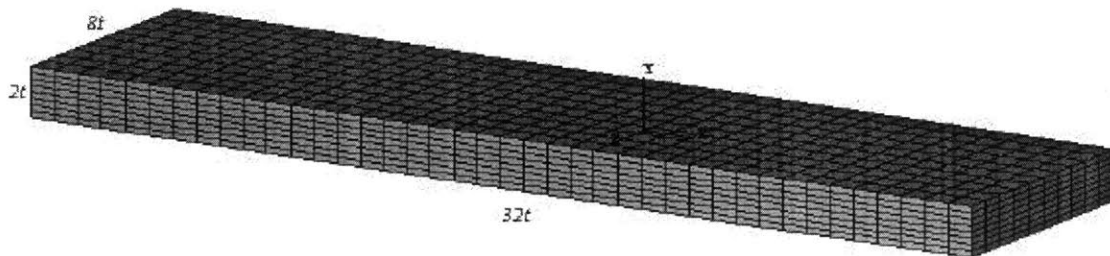


Figure 6.12: An 8-node brick mesh of the bilayer strip.

6.1.2 Model Results: Steady State

Many different loadings may be explored, all departing from the same initial conditions given above. The benchmark case of uniform steady state swelling is explored first. We must impose a condition of swelling on the active material. This is accomplished using temperature as a dummy internal variable. By setting the coefficient of thermal expansion, α , in the active material to unity, we can increase the volume of an element in the model simply by incrementing the temperature. The material properties' dependence on the swelled state is accounted for by using temperature as an internal variable in the user defined subroutine that describes the material behavior (see Appendix). In a sense, temperature becomes the λ_s from Chapter 3. For applications with real-life active materials, the change in “temperature,” $\Delta\Theta$, indicates a change in pH or oxidation state (or any of the other activation mechanisms) and the thermal expansion coefficient, “ α ,” maps how this change in stimuli creates swelling, $\lambda_s = 1 + \alpha\Delta\Theta$.

The inactive material is subjected to the same temperature fields, but has no “coefficient of thermal expansion” and the temperature dependence is written out of the subroutine. An example of a resulting deformation is displayed in Figure 6.13:

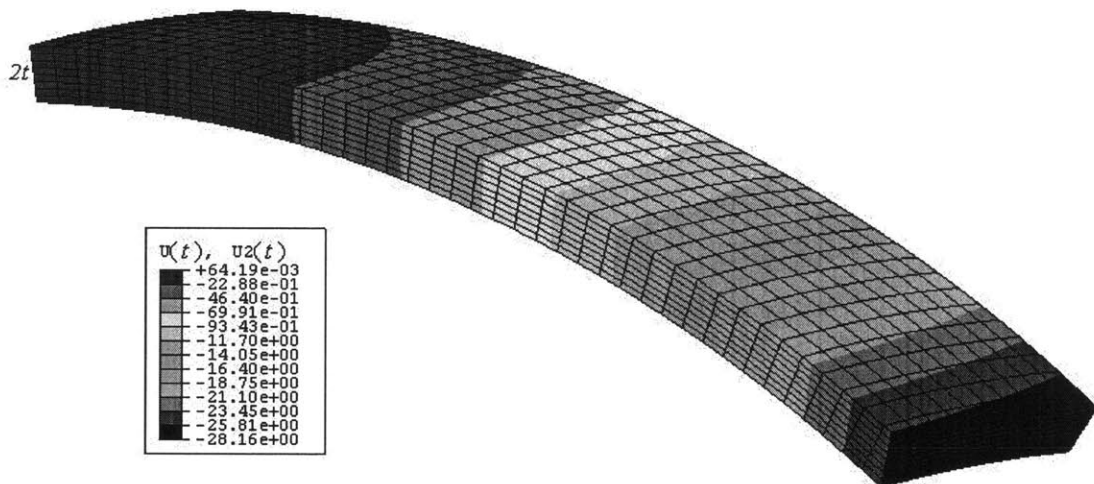


Figure 6.13: Bending of the bilayer strip due to swelling action, $\lambda_s = 1.01$. The dimensions of the contour variable, U_2 , are in terms of the thickness of one strip, t (e.g. the maximum deflection observed in the assembly is $\sim 28.16 t$).

The contours in Figure 6.13 show the displacement in the “2” or “Y” or downward facing direction. They indicate how much each node of the beam has deflected from its original position relative to the initial thickness of one of the strips, t , or half the thickness of the combined strips, $2t$. Besides noting that obviously the beam deflects the nearer the element is to the free end, observe the curvature of the contour lines across the top face. This feature reminds us that we are modeling $\frac{1}{4}$ of a beam which is no longer symmetric across its width. The outside edge deflects slightly more than the center because it has less surrounding material constraining

volume expansion. Because we happened to choose a bilayer strip with a high aspect ratio, a moderately small amount of swelling causes a large deflection (thin strips are easier to bend).

Researchers often use the thinnest possible strips to save on the cost of material, to eliminate spatial gradients through the thickness, and to reduce the time constant of the device (the time needed for the entire layer to respond to the stimulus is usually governed by a transport process such as diffusion). It may be difficult to see both the swelling of the top layer and the differences between the inner and the outer elements of the strip in Figure 6.13. Figure 6.14 shows a much thicker strip formulated in the same way and subjected to a change in temperature exactly an order of magnitude higher. The swelling of the active material is now plain, as is the added deflection on the outer edge. Also, this figure gives an indication of the stress profiles around the interface of the materials – tensile in the active material and compressive in the inactive layer – that cause the bending moment:

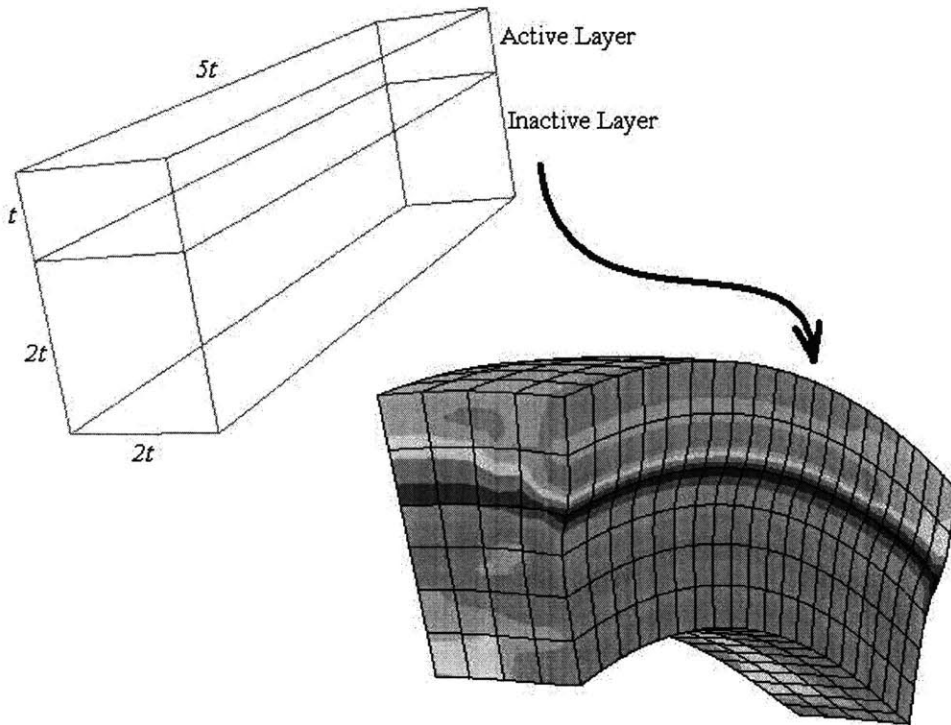


Figure 6.14: Deflection of a “thick” bilayer strip plotted with Von Mises stress contours, $\lambda_s=1.10$.

We now have the framework from which to model any of the examples given in Figures 6.1-6.3. However, the scope of problems that such a simulation could meaningfully address is somewhat limited by the steady state condition. The critical information needed to accurately and usefully model problems such as those at the start of this chapter is found in the time-dependent relationships between the activating mechanisms and external stimuli, which in turn require transient analysis.

6.1.3 Transient Analysis and Future Work

The constitutive theory developed and presented in the previous chapters has been utilized to explain and model conducting polymer actuators, with particular emphasis on the spherically embedded rigid particle within an active polymer matrix. Although it is important and often insightful for a theory to accurately explain observed phenomena (e.g. see Figure 4.13), theories become much more useful tools when they are predictive of future events and experiments not yet performed, perhaps with entirely new materials and operating environments.

In a recent paper [6.7] on the relation of conducting polymer actuator material properties to performance, the authors note the high importance of not only accurately modeling the materials to predict the behavior of the actuators, but also understanding the connection between material properties and performance. Some of the fundamental actuation mechanisms and material properties they cite include ionic diffusion rate, electrochemical operating window, strain to charge ratio, ratio of charge carried by positive versus negative ions, polymer capacitance and conductivity, ion size, and electrolyte conductivity.

Implicit throughout much of the previous chapters is the assumption that the swelling ratio of a given problem is either known, or simply a parameter to be assigned a value. In reality, factors such as those listed above, as well as many other quantities (including perhaps pH level or magnetic field strength) influence and determine the degree of swelling and other changes in the properties of an actuating polymer. A predictive constitutive model must include the effects of these relationships, likely in the form of coupled, time varying field equations (e.g. diffusion equations coupled with chemical and electric field effects).

The design of the simple bilayer applications at the beginning of this chapter clearly requires transient analysis. The steady state formulation presented throughout this work is merely a framework for the solution to a much more general problem. The ability to design with increasing sophistication relies on complete understanding of the transient behavior, which in turn comes directly from a thorough knowledge of the relationships between actuating mechanisms and stimuli. Future work should focus on developing and understanding these relationships, and then incorporating them into a more usefully predictive and robust constitutive model.

6.2 Conclusions

The purpose of this thesis was to develop a three-dimensional constitutive model of active polymeric materials, including changes in material volume and properties due to actuation. Using the principles of continuum mechanics and the application of classical and current statistical mechanics, a three-dimensional constitutive model including swelling effects was created. This model was then applied to some commonly used benchmark experiments and compared with results reported in the literature. Specifically, the constitutive model was applied in the treatment of the swelling of a particle filled elastomer previously reported in the literature using a linear elastic model. Therefore, the objective of this thesis has been completed, and the utility of the model under a variety of complex situations has been demonstrated.

Future work should endeavor to make connections between the actuation variables (pH, voltage, magnetic field) and the actuation mechanisms that cause change in the material. Greater understanding of these relationships will allow for more accurate and predictive three-dimensional constitutive models capable of transient analysis. This may in turn lead to the discovery of better performing materials, as well as the increased reliability and effectiveness of polymer actuating systems.

6.3 Reference

- [6.1] E. W. H. Jager, E. Smela, O. Inganäs, I. Lundstrom, "Polypyrrole microactuators," *Synthetic Metals*, 102 (1-3), pp. 1309-1310, June 1999.
- [6.2] R. H. Baughman, "Conducting polymer artificial muscles," *Synthetic Metals*, 78, pp. 339-353, 1996.
- [6.3] R. Lumia, M. Shahinpoor, "Microgripper design using electro-active polymers," *Proceedings of the 1999 SPIE Smart Structures and Materials Symposium, Electroactive Polymer Actuators and Devices*, Y. Bar-Cohen (ed.), vol. 3669, pp. 322-329, 1999.
- [6.4] E. W. H. Jager, E. Smela, O. Inganäs, "Microfabricating Conjugated Polymer Actuators," *Science*, 290, pp. 1540-1545, Nov 2000.
- [6.5] Y. Bar-Cohen, S. Leary, M. Shahinpoor, J. O. Harrison, J. Smith, "Electro-Active Polymer (EAP) actuators for planetary applications," *Proceedings of the 1999 SPIE Smart Structures and Materials Symposium, Electroactive Polymer Actuators and Devices*, Y. Bar-Cohen (ed.), vol. 3669, pp. 57-63, 1999.
- [6.6] J. D. W. Madden, *Ph. D. Thesis*, MIT, Boston, MA, 2000.
- [6.7] P. G. A. Madden, J. D. W. Madden, P. A. Anquetil, N. A. Vandesteeg, I. W. Hunter, "The relation of conducting polymer actuator material properties to performance," *IEEE Journal of Oceanic Engineering*, 29 (3), pp. 696-705, July 2004.

Appendix

This appendix includes the uhyper subroutine used primarily throughout the work for finite element implementation within ABAQUS. This subroutine is the 8-chain model with swelling effects, though the Gaussian model may be used by setting “n” to a large value. The author’s notes are prefaced by an “!” and are not part of the computer code.

```
SUBROUTINE UHYPER(BI1,BI2,AJ,U,UI1,UI2,UI3,TEMP,NOEL,CMNAME,  
$      INCOMPFLAG,NUMSTATEV,STATEV,NUMFIELDV,  
$      FIELDV,FIELDVINC,NUMPROPS,PROPS)
```

! The “\$” indicates the continuation of a line of code to the next line

```
INCLUDE 'ABA_PARAM.INC'
```

```
REAL(8) Beta,Betas,I,m,v,x,c,xs,lambchain  
CHARACTER*80 CMNAME  
REAL(8) U,UI1(3),UI2(6),TEMP  
DIMENSION UI3(6),STATEV(*),FIELDV(*),  
$      FIELDVINC(*),PROPS(*)  
PARAMETER (ZERO=0.0D0,ONE=1.0D0,TWO=2.0D0,THREE=3.0D0)
```

```
CT=1.
```

! CT is the “coefficient of thermal expansion” explained in section 5.4.

```
xls = 1.+CT*TEMP
```

! xls = λ_s , the swelling stretch (in any direction)

```
NkT=1.      !MPa
```

```
n=5000.
```

! The number of rigid crosslinks, large numbers approach Gaussian model behavior.

```
lambchain=(xls*(1./3.*(BI1))**(1./2.))
```

! $\text{lambchain} = \Lambda_{chain} = \lambda_s \left[\frac{1}{3} (\lambda_1^2 + \lambda_2^2 + \lambda_3^2) \right]^{\frac{1}{2}} = \frac{\sqrt{I_1}}{\sqrt{3}}$

```
xs=(xls/n**(1./2.))
```

```
x=(xls*lambchain/(n))**(1./2.))
```

! x is a measure of the chain stretch, where x = 0 indicates no stretch, and x = 1 is the limiting extensibility

```
Beta=(1.31446*tan(1.58986*x)+.91209*x)
```

```
Betas=(1.31446*tan(1.58986*xs)+.91209*xs)
```

! Dummy Expressions to shorten UI1,2, etc.:

```
I=dble(BI1**(1./2.))
```

```
m=dble(n**(1./2.))
```

```
v=dble(0.603275/cos(x)**2/I/m)
```

```
c=dble(0.263298/I/m+v)
```

! Curve fitting: In order to simplify calculations, a curve was fit to the function

$$! U_{sch} = N_c k_B \Theta \sqrt{n} \left[\beta_{chain} \lambda_{chain} + \sqrt{n} \ln \left(\frac{\beta_{chain}}{\sinh \beta_{chain}} \right) \right].$$

! When $x < .84$, the following strain energy function is used:

```
IF(0<x<=0.84136)THEN
U=dbl(NkT/xls**3*(n)**(1./2.)*(Beta*lambchain+m*log(Beta
$/sinh(Beta))-Betas*xls-m*log(Betas/sinh(Betas))))
```

! The first derivative of U with respect to the first stretch invariant I_1 , $\frac{\partial U(I_1)}{\partial I_1}$:

```
UI1(1)=dbl(m/xls**3*NkT*(0.57735*I*(0.263298/I/m+v)+
$0.288675*(Beta)/I+(m*sinh(Beta)*(1/sinh(Beta)*(0.263298/I/m+v)+
$1/tanh(Beta)*1/sinh(Beta)*(-.263298/I/m-v)*(Beta)))/(Beta))
```

! The second derivative of U with respect to the first stretch invariant I_1 , $\frac{\partial^2 U(I_1)}{\partial I_1^2}$

```
UI2(1)=dbl(m*NkT/xls**3*(0.57735/I*(c)-0.144338*(Beta)/I**3+
$0.57735*I*(-.131649/I**3/m-0.301638*1/cos(x)**2/I**3/m+0.55375/
$cos(x)**2*tan(x)/BI1/n)-(m*(c)*sinh(Beta)*(1/sinh(Beta)
$*(c)+1/tanh(Beta)*1/sinh(Beta)*(-c)*(Beta)))/
$(Beta)**2+(m*cosh(Beta)*(c)*(1/sinh(Beta)*(c)+1/tanh(Beta)*1/sinh(
$Beta)*(-c)*(Beta)))/(Beta)+
$(m*sinh(Beta)*(2/tanh(Beta)*1/sinh(Beta)*(-c)*(c)+1/tanh(Beta)**2
$/sinh(Beta)*(-c)**2*(Beta)+1/sinh(Beta)**3*(-c)**2*(Beta)+
$1/tanh(Beta)*(1/sinh(Beta))*(Beta)*(0.131649/I**3/m+0.301638*
$1/cos(x)**2/I**3/m-0.55375*1/cos(x)**2*tan(x)/BI1/n)+1/sinh(Beta)*
$(-.131649/I**3/m-0.301638/cos(x)**2/I**3/m+0.55375/cos(x)**2*
$tan(x)/BI1/n)))/(Beta))
```

! The same process is repeated for the area near the limiting extensibility, using a more appropriate curve fitting:

```
ELSE IF(1>=x>0.84136)THEN
Beta=DBLE(1/(1-dble(lambchain/m)))
Betas=DBLE(1/(1-dble(xls/m)))

t=dble(1-x/m)
U=DBLE(NkT/xls**3*m*dble((Beta*lambchain+m*Log(Beta/sinh(Beta)))
-$Betas*xls-dble(m*Log(Betas/sinh(Betas))))))
```

```
UI1(1)=DBLE(1/xls**3*(m*NkT*(0.288675/I/t+0.166667/t**2/m+t*m*(
$0.288675/sinh(1/t)/I/t**2/m-0.288675/tanh(1/t)/sinh(1/t)/I/t**3/m)
$*sinh(1/t))))
```

```
UI2(1)=0
```

!If $x < 0$ or $x > 1$, then it has no meaning, and so return an error message:

```
ELSE IF(x>1.or.x<=0)THEN
U=0
UI1(1)=0
UI2(1)=0
print *, "Error - Exceeded maximum chain length"
END IF
UI1(2)=ZERO
UI1(3)=ZERO
UI2(2)=ZERO
UI2(3)=ZERO
UI2(4)=ZERO
UI2(5)=ZERO
UI2(6)=ZERO
UI3(1)=ZERO
UI3(2)=ZERO
UI3(3)=ZERO
UI3(4)=ZERO
UI3(5)=ZERO
UI3(6)=ZERO
RETURN
END
```